Nathan Torggler, BSc

Numerical Studies of Embedded Beam Row in Safety Analysis in PLAXIS 2D

MASTER'S THESIS

to achieve the university degree of

Diplom-Ingenieur

Master's degree programme: Civil Engineering, Geotechnics and Hydraulics

submitted to

Graz University of Technology

Supervisor

Ao.Univ.-Prof. Dipl.-Ing. Dr.techn. M.Sc. tit.Univ.-Prof.
Helmut Schweiger

Institute of Soil Mechanics and Foundation Engineering

Graz, September 2016

AFFIDAVIT

I declare that I have authored this thesis independently, that I have not used other than the declared sources/resources, and that I have explicitly indicated all material which has been quoted either literally or by content from the sources used. The text document uploaded to TUGRAZonline is identical to the present master‘s thesis.

Date

Signature

Danksagung

Ein ganz besonderer Dank gilt in erster Linie meinem Betreuer Helmut Schweiger, der meine Arbeit geduldig und zeitintensiv betreut hat. In weiterer Folge danke ich auch Franz Tschuchnigg, der immer Zeit fand an den Besprechungen teilzunehmen und durch seine Beiträge wesentlich zur Arbeit beigetragen hat.

Außerdem danke ich Mathilde für ihre persönliche Unterstützung und besonders für das sorgfältige Korrekturlesen.

Diese Arbeit widme ich meinem Vater, meiner Mutter und meinen beiden Schwestern, die mir das Studium ermöglicht haben.

Einen wichtigen Teil zum Abschluss meines Studiums haben meine Kommilitonen Matthias, Dominik und David beigetragen, die vor allem während des Bachelorstudiums eine motivierende Kraft für mich waren. Meine Mitarbeit in der Studienvertretung FvBau hat für Abwechslung im Uni-Alltag gesorgt.

All meinen Freunden und Kollegen danke ich für die gemeinsamen Abenteuer und die unvergessliche Zeit in Graz, Trondheim, Stockholm und zu Hause.

Kurzfassung

Es gibt zahlreiche Methoden zur Bestimmung der Standsicherheit. Bei der Finite-Element-Methode kommt häufig die „phi/c-Reduktion“ zum Einsatz. Dabei werden die Scherparameter bis zum Erreichen des Grenzzustandes abgemindert. Zweidimensionale Analysen sind wesentlich schneller als dreidimensionale Berechnungen. PLAXIS bietet die Möglichkeit, Pfahlreihen mit der sog. „Embedded Beam Row“ in 2D zu modellieren. Ziel dieser Arbeit ist es, die Anwendung der „Embedded Beam Row“ für Standsicherheitsanalysen zu untersuchen. Dabei wird hauptsächlich die Anwendung dieses Strukturelements für die Bodenverdübelung ausgewertet. Der Einfluss der einzelnen Parameter wird für eine homogene Böschung und eine Böschung mit einer Scherfläche ausführlich untersucht. Die praktische Anwendung wird anhand einer kurzen Fallstudie aufgezeigt.

Abstract

The Strength Reduction method with Displacement Finite Element Analysis is a common tool to obtain the safety factor of natural or artificial slopes. Two-dimensional analyses are less time-consuming as analyses in three dimensions. PLAXIS introduced the Embedded Beam Row to model pile rows in 2D. Aim of this thesis is a numerical study of the application of the Embedded Beam Row in Slope stability analyses. The main objective is the utilisation of the Embedded Beam Row for modelling pile-like elements acting as dowels. The influence of individual parameters is studied extensively in a homogeneous slope and in a slope with a weakness zone. A short case study is elaborated.

Table of contents

List of figures

List of tables

List of symbols and abbreviations

Capital letters

A	$[m^2]$	Profile area
c'	$\left[\frac{kN}{m^2}\right]$	Effective cohesion
$c'_{mobilised}$	$\left[\frac{kN}{m^2}\right]$	Mobilised effective cohesion
D_{eq}	$[m]$	Equivalent diameter
E	$\left[\frac{kN}{m^2}\right]$	Young's Modulus
F_{bot}	$\left[\frac{kN}{m}\right]$	Force at bottom
F_{max}	$[kN]$	Base resistance
FoS or ΣM_{sf} or F	$[\ ]$	Safety factor
G	$\left[\frac{kN}{m^2}\right]$	Shear Modulus ($G = \frac{E}{2(1+\upsilon)}$)
G_{soil}	$\left[\frac{kN}{m^2}\right]$	Shear modulus surrounding soil
I	$\left[\frac{kN}{m^2}\right]$	Moment of inertia
ISF_{RS}	$[\ ]$	Interface stiffness factor for skin stiffness R_S
ISF_{RN}	$[\ ]$	Interface stiffness factor for skin stiffness R_N
ISF_{KF}	$[\ ]$	Interface stiffness factor for base stiffness K_F
K_0	$[\ ]$	Earth pressure coefficient at rest
K_f	$\left[\frac{kN}{m}/m\right]$	Pile base stiffness
$L_{spacing}$ or L_s or a	$[m]$	Spacing
M	$[kNm]$	Bending moment
N	$[kN]$	Normal force
N_q and N_c	$[\ ]$	Bearing capacity factors
Ø	$[m]$	Diameter
Q	$[kN]$	Shear force
R_{eq}	$[m]$	Equivalent radius
R_n	$\left[\frac{kN}{m^2}/m\right]$	Lateral skin stiffness
R_s	$\left[\frac{kN}{m^2}/m\right]$	Axial skin stiffness
S	$[kN]$	Shear force in the shear zone
T_{lat}	$\left[\frac{kN}{m}\right]$	Lateral skin resistance
T_{skin}	$\left[\frac{kN}{m}\right]$	Axial skin resistance

Small letters

c_u	$\left[\frac{kN}{m^2}\right]$	Undrained cohesion
d	$[m]$	Pile diameter
d_q and d_c	$[\,]$	Depth factor (non-cohesive and cohesive soils)
f_{yd}	$\left[\frac{N}{mm^2}\right]$	Steal strength
l	$[m]$	Length of the shear zone
p	$\left[\frac{kN}{m}\right]$	Load on the dowel
q	$\left[\frac{kN}{m^2}\right]$	Vertical earth pressure
t_s	$\left[\frac{kN}{m^2}\right]$	Shear stress
t_n	$\left[\frac{kN}{m^2}\right]$	Normal stress
$u_{foot}^{p} - u_{foot}^{s}$	$[m]$	Displacement between pile and soil at foot
$u_{n}^{p} - u_{n}^{s}$	$[m]$	Displacement between pile and soil in lateral direction
$u_{s}^{p} - u_{s}^{s}$	$[m]$	Displacement between pile and soil in axial direction
w_{pl}	$[m^3]$	Plastic moment of resistance

Greek letters

γ	$[\,]$	Shear strain
γ^*	$[\,]$	Modified shear strain
γ_{sat}	$\left[\frac{kN}{m^3}\right]$	Saturated specific weight
γ_{unsat}	$\left[\frac{kN}{m^3}\right]$	Unsaturated specific weight
ε_N	$\left[\frac{kN}{m^3}\right]$	Normal strain
κ	$[\,]$	Shear correction factor ($^5/_6$)
υ	$[\,]$	Poisson's ratio
σ_N	$[\,]$	Normal stress
τ	$\left[\frac{kN}{m^2}\right]$	Shear stress
φ'	$\left[\frac{kN}{m^2}\right]$	Effective friction angle
$\varphi'_{mobilised}$	$[\,^\circ]$	Mobilised friction angle
ψ	$[\,^\circ]$	Dilatancy angle

Abbreviations

2D	Two dimensional
3D	Three dimensional
API	American Petroleum Institute
aso	and so on
Axi.	Axial skin resistance
EB	Embedded Beam
EBR	Embedded Beam Row
Elem.	Element
FEM	Finite Element Method
GLE	General Limit Equilibrium / Morgenstern Price
IF	Interface
Lat.	Lateral skin resistance
LE	Limit Equilibrium
No.	Number
PL	Plate
Pla.	Plastic
SRFEA	Strength Reduction method with displacement Finite Element Analysis
VE	Volume element
vs.	versus
w/	with

1 Introduction

1.1 Research background

When performing numerical analyses, the calculation of two dimensional (2D) models is significantly faster than in three dimensions (3D). Therefore designers often prefer using two dimensional models, especially for preliminary studies. In the past, modelling of repetitive, non-coherent structures (like pile rows, nail walls etc.) was only possible by simplifying the model. The structure in PLAXIS 2D was modelled by using plate elements, node-to-node anchors or their combinations (Sluis, 2012). The results obtained are only valuable under certain assumptions and limitations. PLAXIS 2D recently introduced a so called Embedded Beam Row (renamed, former 'Embedded Pile Row') which is similar to the Embedded Pile (renamed, former 'Embedded Pile') from PLAXIS 3D. The Embedded Beam Row is always written-out, to avoid confusion to the three-dimensional Embedded Beam.

Sluis (2012) already has investigated in detail the behaviour of the Embedded Pile Row under different load directions. Algulin & Pedersen (2014) show the application of the Embedded Beam Row to a piled raft foundation based on a case history. Kwaak (2015) studied the application of Embedded Beam Row in dynamic modelling for earthquakes. The previous papers do not cover the safety analysis of an Embedded Beam Row in PLAXIS 2D. Mosser (2016) compares generally slope stability calculations of soil nails and includes also the Embedded Beam Rows to some extent. However there is little literature available for safety analyses with the Embedded Beam Row. An extended numerical study of the Embedded Beam Row in safety analysis in PLAXIS 2D is therefore necessary.

1.2 Research objectives

The aim of this master thesis is the evaluation of the behaviour of Embedded Beam Rows in safety analysis. An extended numerical study should analyse the application limits and possibilities. The main objectives are:

- Evaluation of safety analyses of unsupported slopes
- Evaluation of safety analyses of slopes supported by an Embedded Beam Row
- Evaluation of the influence of the individual parameters in the safety analysis
- Comparison and validation using a plate with interfaces in 2D

- Comparison and validation using an Embedded Beam in 3D
- Comparison and validation using volume elements in 3D

1.3 Research limitations

For the parameters studies no water loads or additional loads are applied. Installation effects of the piles are neglected. The parameter study is mostly based on a homogeneous soil body for simplicity. The dilatancy angle is in most cases non-associated ($\psi = 0$). The soil model is Mohr-Coloumb since it is assumed that the influence of an advance soil model is negligible for the purpose if this study. Results from 2D are compared to 3D analysis but no elastoplastic material behaviour for the Embedded Beam is considered in 3D. In addition to the results from the homogeneous soil body a slope with a weakness zone is investigated.

1.4 Research approach and thesis outline

At the beginning of the thesis a short overview of the theoretical background is given based on a literature survey. Stability analysis, soil doweling, Embedded Beam Rows and safety analysis in PLAXIS are explained. After that the slope stabilisation with an Embedded Beam Row of a homogeneous slope is described. First the unsupported slope and the mesh are studied. This is followed by calculations with a plate element as support. The impact of various input parameters for the Embedded Beam Row is evaluated. The results obtained from 2D analyses are than compared to 3D analyses. The study of the slope with a weakness zone follows a similar pattern. A short case study based on the results obtained from Grabe (2016) is performed. Finally a conclusion is given. The structure of the thesis is presented in Figure 1.

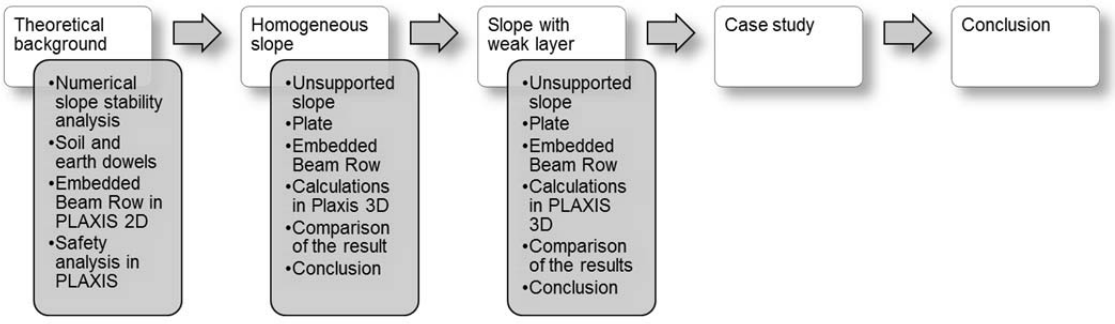

Figure 1 Structure of the thesis

2 Theoretical background

2.1 Numerical slope stability analysis

In general stability analyses are performed to determine failure mechanisms and the safety factor of geotechnical structures. Slope stability analyses are applied to natural and artificial slopes.

Different methods are available to perform the safety analysis. The safety analysis in PLAXIS is based on the displacement finite element method. The method is described in chapter §2.1.2. Comparative calculations are performed based on 'Limit Equilibrium' (see chapter §2.1.1). Further methods to evaluate slope stability are not treated here.

2.1.1 Limit equilibrium

The limit equilibrium method is the oldest method to evaluate slope stability and was first used by Coulomb. In most cases the failure is governed by the strength parameters effective cohesion c' and effective friction angle φ'. Several techniques based on the method of slices are available: Janbu, Bishop, Morgenstern & Price, Spencer aso. They all differ in their assumptions about equilibrium of moments and forces or in the form of the failure surface (circular or non-circular). The differences of the methods will not be further discussed here. The challenge of these methods is the derivation of the decisive failure mechanisms. (Wolffersdorff et al., 2008). A wide range of geotechnical software is available to perform the analysis; some comparative calculations based on the limit equilibrium method are performed with 'SLIDE Ver. 7.013 64-bit' by Rocscience.

2.1.2 Displacement finite element method

The predictions of the failure mechanisms and the stability of a slope with the displacement finite element method are usually performed by means of strength reduction method, where the strength of the soil is decreased till a failure occurs (Sloan, 2013). PLAXIS uses this approach for its safety analysis and describes it under the term 'Phi/c reduction'.

The strength, under assumption of a Mohr-Coloumb criterion, is described by the friction angle φ' and the cohesion c' . The strength factors are decreased till a failure is reached. The computation is described in Brinkgreve & Bakker (1991). The safety factor from this method is obtained by:

$$FoS = \frac{\tan \varphi'}{\tan \varphi'_{mobilised}} = \frac{c'}{c'_{mobilised}} \quad (1)$$

FoS	[ ]	Safety factor
c'	$\left[\frac{kN}{m^2}\right]$	Effective cohesion
$c'_{mobilised}$	$\left[\frac{kN}{m^2}\right]$	Mobilised effective cohesion
φ'	[°]	Effective friction angle
$\varphi'_{mobilised}$	[°]	Mobilised effective friction angle

Sloan (2013) mentions the advantages and the reasons why the displacement finite element method is widely spread for the determination of slope stabilities:

- associated and non-associated flow rule can be applied
- method works also with heterogeneity and anisotropy
- hardening and softening effects can be taken into account
- combined with fully coupled consolidation and dynamics

Other than the limit equilibrium approach, the failure mechanism in displacement finite-element analysis is determined automatically in the zones where the shear stresses exceed the failure criterion. There is no need for assuming inter-slice forces. The deformation can be evaluated on working stress level, where the limit equilibrium gives no information about deformation at all, see e.g. Griffiths & Lane (1999). However it is not straight forward to predict displacements of the onset of failure.

The flow rule, associated or non-associated, generally affects the safety analysis. In this work in most cases a dilatancy angle $\psi = 0$ is assumed (non-associated flow rule) which can be considered to be conservative.

Tschuchnigg et al. (2015) mentions that the results obtained from SRFEA are dependent on the mesh discretization, the element type and the convergence criteria. In the numerical studies the mesh size is analysed for every slope type. For all two-dimensional analysis in PLAXIS 2D high-order 15-noded elements are used, as recommended by Brinkgreve et al. (2016a).

'PLAXIS 2D Version 2015.02 (Build 4979)' and 'PLAXIS 3D AE.01 (Build 11778)' are used for the calculations.

2.2 Soil and earth dowels

The following definitions and approaches are based on literature about earth and soil doweling. Soil doweling is mostly performed by bored piles of any size, diaphragm wall elements or large elliptical concrete structures. Injection doweling with remaining steel pipes can also be considered as soil doweling, but shows like micro piles a different behaviour. Driven piles (made of steel, timber or reinforced concrete) are often used especially in disaster operations. In general earth dowels are designed as non-continuous repetitive single elements (in a certain grid), but also continuous walls are possible. Due to their slenderness and stiffness they show different behaviour. Small piles ($Ø < 0.2\ \mathrm{m}$) strongly bend and plastic deformation needs to be taken into account (Figure 2.1). Normal sized piles bend (Figure 2.2). Large piles ($Ø > 1.5\ \mathrm{m}$) only rotate because of their high stiffness (Figure 2.3). Large piles are generally stiff and mostly sheared; slender piles can also bend. Normal sized piles are often connected rigidly on top to obtain a uniform loading. When no pile group effect is taken into account the load capacity of the single piles is summed up. In many cases creep effects have to be considered. It should be noted that earth dowels are passive retaining structures, meaning that deformation is needed to activate the support (Brandl, 2009).

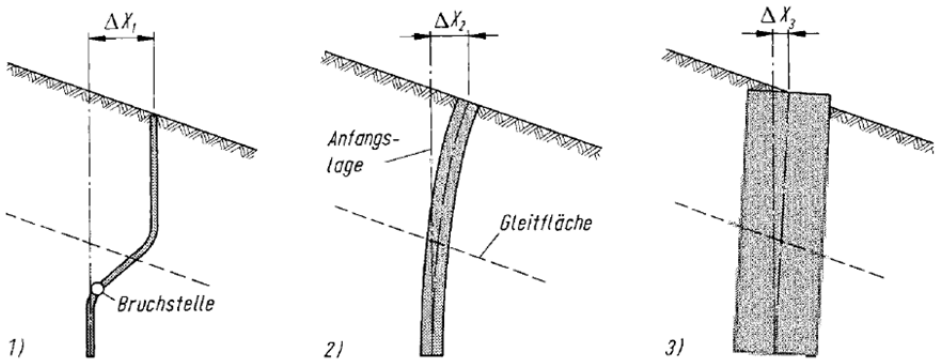

Brandl (2009)

Figure 2 Behaviour of soil dowels of different sizes (Brandl 2009)

There are several methods described in Brandl (2009) to derive the internal forces and deformations of an earth dowel. The slope stability, using limit equilibrium analysis, considers the shear resistance of the dowel for determination of the safety factor. A simple approach is explained in the dowel theory of Huder (1983). An elastic bedded pile with shear joints at the depth of the failure zone is assumed (Figure 3).

The maximal shear force in the pile is limited by the shear resistance and can be determined by the load, equation (2). The bending moment in point 'A' can be determined by equation (3), and leads to a relation between the bending moment and the shear resistance. The bending moment is derived from the maximal acceptable bending moment, the plastic bending moment, and the safety factor (4). The load p equals the passive earth pressure at the depth of the failure for walls. In cases where the piles do not form a wall, the load is determined by equation (5) for non-cohesive soils. Equation (6) is valid for cohesive soils under undrained conditions. Values for the parameters for the equations (5) and (6) can be obtained from Rüegger (2013).

$$S = Q_{max} = p \cdot \frac{l}{2} \tag{2}$$

$$M_{max} = \frac{p \cdot l^2}{8} = \left(p \cdot \frac{l}{2}\right)^2 \cdot \frac{1}{2 \cdot \mathrm{p}} = \frac{\mathrm{S}^2}{2 \cdot \mathrm{p}} \quad \Longrightarrow \quad \mathrm{S} = \sqrt{2 \cdot \mathrm{p} \cdot \mathrm{M}} \tag{3}$$

$$M_{max} \leq F \cdot M_{pl} \tag{4}$$

$$p = d_q \cdot d \cdot K_0 \cdot q \cdot N_q \tag{5}$$

$$p = d_c \cdot d \cdot (c_u \cdot N_c + K_0 \cdot q) \tag{6}$$

S	$[kN]$	Shear force in the shear zone
Q_{max}	$[kN]$	Maximal shear force in the dowel
p	$\left[\frac{kN}{m}\right]$	Load on the dowel
l	$[m]$	Length of the shear zone
M_{max}	$[kNm]$	Maximal bending moment
M_{pl}	$[kNm]$	Plastic bending moment
F	[ ]	Safety factor
d_q and d_c	[ ]	Depth factor (non-cohesive and cohesive soils)
d	$[m]$	Pile diameter
K_0	[ ]	Earth pressure coefficient at rest
q	$\left[\frac{kN}{m^2}\right]$	Vertical earth pressure
N_q and N_c	[ ]	Bearing capacity factor (non-cohesive and cohesive soils)
c_u	$\left[\frac{kN}{m^2}\right]$	Undrained cohesion

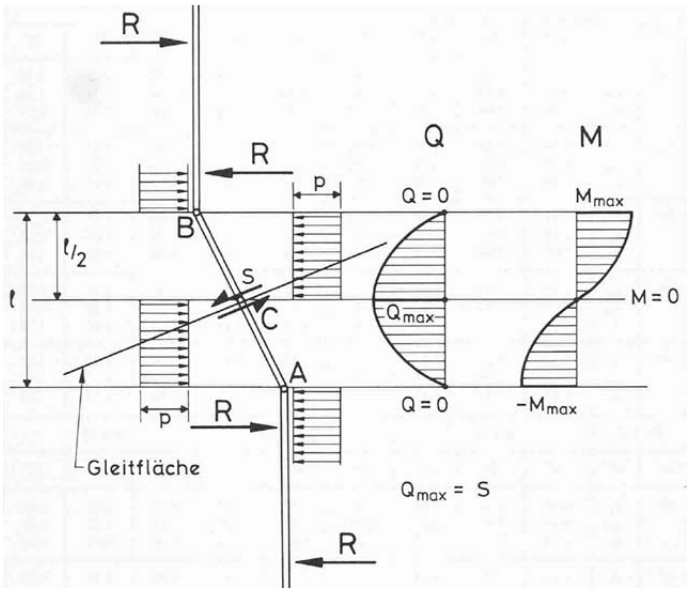

Huder (1983)

Figure 3 Dowel theory (Huder 1983)

Witt (2013) mentions standard values for earth dowels based on practical experience. In most cases multi-row dowels have a centre-to-centre spacing of 5 to $7\,\mathrm{m}$. The minimal distance equals three times the diameter. The reinforcement of the piles is usually between $200-250\,\frac{\mathrm{kg}}{\mathrm{m}^3}$.

2.3 Embedded Beam Row in PLAXIS 2D

The realistic deformation pattern and stress state of a pile is impossible to simulate with a 2D model. In the past the Embedded Beam Row was introduced based on a '2.5D model'. This simplified approach should allow dealing with repetitive, non-coherent structures in a 2D plane strain model. The Embedded Beam Row is represented by a 'Mindlin' beam element, as the plate element. This beam element is connected with interfaces to the soil mesh. Thus the beam can deform individually to the soil mesh. Also the soil can deform individually, unlike when a plate element is installed. The interface transfers forces to the Embedded Beam Row and models the soil-structure interaction. The nodes around the Embedded Beam Row are duplicated and connected via this interfaces to the soil nodes. The nodes have three degrees of freedom: two of translation (u_x, u_y) and one of rotation (ϕ_z). In PLAXIS 2D bending moments can only be calculated in elements representing plates or Embedded Beam Rows. The material data set of an Embedded Beam Row does not contain the stiffness response of piles and soil (like so called 'p-y curves'). The stiffness response is defined by the equations (7) to (13). The manual indicates that the Embedded Beam Row in general is not meant to be used for lateral loading (Brinkgreve et al., 2016a).

Figure 4 represents the above described model of an Embedded Beam Row and the interaction with the soil after Sluis (2012).

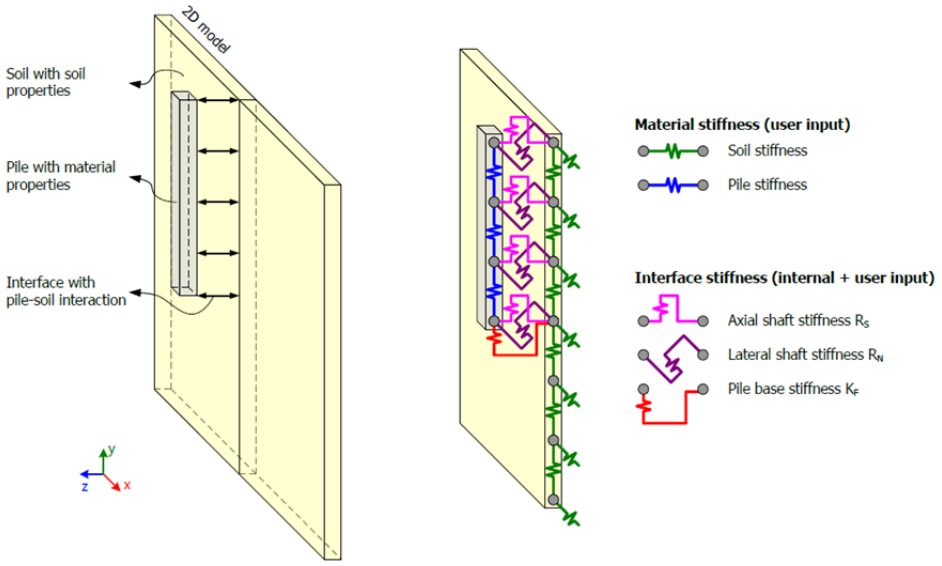

(Sluis, 2012)

Figure 4 Schematisation of the Embedded Beam Row (after Sluis, 2012)

Sluis (2012) defines in Figure 5 the possible application of Embedded Beam Rows in PLAXIS 2D in comparison with PLAXIS 3D with respect to pile spacing–diameter ratio.

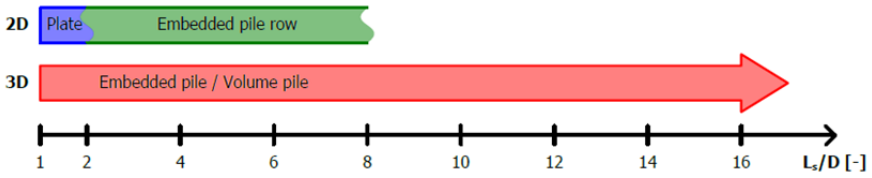

(Sluis, 2012)

Figure 5 Area of application of structural elements in 2D and 3D (after Sluis, 2012)

The interfaces describing the interaction between soil and structure are line-to-line interfaces along the pile and point-to-point interfaces at the base. The interfaces are represented by springs which are limited by a maximum force. This relationship is shown in Figure 6, adapted from Sluis (2012). The stiffness of the interfaces are currently dependent on the spacing (L_s), the shear stiffness of the surrounding soil (G_{soil}) and the interface stiffness factor. The equations defining the stiffnesses are shown below in the equations (7), (8) and (9), (Sluis, 2012).

The equivalent radius/diameter for non-circular piles is determined by the ratio of the moment of inertia and the area, equation (10). This equation is based on determination of the moment of inertia for a square profile.

$$R_s = ISF_{RS} \cdot \frac{\mathrm{G_{soil}}}{L_s} \quad (7)$$

$$R_n = ISF_{RN} \cdot \frac{\mathrm{G_{soil}}}{L_s} \quad (8)$$

$$K_f = ISF_{KF} \cdot \frac{\mathrm{G_{soil}} \cdot R_{eq}}{L_s} \quad (9)$$

$$D_{eq} = \sqrt{12 \cdot \left(\frac{EI}{EA}\right)} = \sqrt{12 \cdot \left(\frac{I}{A}\right)} = 2 \cdot R_{eq} \quad (10)$$

R_s	$\left[\frac{kN}{m^2}/m\right]$	Axial skin stiffness
R_n	$\left[\frac{kN}{m^2}/m\right]$	Lateral skin stiffness
K_f	$\left[\frac{kN}{m}/m\right]$	Pile base stiffness
ISF_{RS}	[ ]	Interface stiffness factor for skin stiffness R_S
ISF_{RN}	[ ]	Interface stiffness factor for skin stiffness R_N
ISF_{KF}	[ ]	Interface stiffness factor for base stiffness K_F
$\mathrm{G_{soil}}$	$\left[\frac{kN}{m^2}\right]$	Shear modulus surrounding soil
L_s	$[m]$	Centre-to-centre distance of piles in pile row
R_{eq}	$[m]$	Equivalent radius
D_{eq}	$[m]$	Equivalent diameter
E	$\left[\frac{kN}{m^2}\right]$	Young's Modulus
I	$\left[\frac{kN}{m^2}\right]$	Moment of inertia
A	$[m^2]$	Profile area

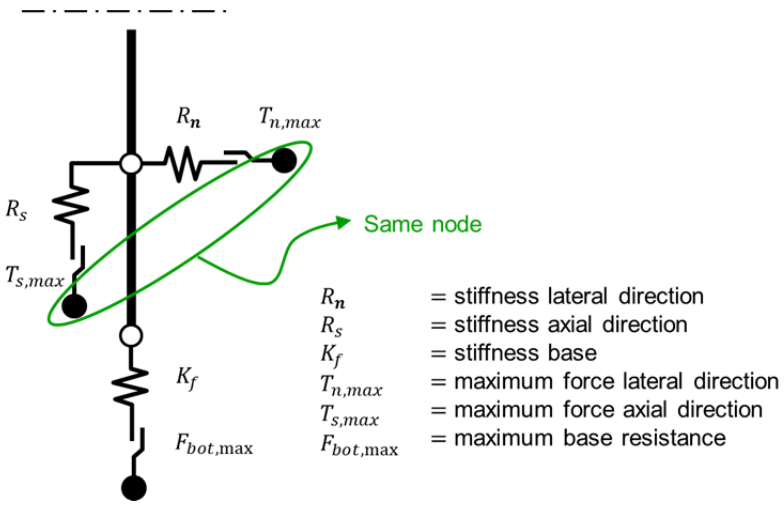

Figure 6 Soil-structure interaction with elastic springs after Sluis (2012)

The interface stiffness factors can be defined individually in PLAXIS 2D. By default the determination is based on the results from the master thesis by Sluis (2012). These interface stiffness factors are based on the determination with very stiff piles. The ratio of the stiffness parameters $\mathrm{ISF_{RS}}:\mathrm{ISF_{RN}}:\mathrm{ISF_{KN}}$ is $1:1:10$.

$$ISF_{RS} = 2.5 \cdot \left(\frac{L_s}{D_{eq}}\right)^{-0.75} \quad (11)$$

$$ISF_{RN} = 2.5 \cdot \left(\frac{L_s}{D_{eq}}\right)^{-0.75} \quad (12)$$

$$ISF_{KF} = 25 \cdot \left(\frac{L_s}{D_{eq}}\right)^{-0.75} \quad (13)$$

Based on the dataset used for the later studies (see Table 5), the standard lateral interface stiffness factor and lateral skin stiffness for varying spacing-diameter ratio is plotted in Figure 7. As already noted the axial and lateral factors are the same.

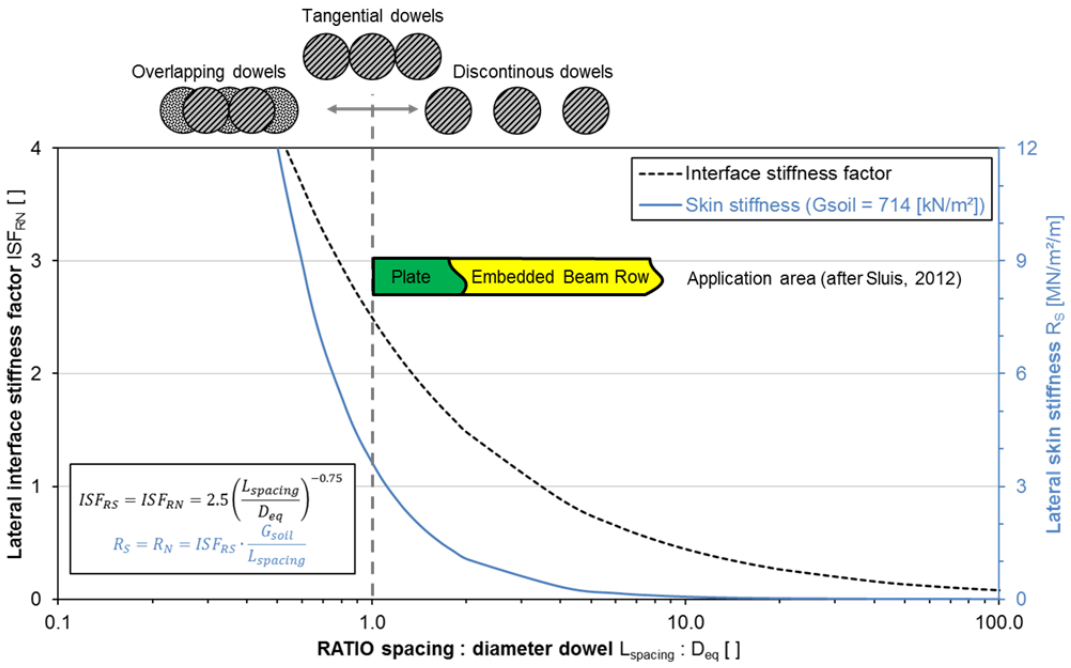

Figure 7 Lateral interface stiffness factor and skin stiffness

The material behaviour of an Embedded Beam Row and a plate are the same. The relationship of stresses and strains are defined by (Brinkgreve et al., 2016b):

$$\begin{bmatrix}\sigma_N \\ \tau\end{bmatrix} = \begin{bmatrix}E & 0 \\ 0 & \kappa G\end{bmatrix}\begin{bmatrix}\varepsilon_N \\ \gamma\end{bmatrix} \quad (14)$$

σ_N	$\left[\frac{kN}{m^2}\right]$	Normal stress
τ	$\left[\frac{kN}{m^2}\right]$	Shear stress
E	$\left[\frac{kN}{m^2}\right]$	Young's Modulus
κ	[ ]	Shear correction factor $(5/6)$
G	$\left[\frac{kN}{m^2}\right]$	Shear Modulus ($G = \frac{E}{2(1+\upsilon)}$)
υ	[ ]	Poisson's ratio
ε_N	[ ]	Normal strain
γ	[ ]	Shear strain

The structural (internal) forces in an Embedded Beam Row are defined by (Brinkgreve et al., 2016b):

$$N = E \cdot \varepsilon_N \cdot A \quad (15)$$

$$Q = \frac{\kappa \cdot E \cdot A}{2 \cdot (1+\upsilon)} \cdot \gamma^* \quad (16)$$

$$M = E \cdot I \cdot \kappa \quad (17)$$

N	$[kN]$	Normal force
A	$[m^2]$	Profile area
Q	$[kN]$	Shear force
M	$[kNm]$	Bending moment
I	$[m^4]$	Moment of inertia

The modified shear strain γ^* takes some additional terms into account, which gives a more accurate result (Brinkgreve et al., 2016b).

Based on the equations (7) and (8) the normal and shear stresses of the Embedded Beam Row are defined by (Brinkgreve et al., 2016b):

$$\begin{bmatrix} t_s \\ t_n \end{bmatrix} = \begin{bmatrix} R_s & 0 \\ 0 & R_n \end{bmatrix} \begin{bmatrix} u_s^p - u_s^s \\ u_n^p - u_n^p \end{bmatrix} \quad (18)$$

t_s	$\left[\frac{kN}{m^2}\right]$	Shear stress
t_n	$\left[\frac{kN}{m^2}\right]$	Normal stress
$u_s^p - u_s^s$	$[m]$	Displacement between pile and soil in axial direction
$u_n^p - u_n^s$	$[m]$	Displacement between pile and soil in lateral direction

The derivation of the interaction of soil and pile at the bottom is similar. Only tension is allowed at the foot of the pile (Brinkgreve et al., 2016b).

$$F_{bot} = K_f \cdot (u^p_{foot} - u^s_{foot}) \quad (19)$$

F_{bot}	$\left[\frac{kN}{m}\right]$	Force at bottom
$u^p_s - u^s_s$	$[m]$	Displacement between pile and soil at foot

These stresses are limited by the maximum forces in the related direction. When the maximum force in a certain direction is reached, perfectly plastic behaviour is postulated (Brinkgreve et al., 2016b).

Additionally an elastic zone with the equivalent radius is surrounding the foot of the pile (see Figure 8 after Sluis, 2012).

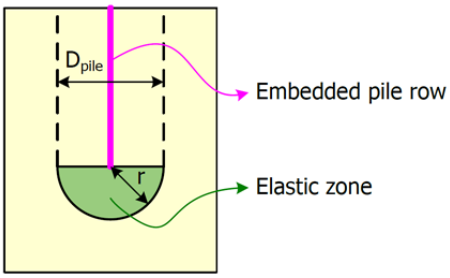

Sluis (2012)

Figure 8 Elastic zone around pile foot (Sluis, 2012)

Note that the PLAXIS manual (Brinkgreve et al., 2016b) explicitly indicates that the Embedded Beam Row is not fully capable to model horizontal loading:

> *"…Embedded Beams may not show fully realistic behaviour when subjected to transverse forces" (page 209)*

The Embedded Beam Row gives the option to choose between the behaviour of piles or rock bolts. The behaviour of those is the same, only the selection of the connection point is different. The pile behaviour allows selecting the top or bottom as connection point. If the top is set as connection point, the point with the largest Y-value is defined as connection point, regardless of the drawing order. If the behaviour as rock bolt is chosen, the connection point is dependent of the drawing order (set as first or second). The rock bolt behaviour was implemented mostly for the usage in tunnel design. Generally the pile behaviour is assigned (Brinkgreve et al., 2016b).

The Embedded Beam Row allows defining the fixation of the top or bottom point (standard PLAXIS setting: top). The possible connectivity options are rigid, hinged and free (standard PLAXIS setting: rigid). A rigid fixation means that the deformation and rotation of the connection point between soil and Embedded Beam Row are the same. Thus there is no differential strain and rotation between Embedded Beam Row top and the connected soil point (differential strain $\Delta\varepsilon = 0$, differential rotation $\Delta\omega = 0$). The deformation and rotation with a free connection are different for the soil and Embedded Beam Row point and governed by the axial and lateral stiffness factors ($\Delta\varepsilon \neq 0$, $\Delta\omega \neq 0$). A hinged connectivity fixes only the deformation and allows differential rotation ($\Delta\varepsilon = 0$, $\Delta\omega \neq 0$).

PLAXIS applies certain assumptions and simplifications to the behaviour of an Embedded Beam Row. An Embedded Beam Row located in a linear elastic cluster ignores the specified spacing and shaft resistance. This is based on the assumption that clusters with linear elastic behaviour are structures not soil. The connection is rigid and a punching through is prevented. Also the connection of structures sharing a geometry point is by default rigid when both are activated. When an interface exists, the Embedded Beam Row is not connected to this (Brinkgreve et al., 2016a).

2.4 Safety analysis in PLAXIS

The safety analysis in PLAXIS (Phi/c reduction) is selected as calculation type in the staged construction mode. This approach reduces the strength parameters until a failure occurs. The safety factor is defined by equation (20), which is basically the same as described in chapter §2.1.2. This notation includes the undrained shear strength s_u and possible tensile strength. The dilatancy angle is not reduced, but it cannot be larger than the reduced friction angle. Elastoplastic strength parameters of structures can be reduced as well by applying the strength reduction in the selection explorer. The safety analysis starts with $\Sigma M_{sf} = 1$ and is increased successively in the load advancement procedure. The procedure will continue till a defined amount of steps is reached, or is cancelled by the user. The default value of steps is 100, an amount up to 10’000 steps could be necessary. For the calculation of the first step the increment of the strength reduction Msf can be defined, the default value is $Msf = 0.1$. The user can choose between two loading types. The safety factor is reduced incrementally by selecting the option ‘incremental multipliers’. In the ‘Target SumMsf’ the calculation will terminate when the target safety factor is reached.

For the interpretation of the result it is necessary to evaluate the progress of the safety factors curve per step. It is recommended to choose a curve point in the slope before the calculation is performed to obtain a deformation progress. In most cases the toe point is chosen. The curve point can be easily selected by tipping '__*selectcurvepoints*' and the coordinates in the command line of the mesh mode. It is necessary to use the 'Arc-length control' in safety analysis since this is the technique which makes this procedure robust (see Brinkgreve & Bakker, 1991). The tolerated error of the safety analysis should not exceed $1\,\%$. When advanced soil models are assigned in PLAXIS safety analysis, the material model is switched to Mohr-Coloumb. Hardening effects and stress-dependent stiffness behaviour are excluded from the analysis. The soil models Cam-Clay and Sekiguchi-Ohta (but also Linear Elastic) do not contain the friction angle and cohesion as strength parameters; therefore no strength reduction can be applied. In the NGI-ADP all undrained parameters and in the Jointed Rock all strength parameters in every plane are reduced. The Safety Analysis cannot be adapted with user-defined soil models, Brinkgreve et al (2016a).

$$\Sigma M_{sf} = \frac{\tan\varphi'_{input}}{\tan\varphi'_{reduced}} = \frac{c'_{input}}{c'_{reduced}} = \frac{s_{u,input}}{\mathrm{s_{u,reduced}}} = \frac{\mathrm{Tensile\ strength_{input}}}{\mathrm{Tensile\ strength_{output}}} \qquad (20)$$

2.4.1 Phases

In the staged construction the phases are defined. In the 'Initial phase' the initial stresses are calculated. These stresses are dependent on the soil weight, the water conditions and the formation history. Two procedures are used to obtain the initial stress state. In the 'K0 procedure' the stresses are derived by the earth pressure coefficient $\mathrm{K_0}$. This coefficient defines the ratio between the vertical and horizontal stresses. The vertical stresses are derived by the soil weight and the depth ($\sigma_v = \gamma \cdot z$), the horizontal stresses are determined by the ratio and the vertical stress ($\sigma_H = \sigma_v \cdot \mathrm{K_0}$). The stresses of a soil model with non-horizontal soil or water surfaces would not be in equilibrium, in this cases a 'Plastic nil--step' has to be added. In a Plastic nil-step the soil model from the previous step is not changed and no additional load is applied. In this phase the soil stresses can rearrange till equilibrium is obtained. The deformations should be reset ('Reset displacement to zero') after a Plastic nil-step to ensure that the deformations do not affect the subsequent stages. The adequate procedure to derive the stresses in non-horizontal soil model (like a slope) is the 'Gravity loading'. Basically this procedure equals the 'Plastic Calculation', the soil self-weight is increased from $\Sigma M_{weight} = 0$ to 1.

The gravity loading does not consider the over consolidation rate OCR and pre overburden pressure POP. In this case the K0 procedure followed by a Plastic nil-step should be used. The stresses obtained from Gravity Loading and K0 procedure with Plastic nil-step should be the same, when no over consolidation rate and pre overburden pressure is defined, Brinkgreve (2016a).

In the numerical study the initial phase is calculated by Gravity loading. The initial phase is followed by a Plastic phase of placing the piles wished-in-place. The Embedded Beam Row is activated. The displacements in this phase are set to zero to ignore settlements from the initial phase. After the placement of the pile the stability of the supported slope is derived. The settlements are reset again. The number of steps of the safety analysis is set to 1’000 steps.

3 Homogeneous slope

This chapter evaluates the behaviour of the Embedded Beam Row in a homogeneous slope without any water loads. First the unsupported slope is analysed in chapter §3.1. A comparative analysis with a plate element is described in chapter §3.2. The influence of the individual parameters of the Embedded Beam Row is investigated in chapter §3.3. The results are compared with the outcome taken from a three dimensional analysis. Conclusions are made in chapter §3.6.

3.1 Unsupported slope

The slope has a height of $10\,\mathrm{m}$ and a slope angle of $30°$.The model is presented in Figure 9. The soil parameters are summarised in Table 1 and based on a real case history. The mesh is refined in the area of failure; see the coarseness factors in Figure 9.

Table 1 Soil properties of the homogeneous soil model

Parameter	**Name**	**Klei**	**Unit**
Material model	-	Mohr-Coulomb	-
Unsaturated specific weight	γ_{unsat}	16	$\left[\frac{kN}{m^3}\right]$
Saturated specific weight	γ_{sat}	16	$\left[\frac{kN}{m^3}\right]$
Young's modulus	E'	2'000	$\left[\frac{kN}{m^2}\right]$
Poisson's ratio	ν'	0.4	[ ]
Cohesion	c'_{ref}	10	$\left[\frac{kN}{m^2}\right]$
Friction angle	φ'	15	[°]
Dilatancy angle	ψ	0	[°]

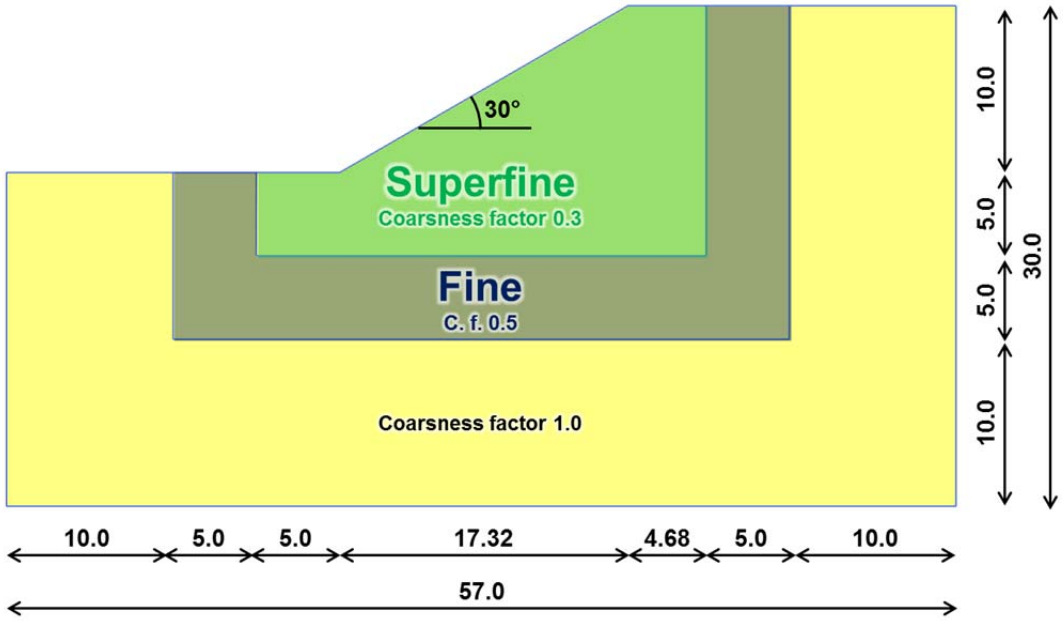

Figure 9 Homogeneous soil profile without water loads

3.1.1 Influence of the mesh

The result obtained from a phi/c reduction is influenced by the mesh size, element type and convergence tolerances (Tschuchnigg et al. 2015). All the two dimensional calculations are modelled by 15-noded high-order elements. The tolerance is kept on the default value (1 %). An investigation on the dependence of the mesh is done to optimise the calculation time, without affecting the calculation quality. The mesh is varied from a coarse mesh to a very fine mesh (PLAXIS mesh value: 0.01 to 0.07). The amount of steps is varied as well (100, 200 and 500 steps). The result of the variation with 500 steps is shown in Table 2. Figure 10 summarises the result with the different numbers of steps. The graph shows that the difference between the results is minimal. The calculation time is analysed in Appendix A. For the further calculations the mesh factor is fixed to 0.02. The chosen mesh is very fine. For practical application a coarser mesh could probably be chosen. The default amount of steps for the safety analysis in PLAXIS is 100 steps. The steps for the safety analysis are increased to 1'000 steps for all following calculations, to ensure that a proper failure mechanism is obtained in all cases. Figure 11 presents the failure of the chosen mesh (mesh factor 0.02). The validation of the mesh size including an Embedded Beam Row is performed in Appendix B.

Table 2 Result of the mesh variation

Mesh	Mesh factor	No. of soil elements	Minimal elem. area	Average elem. size	Safety factor
	[ ]	[ ]	[m²]	[m]	$\sum M_{SF}$[ ]
	0.01	33'581	< 0.01	0.2257	1.111
	0.02	8'481	0.02	0.449	1.110
v. fine	0.03	3'834	0.05	0.6678	1.109
fine	0.04	2'138	0.1	0.8943	1.109
	0.05	1'407	0.18	1.102	1.108
medium	0.06	995	0.25	1.311	1.107
	0.07	728	0.37	1.533	1.107
coarse	0.08	560	0.35	1.747	1.106

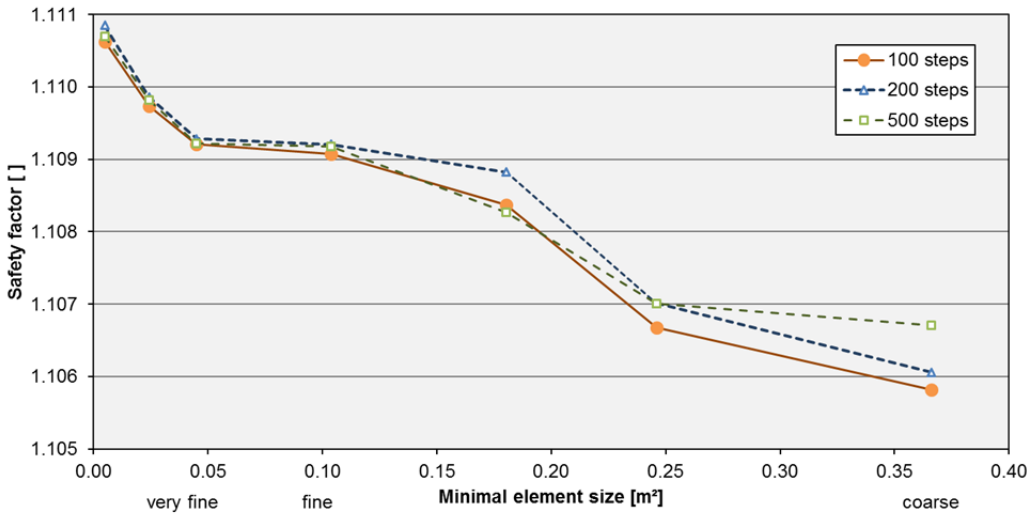

Figure 10 Safety factor vs. minimal element size

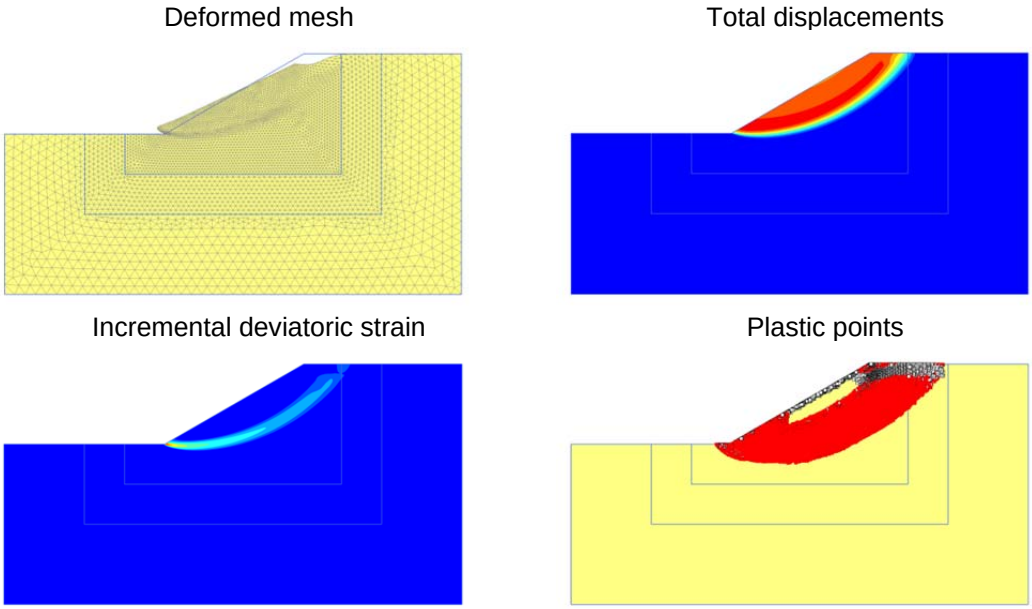

Figure 11 Visualisation of the failure mechanism (chosen mesh factor: 0.02)

3.1.2 Comparative calculations with limit equilibrium analysis

Calculations based on the limit equilibrium (with the software SLIDE) are done to derive comparative factors of safety. Also an associated analysis, where the dilatancy angle equals the friction angle ($\psi = \varphi$) is carried out. Figure 12 compares the failure line of the minimal safety factor obtained from SLIDE with GLE/Morgenstern-Price (red coloured line) with the failure line from the non-associated phi/c reduction (incremental deviatoric strains). Figure 13 compares the failure mechanisms of the associated ($\psi = \varphi$) and the non-associated ($\psi = 0$) calculation. The failure of the associated calculation is closer to the slope face. The results are summarised in Table 3.

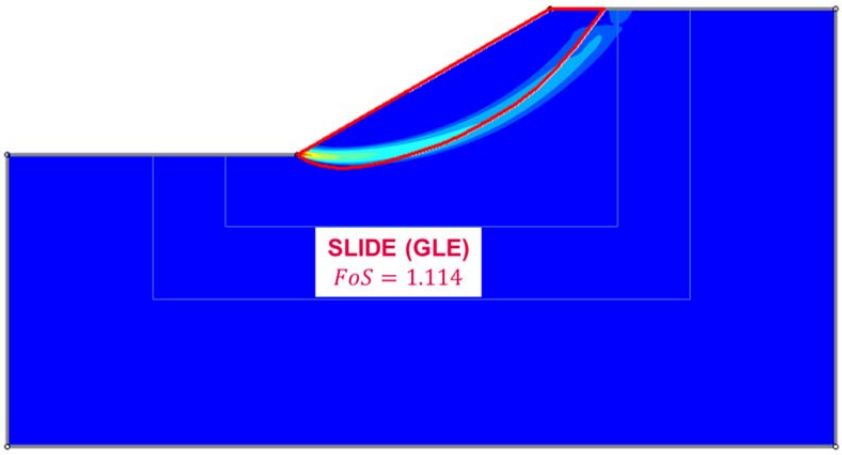

Figure 12 Failure line after GLE/Morgenstern (red line) and incremental deviatoric strains of the phi/c reduction in background (non-associated)

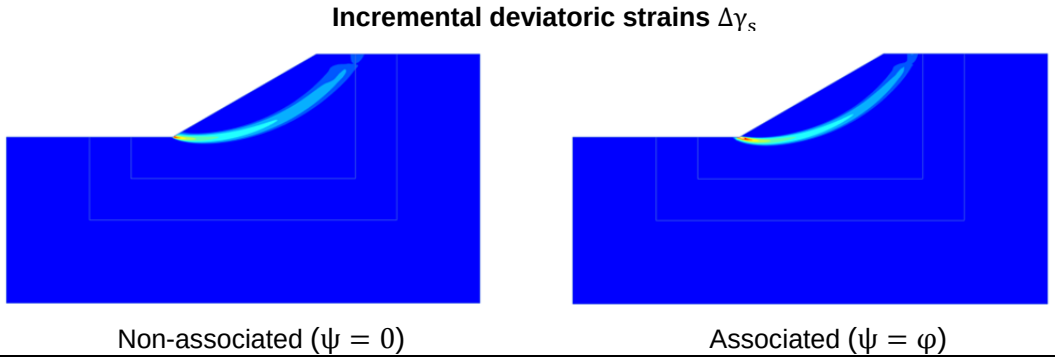

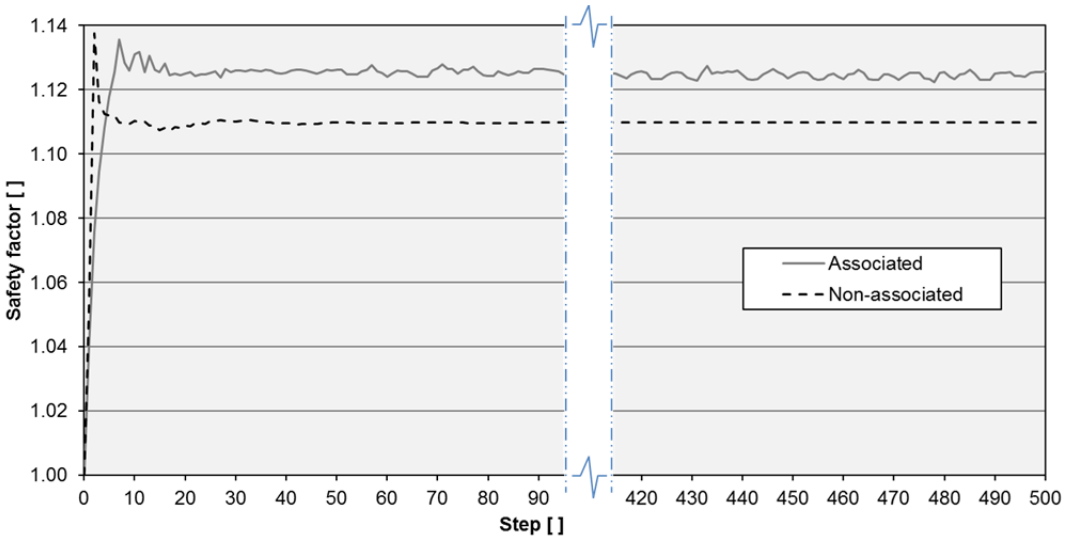

Figure 13 Incremental deviatoric strains and safety factor of the associated and non-associated safety calculation

Table 3 Safety factors for different calculation methods

Calculation method	**Circular failure line** $\Sigma M_{sf}[\,]$	**Non-circular failure line** $\Sigma M_{sf}[\,]$
PLAXIS: Phi/c reduction, non-associated ($\psi = 0$)	-	1.111
PLAXIS: Phi/c reduction, associated ($\psi = \varphi$)	-	1.125
SLIDE: GLE/Morgenstern-Price	1.131	1.114
SLIDE: Spencer	1.130	1.126
SLIDE: Janbu simplified	1.050*	1.027*
SLIDE: Bishop simplified	1.138	1.085*

*safety factors in general too small, see Wolffersdorff & Schweiger(2008)

3.2 Slope supported by plate element with interfaces

Calculations with a plate element with a length of $7.5\ \mathrm{m}$ are performed. The interface is set on 'Rigid' ($\mathrm{R_{inter}} = 1.0$). The parameters of the calculation are found in Table 4 and correspond to a doweled slope with an equivalent spacing of 1 meter (compare with Table 5).

Table 4 Plate parameters

Parameters	**Name**	**Plate**	**Unit**
Material type	-	Elastic	-
Isotropic	-	on	-
End bearing	-	off	-
Axial stiffness	$\mathrm{EA_1}$	2.0E6	$\left[\frac{\mathrm{kN}}{\mathrm{m}}\right]$
Axial stiffness out of plane	$\mathrm{EA_2}$	2.0E6	$\left[\frac{\mathrm{kN}}{\mathrm{m}}\right]$
Flexural rigidity	EI	4.0E4	$\left[\frac{\mathrm{kN\ m^2}}{\mathrm{m}}\right]$
Specific weight	w	0.6	$\left[\frac{\mathrm{kN}}{\mathrm{m}}/\mathrm{m}\right]$
Poisson's ratio	υ	0.2	[ ]

The failure mechanism is shown in Figure 14. However a close inspection shows that the failure mechanism is developed as a shallow failure in the slope above the pile and a safety factor of $\Sigma \mathrm{M_{sf}} = 1.168$ is obtained. Figure 14 also shows the internal forces of the plate resulting from the last step of the safety calculation. The blue and red lines indicate the maximal and minimal values. The maximal shear force is at a depth of $-4.85\ \mathrm{m}$ ($\mathrm{Q_{max}} = 21\ \mathrm{kN}$) which corresponds with the depth of the slip surface of the unsupported slope.

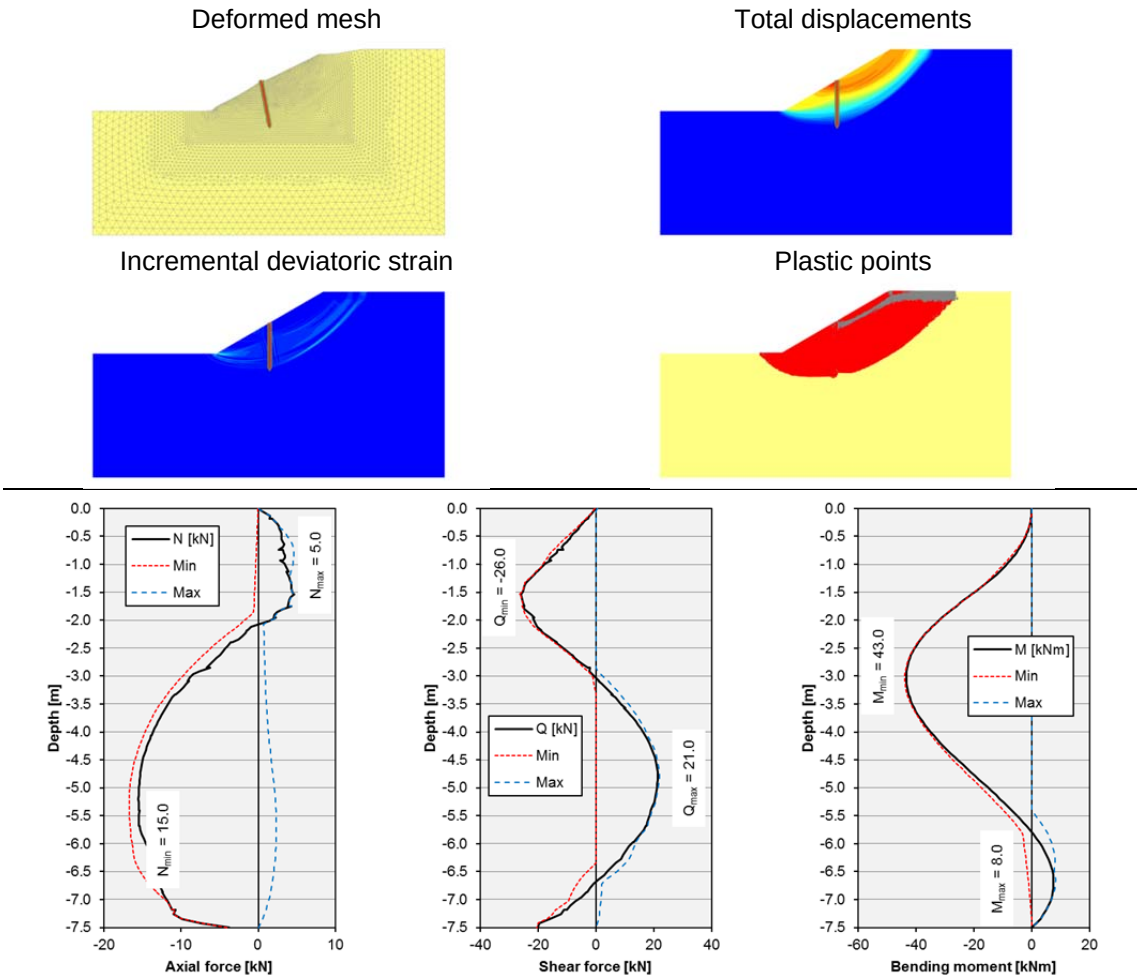

Figure 14 Failure mechanism of the slope supported by a plate

If the area at the surface of the slope is set elastic to force the failure beneath the pile, the result is shown in Figure 15. The safety factor obtained from this calculation is $\Sigma M_{sf} = 1.227$.

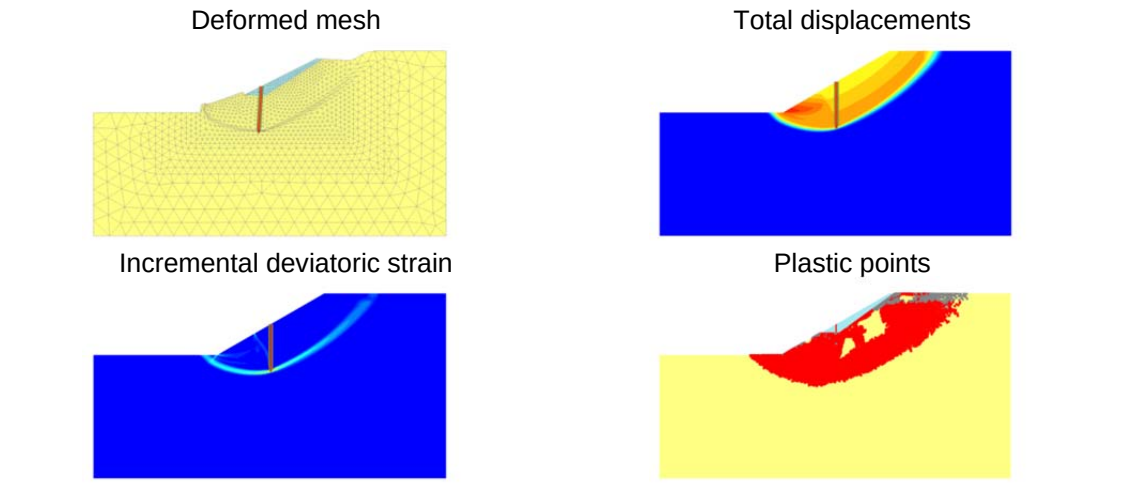

Figure 15 Failure mechanism of the plate supported slope with an elastic zone at the surface

3.2.1 Plate without interfaces

A single calculation is done by modelling the pile only with a plate (without interfaces). The standard approach is a plate with interfaces, which is used to model the soil-structure interaction properly. The safety factor obtained is $\Sigma M_{sf} = 1.175$. This safety factor is slightly larger than the one obtained by a plate with interfaces. The internal forces and the failure are almost identical, no major differences are recognised (Figure 16).

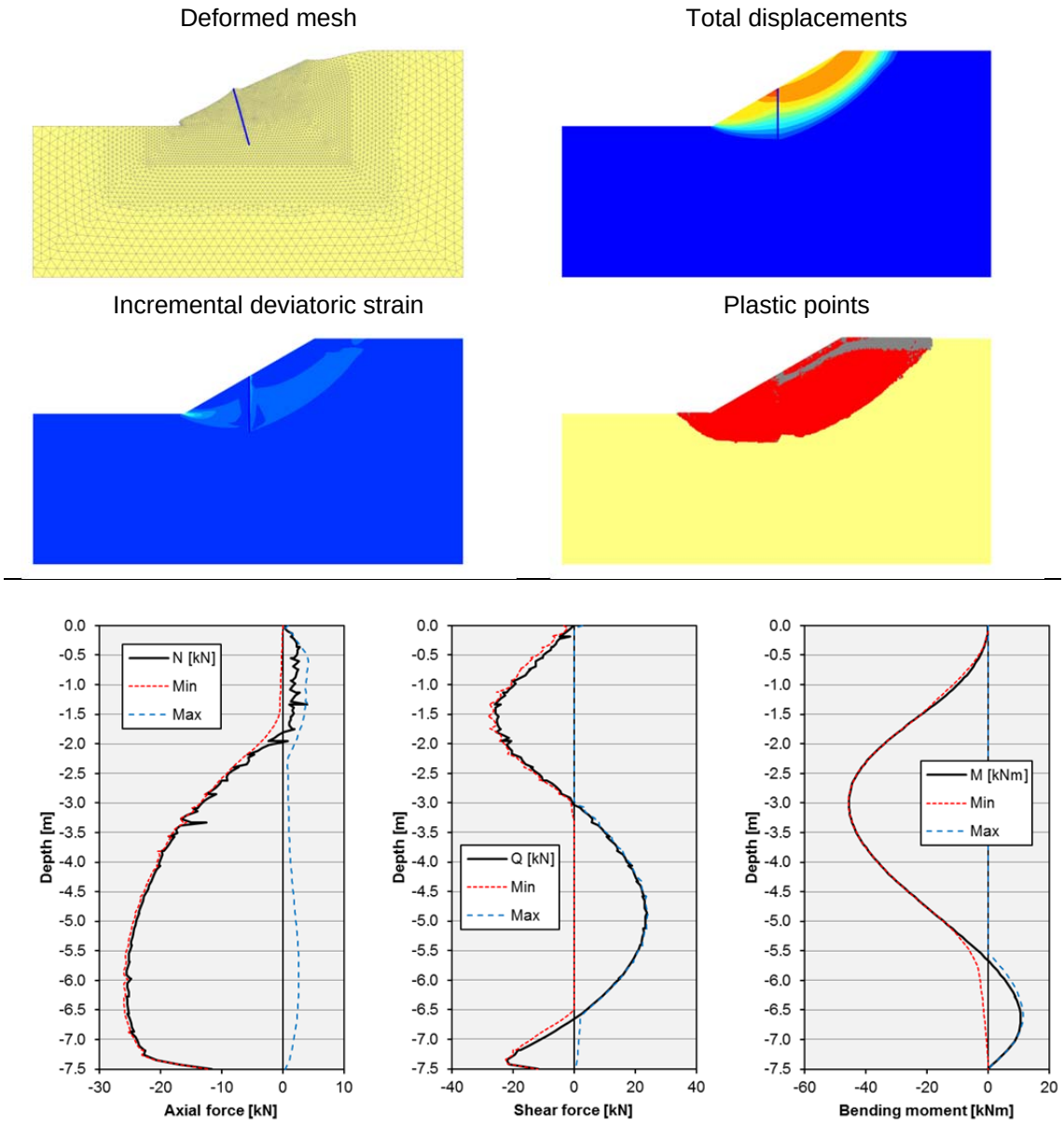

Figure 16 Failure mechanism of the slope supported only by a plate (without interfaces)

3.3 Slope supported by Embedded Beam Row

An Embedded Beam Row with a length of $7.5\ \mathrm{m}$ is installed in the middle of the slope (see Figure 17). The Embedded Beam Row parameters are chosen similar to the values from Grabe (2016). The axial and lateral skin resistance are set as linear constant values. If not noted different, the parameters for the calculation are the same as the parameters from Table 5.

Table 5 Embedded Beam Row parameters

Parameter	**Name**	**Embedded Beam Row**	**Unit**
Behaviour option	-	Pile	-
Connection point	-	Top	-
Connection	-	Rigid	-
Material type	-	Elastic	-
Young's Modulus	E	2.0E8	$\left[\frac{\mathrm{kN}}{\mathrm{m^2}}\right]$
Specific weight	γ	60.0	$\left[\frac{\mathrm{kN}}{\mathrm{m^3}}\right]$
Pile type	-	User-defined	-
Profile area	A	0.01	$[\mathrm{m^2}]$
Moment of inertia	I	2.0E-4	$[\mathrm{m^4}]$
Spacing	$\mathrm{L_{spacing}}$	1.0	$[\mathrm{m}]$
Axial skin resistance	$\mathrm{T_{skin}}$	10.0	$\left[\frac{\mathrm{kN}}{\mathrm{m}}\right]$
Lateral skin resistance	$\mathrm{T_{lat}}$	10.0	$\left[\frac{\mathrm{kN}}{\mathrm{m}}\right]$
Base resistance	$\mathrm{F_{max}}$	$0.01 \approx 0$	$[\mathrm{kN}]$
*specific weight is the difference between weight of the Embedded Beam Row and the soil			

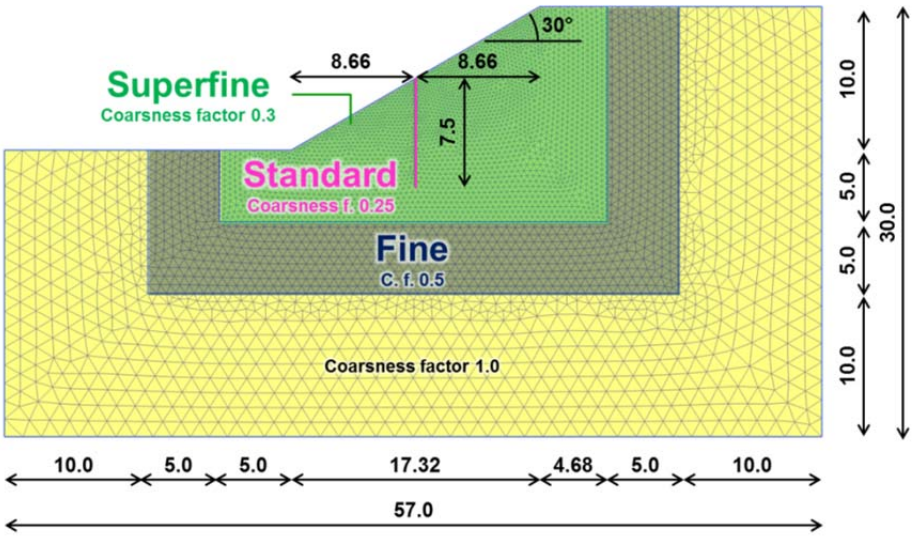

Figure 17 Homogeneous soil profile

The values taken from Grabe (2016) for the dowel correspond to a steel I-beam. An equivalent diameter can be calculated from the following equation taken from the PLAXIS manual (Brinkgreve, 2016a):

$$D_{eq} = \sqrt{12 \cdot \left(\frac{EI}{EA}\right)} = \sqrt{12 \cdot \left(\frac{I}{A}\right)} = \sqrt{12 \cdot \left(\frac{2 \cdot 10^{-4}\ m^4}{0.01\ m^2}\right)} \approx 0.5\ m \qquad (21)$$

D_{eq}	$[m]$	Equivalent diameter
E	$\left[\frac{kN}{m^2}\right]$	Young's Modulus
I	$\left[\frac{kN}{m^2}\right]$	Moment of inertia
A	$[m^2]$	Profile area

For elastoplastic calculations the plastic bending moment and plastic axial force need to be determined. The steel beam is a profile 'HP 360x84 S235':

$$N_{pl} = A \cdot f_{yd} = 2'500\ kN \qquad (22)$$

$$M_{pl} = w_{pl} \cdot f_{yd} = 350\ kNm \qquad (23)$$

N_{pl}	$[kN]$	Plastic axial force
M_{pl}	$[kNm]$	Plastic bending moment
w_{pl}	$[m^3]$	Pla. moment of resistance ($\mathrm{w_{pl}} = 1498\mathrm{cm}^3$ for HP360x84)
A	$[m^2]$	Profile area ($\mathrm{A} = 107\mathrm{cm}^2$ for HP 360x84)
f_{yd}	$\left[\frac{N}{mm^2}\right]$	Steal strength ($\mathrm{f_{yd}} = 235\,\frac{\mathrm{MN}}{\mathrm{m}^2}$ for S235)

The obtained safety factors for a dowel length of $7.5\,\mathrm{m}$ should all be between $\Sigma M_{sf} = 1.11 - 1.23$, based on the safety factor obtained for the unsupported slope in chapter §3.1 and supported by a plate in chapter §3.2. A verification of the upper limit is shown in Appendix C.

3.3.1 Axial and lateral skin resistance

In this chapter the axial and lateral skin resistance is discussed. It should be noted, that the symbol of the axial skin resistance is defined by T_{skin} (after Brinkgreve, 2016a). Some results of the variation of the lateral skin resistance are shown in Figure 18. The overall overview is given in Figure 19 on a logarithmic scale. The figure shows that by installing a weak dowel (with almost no skin resistance), the safety factor corresponds to the minimal safety factor from the unsupported slope as expected.

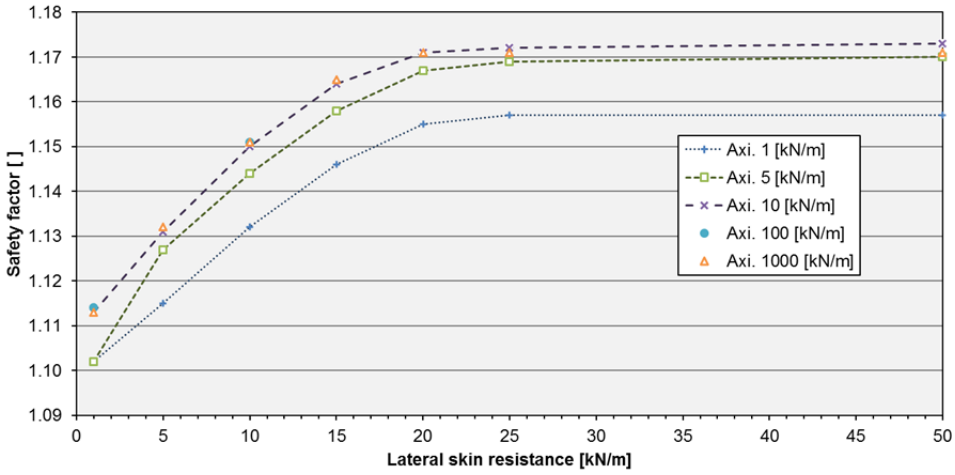

Figure 18 Variation of the lateral skin resistance (by different axial skin resistance)

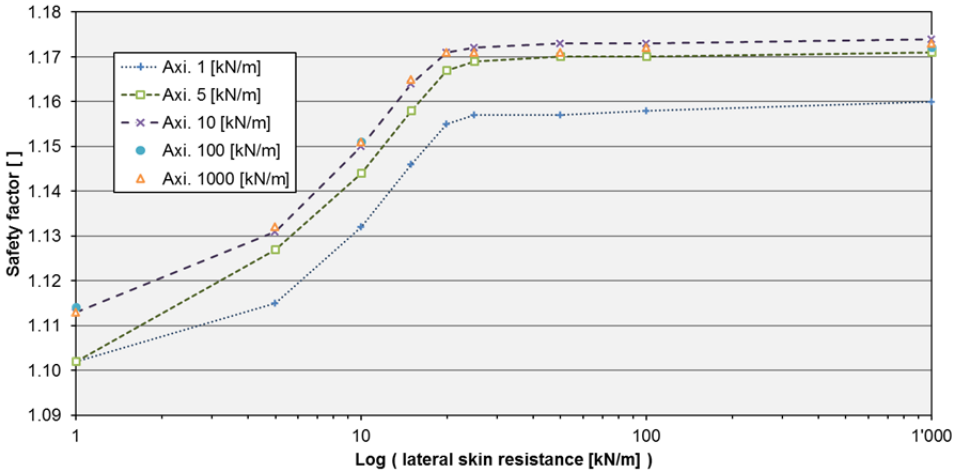

Figure 19 Overview of the variation of the lateral skin resistance on a logarithmic scale

The correlation between a weak dowel and the unsupported slope can also be shown in the failure mechanism of a weak dowel (Figure 20) by comparing the incremental deviatoric strains with Figure 11, where the failure mechanism is almost the same. Also the shear forces and the bending moment of a weak Embedded Beam Row are very low.

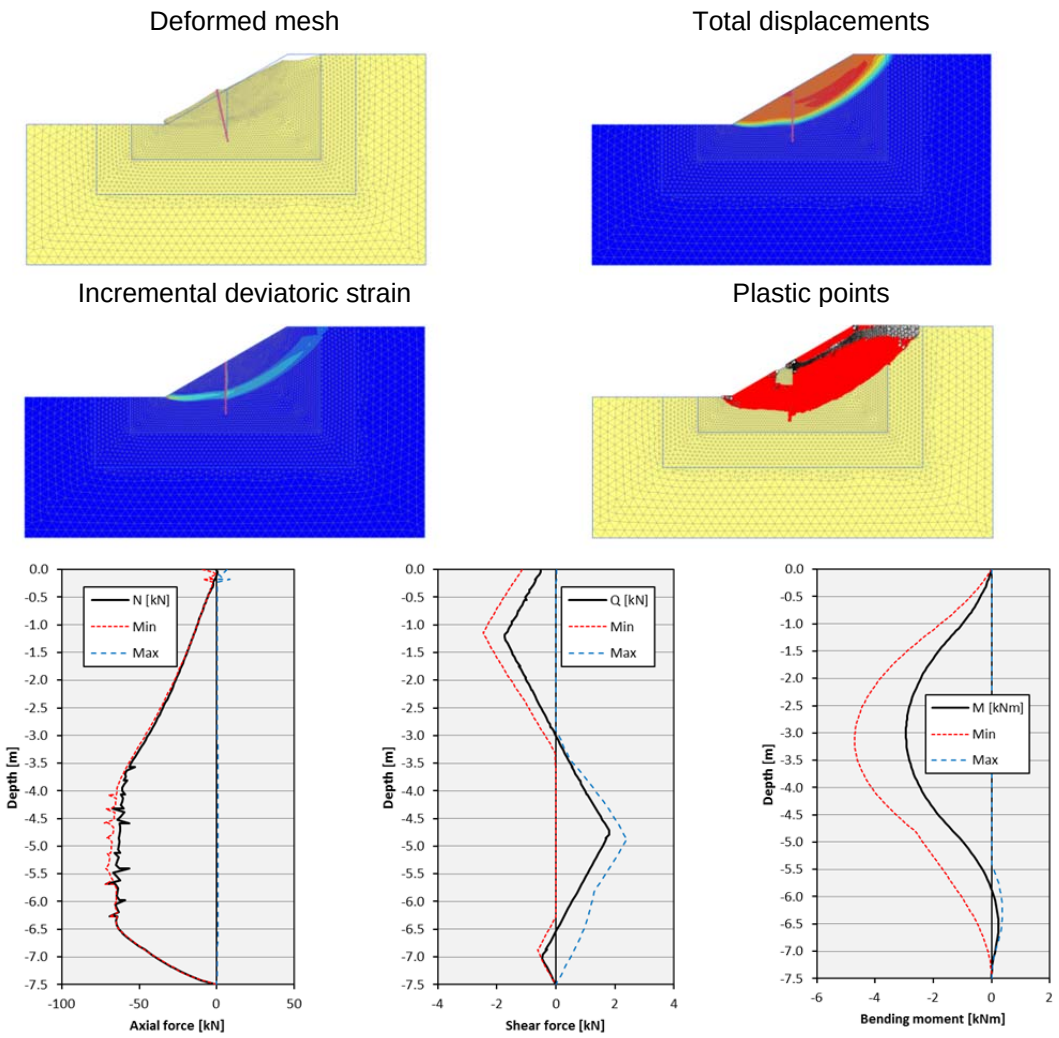

Figure 20 Failure mechanism of a 'weak' dowel (lateral skin resistance $T_{lat} = 1 \frac{kN}{m}$, axial skin resistance $T_{skin} = 1'000 \frac{kN}{m}$)

On the other hand the maximal reached safety factor (with high axial and lateral skin resistance) is similar to the safety factor derived from the analysis with a plate. The result is almost identical to the plate without interfaces (chapter §3.2.1). The failure mechanism of a strong dowel (Figure 21) is the same as the failure mechanism of the slope supported by the plate. Also the internal forces of the plate and the Embedded Beam Row correlate. The maximal shear force is at a depth of -4.9 m ($Q_{max} = 25$ kN), which corresponds to the depth of the slip surface of the unsupported slope.

Applying an elastic area on the surface of the slope above the Embedded Beam Row would result in the maximal safety factor obtained in Appendix C.

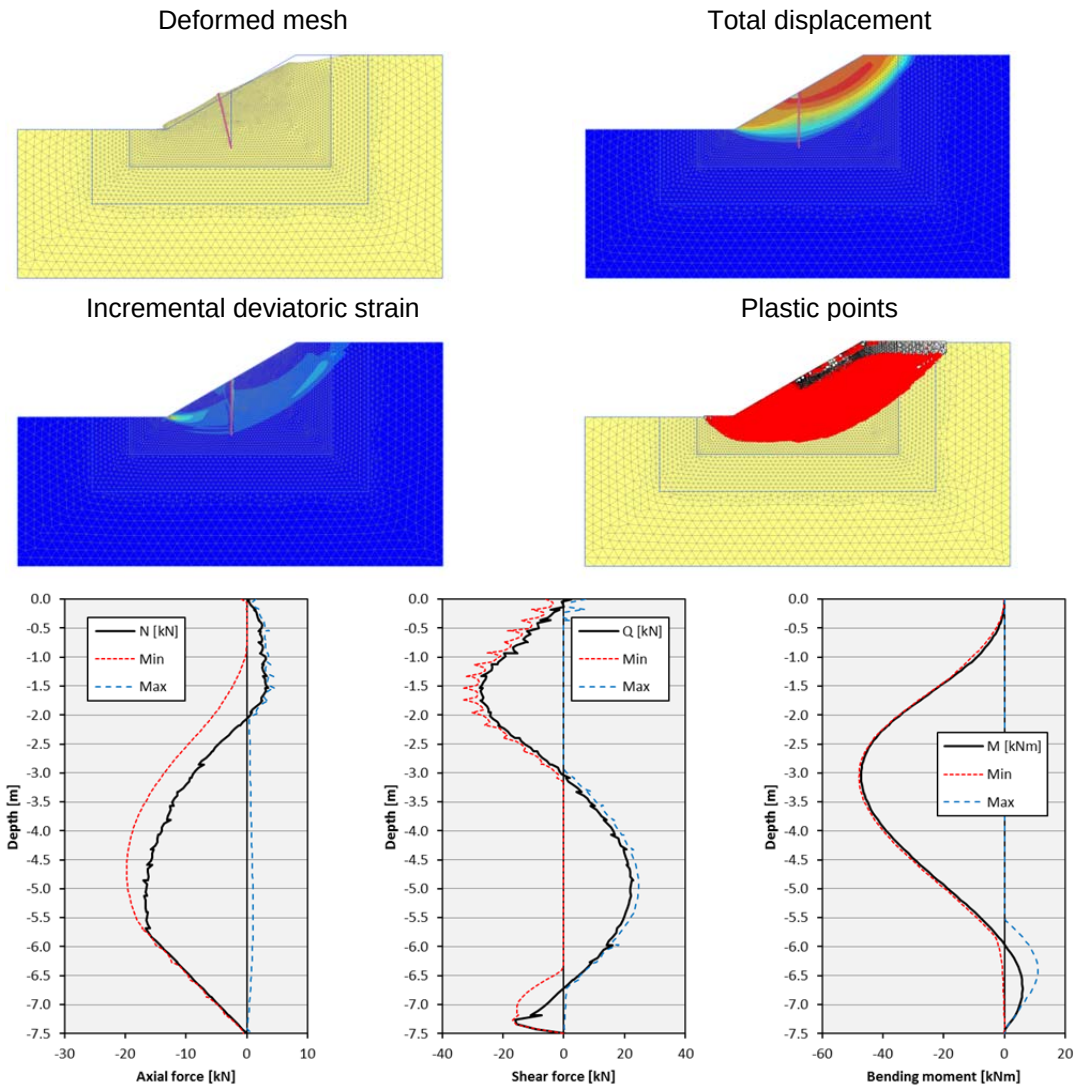

Figure 21 Failure mechanism of a 'strong' dowel (lateral skin resistance $T_{lat} = 100 \frac{kN}{m}$, axial skin resistance $T_{skin} = 10 \frac{kN}{m}$)

Figure 22 shows the internal forces of the Embedded Beam Row by variation of the lateral skin resistance and a constant axial skin resistance ($T_{skin} = 10 \frac{kN}{m} = const.$). The red and blue lines indicate the location and value of the maximum and minimum. The variation of the lateral skin resistance affects the axial and shear forces; as a consequence the bending moment is influenced as well. The gradient of the shear force is limited by the lateral skin resistance; this explains the linear shear force progression at a lateral skin resistance $T_{lat} = 1,\ 5$ and $10 \frac{kN}{m}$. The axial force of these three lines is almost identical and limited by the axial skin resistance $T_{skin} = 10 \frac{kN}{m}$.

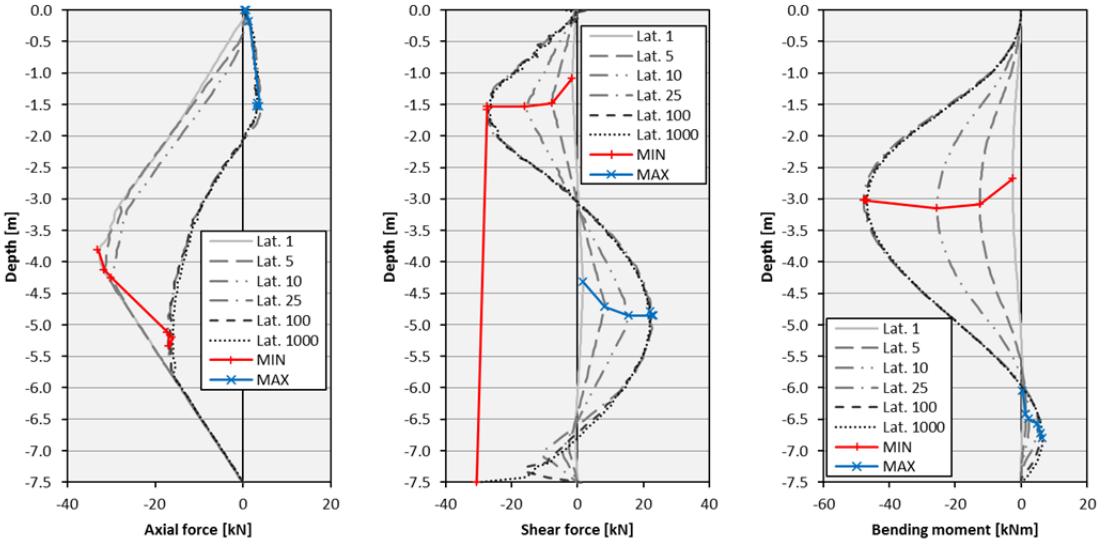

Figure 22 Internal forces of the Embedded Beam Row under variation of the lateral skin resistance ($T_{skin} = 10 \frac{kN}{m} = const.$)

This relationship is also shown in Figure 23, where the skin friction and the traction are plotted. The skin friction is limited by the axial skin resistance and the traction by the lateral skin resistance.

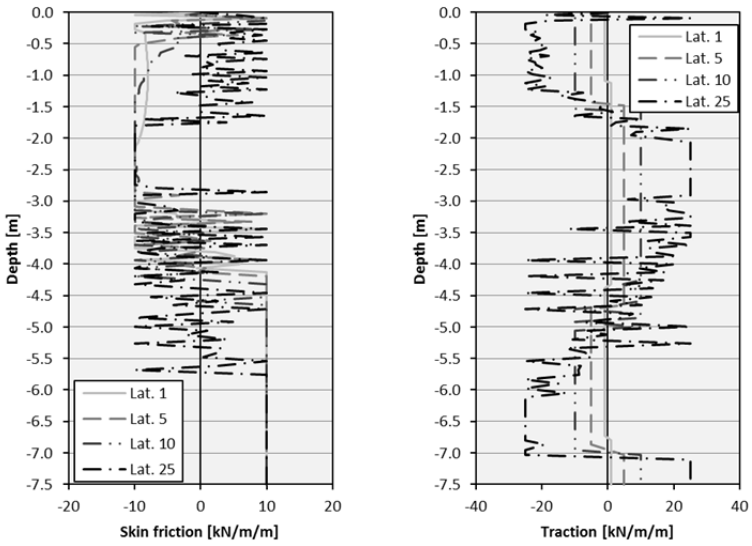

Figure 23 Skin friction and traction under variation of the lateral skin resistance ($T_{skin} = 10 \frac{kN}{m} = const.$)

The shear forces and bending moments of the lateral skin resistance from $T_{lat} = 25$ to $1'000 \frac{kN}{m}$ are identical; except the last $2\,m$ at the bottom differ. Also the effective horizontal forces (Figure 24) are identical.

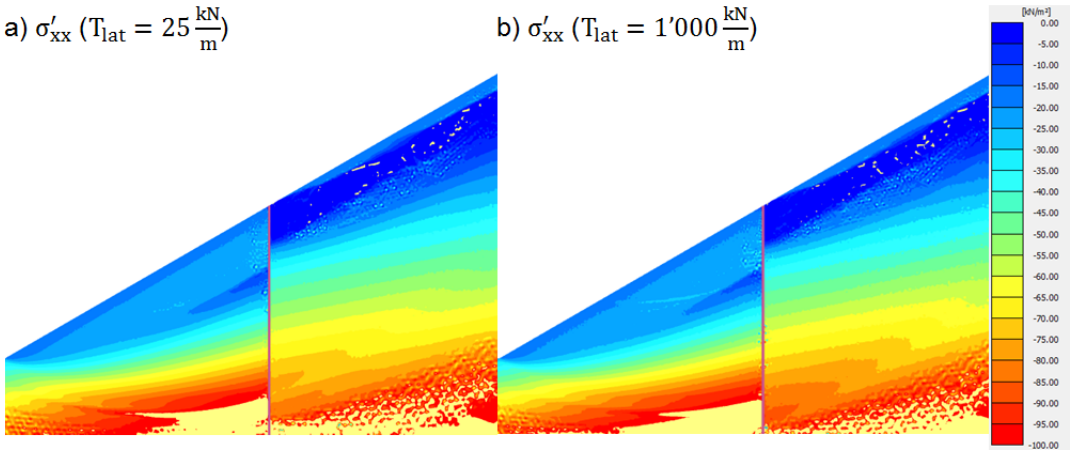

Figure 24 Effective horizontal stresses σ'_{xx} of a lateral skin resistance $T_{lat} = 25$ and $1'000 \frac{kN}{m}$

Figure 25 shows the failure mechanism depending on the lateral skin resistance. As already explained the Embedded Beam Row with a low lateral skin resistance behaves like an unsupported slope. At the lateral skin resistance of $T_{lat} = 25 \frac{kN}{m}$ the same surficial failure mechanism as in a plate occurs. This results in equal internal forces and safety factor for increasing lateral skin resistance.

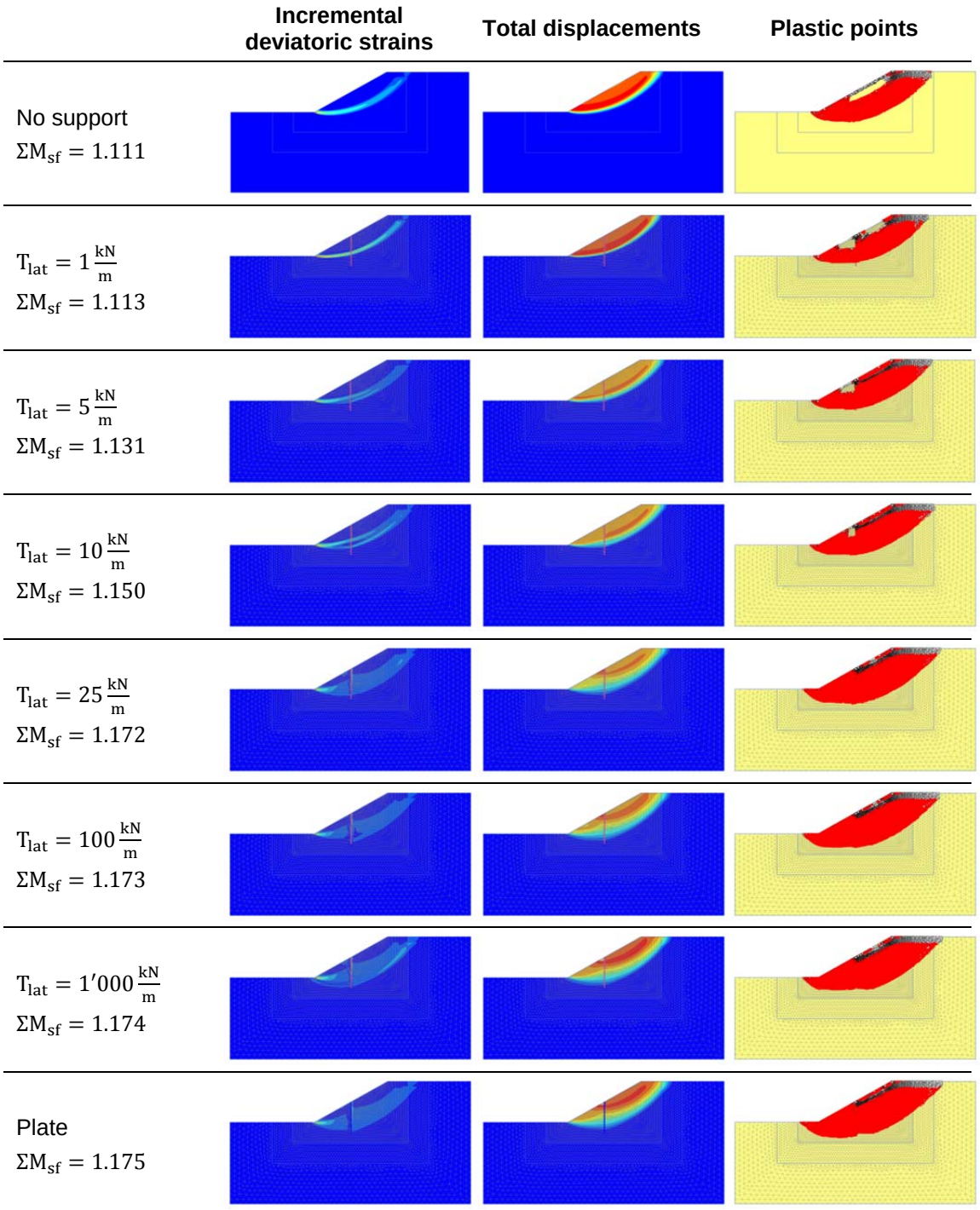

Figure 25 Failure mechanism depending on the lateral skin resistance (axial skin resistance $T_{skin} = 10 \frac{kN}{m}$)

Figure 26 shows the results as a function of the axial skin resistance. The same conclusions as made before can be observed. The axial skin resistance has almost no influence on the safety factor. The safety factor is the same between an axial skin resistance of $T_{skin} = 10$ and $1'000 \frac{kN}{m}$.

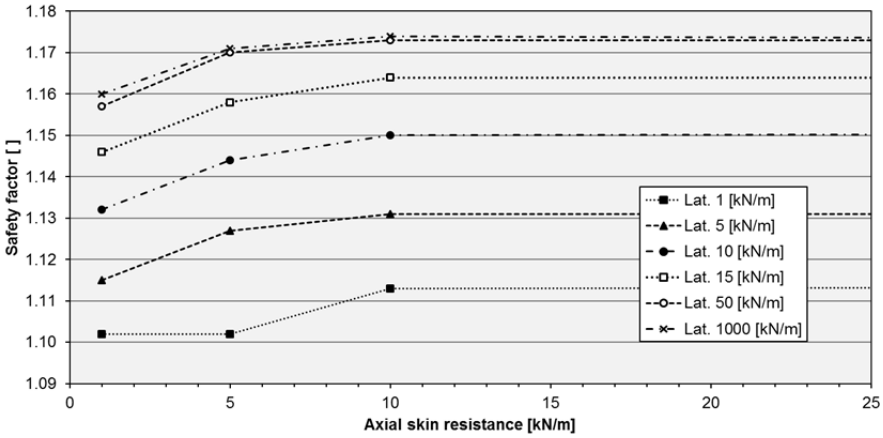

Figure 26 Variation of the axial skin resistance (by varying skin resistance)

Whereas Figure 22 showed the internal forces for varying lateral skin resistance, Figure 27 shows the internal forces by varying the axial skin resistance. The axial skin resistance only affects the axial forces. The shear forces are limited by the lateral skin resistance of $T_{lat} = 10 \frac{kN}{m}$. The inclination of the axial force is limited by the axial skin resistance for $T_{skin} = 1; 5$ and $10 \frac{kN}{m}$. The axial force for $T_{skin} = 100$ and $1'000 \frac{kN}{m}$ is limited by the same internal forces as obtained in the analysis with a plate.

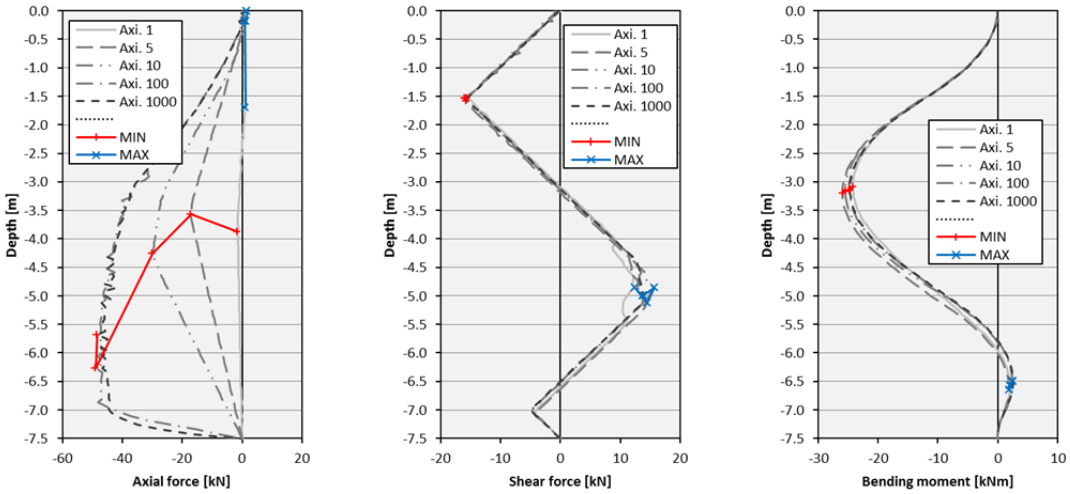

Figure 27 Internal forces of the Embedded Beam Row under variation of the axial skin resistance ($T_{lat} = 10 \frac{kN}{m} = const.$)

An ultimate calculation with unlimited lateral and axial skin resistances ($T_{lat} = T_{skin} = 10^{12} \frac{kN}{m}$) is performed to prove that the maximum safety factor is reached. The internal forces match as well with the one obtained through high lateral skin resistance in Figure 22.

When an elastic zone (Figure 28) is added on the slope above the Embedded Beam Row, the failure mechanism is pushed beneath the pile. The safety factor obtained ($\Sigma M_{sf} = 1.242$) is similar to the result from Appendix C and the plate with elastic zone.

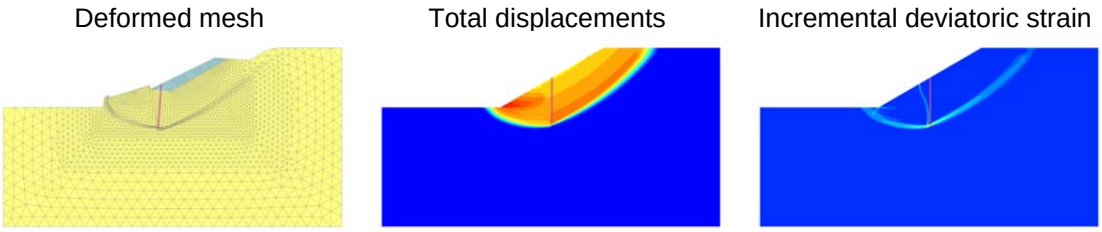

Figure 28 Failure mechanism of the Embedded Beam Row supported slope with an elastic zone at the surface

The principal behaviour of the Embedded Beam Row is correct since the upper limit corresponds with the plate element and the lower limit with the unsupported slope from chapter §3.1. Also the internal forces are consistent and are limited by the result of the plate and the skin resistance. The maximal shear force is at the depth of the failure of the unsupported slope.

3.3.2 Base resistance

The estimation of the influence of the base resistance (F_{max}) is evaluated on an Embedded Beam Row with a lateral skin resistance $T_{lat} = 10\ \frac{kN}{m}$ and an axial skin resistance of $T_{skin} = 1\frac{kN}{m}$. The safety factor of the various bases resistances is:

- $F_{max} = 0.01\ kN$: $\Sigma M_{sf} = 1.132$
- $F_{max} = 5\ kN$: $\Sigma M_{sf} = 1.132$
- $F_{max} = 10\ kN$: $\Sigma M_{sf} = 1.135$
- $F_{max} = 1'000\ kN$: $\Sigma M_{sf} = 1.135$

The base resistance has almost no influence as expected. Figure 29 shows the influence of the various axial skin resistances at a lateral skin resistance of $T_{lat} = 10\frac{kN}{m}$ and an axial skin resistance of $T_{skin} = 1\frac{kN}{m}$. The failure mechanism is only plotted for a base resistance of $F_{max} = 0.01$ and $1'000kN$ since they are identical (Figure 29). The base resistance affects only the axial force. When the base resistance is set to $F_{max} = 0.01\ kN$, the axial force at the bottom of the Embedded Beam Row is limited and results in $N_{bottom} = 0.01\ kN$. When the base resistance is $F_{max} = 5\ kN$, the axial force at the bottom of the Embedded Beam Row is $N_{bottom} = 5\ kN$.

The axial force of $F_{max} = 10\ kN$ and $F_{max} = 1'000\ kN$ are identical, the base resistance is not confining the axial force anymore. The shear forces and the bending moments are identical.

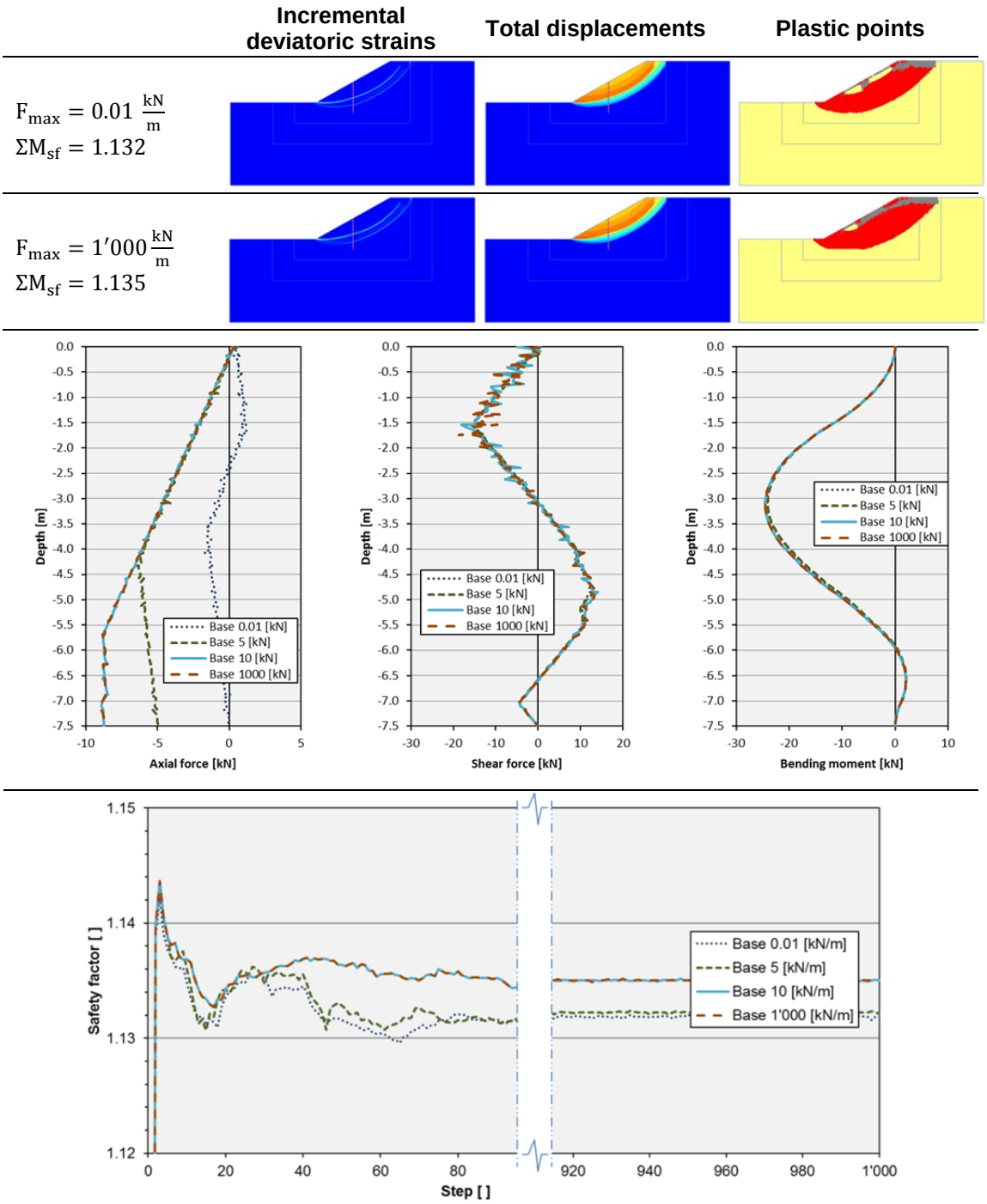

Figure 29 Failure mechanism depending on the base resistance (lateral skin resistance $T_{lat} = 10\ \frac{kN}{m}$; axial skin resistance $T_{skin} = 1\ \frac{kN}{m}$)

The base resistance only affects the axial forces at the bottom of the Embedded Beam Row. The influence on the safety factor is negligible.

3.3.3 Length

At a certain pile length no further improvement of the slope stability is possible, since a failure mechanism in front or behind the pile is decisive. The safety factor of the supported slope is limited by this failure mechanism. An improvement of the slope could only be obtained through more dowels in different positions. Figure 30 contains the variation of the length with a comparative analysis with SLIDE, under the assumption of a 'micro-pile' with almost infinite shear strength (spacing $a = 0.5\ \mathrm{m}$; shear strength $\tau_{max} = 10^6 \mathrm{kN}$). The base, lateral skin and axial skin resistance of the Embedded Beam Row parameters are set high ($L_s = 0.5\ \mathrm{m}$, $T_{lat} = T_{skin} = F_{max} = 10^6$).

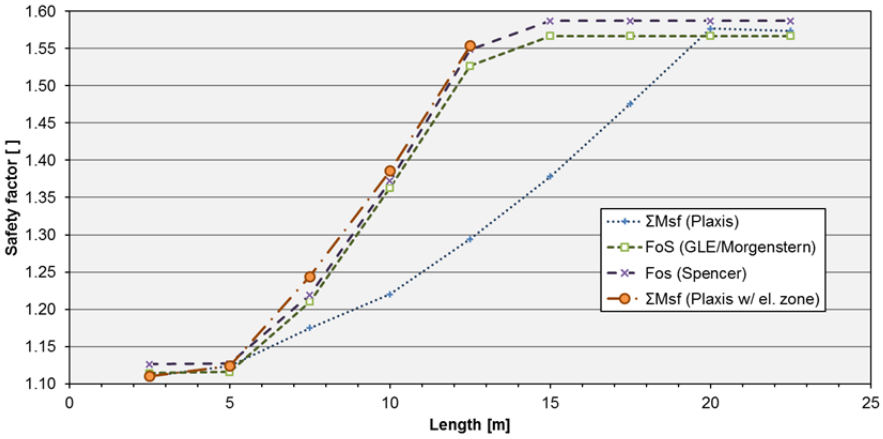

Figure 30 Variation of the dowel length

The figure shows that the limit analysis and phi/c reduction correlate when an elastic material behaviour is applied close to the surface to avoid the surficial failure. In cases where no elastic zone is defined, a smaller safety factor is obtained and the failure mechanism is different as well. When no further improvement is possible, the failure lines obtained from the limit analysis and phi/c reduction (Figure 31) agree well.

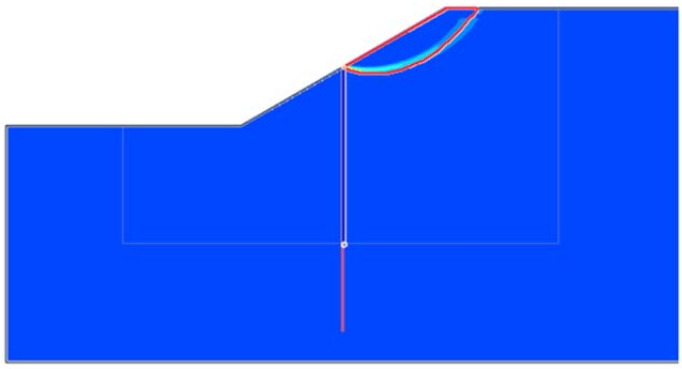

Figure 31 Failure line after GLE/Morgenstern (red line, dowel length $15\ \mathrm{m}$) and incremental deviatoric strains of the phi/c reduction in background (dowel length $22.5\ \mathrm{m}$)

3.3.4 Spacing

The aim of the Embedded Beam Row is to model the three dimensional effect in two dimensions. Chapter §2.3 explains formulas and background of the Embedded Beam Row. One conclusion made from chapter §3.3.1 and §3.3.2 is that the axial skin resistance and base resistance have almost no influence on the safety analysis. Therefore the axial skin resistance ($T_{skin} = 10 \frac{kN}{m}$) and the base resistance ($F_{max} = 0.01\ kN$) are kept constant for this evaluation.

A detailed view of the result is shown in Figure 32. The overall overview is shown on a logarithmic scale in Figure 33. Sluis (2012) describes the application area of the Embedded Beam Row with $\frac{L_{spacing}}{D} = 2$ to 8. Considering the equivalent diameter from chapter §3.3 ($D_{eq} = 0.5\ m$) the application area for our example would be a spacing of $L_{spacing} = 1$ to $4\ m$. The result seems reasonable in the limits of the application area. The results obtained from a spacing, larger than the application area ($L_{spacing} > 4\ m$), are unsatisfying. A realistic model would show no improvement at a large spacing.

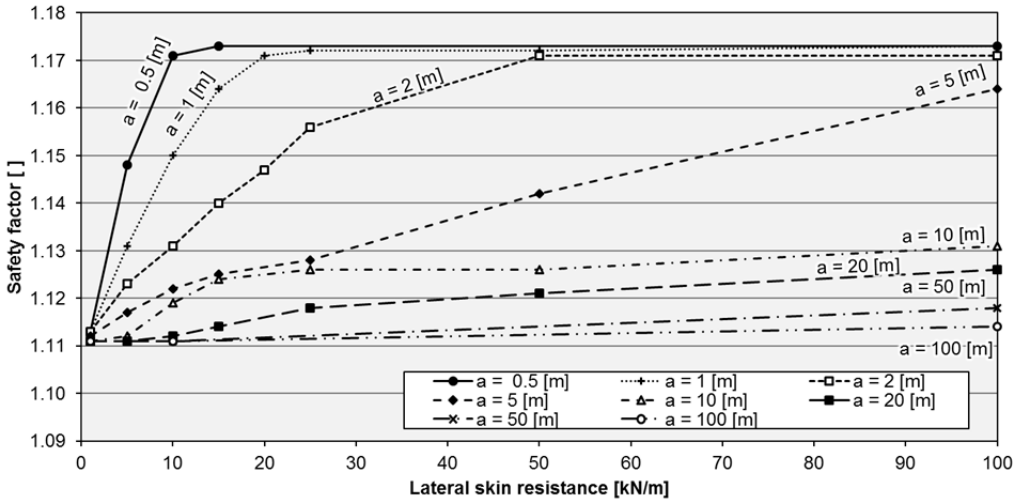

Figure 32 Variation of the axial skin resistance (by different spacing)

When the spacing and the lateral skin resistance are large, local failures near the head of the piles appear. Also numerical instabilities in the determination of the safety factor can be observed. This effect is shown in Figure 34 for a spacing of $L_s = 20\ m$ and a lateral skin resistance of $T_{lat} = 500 \frac{kN}{m}$. This can also be observed in the trend of the safety factor versus the steps which shows numerical instabilities. Data sets, where numerical instabilities appear, are marked red in Figure 33.

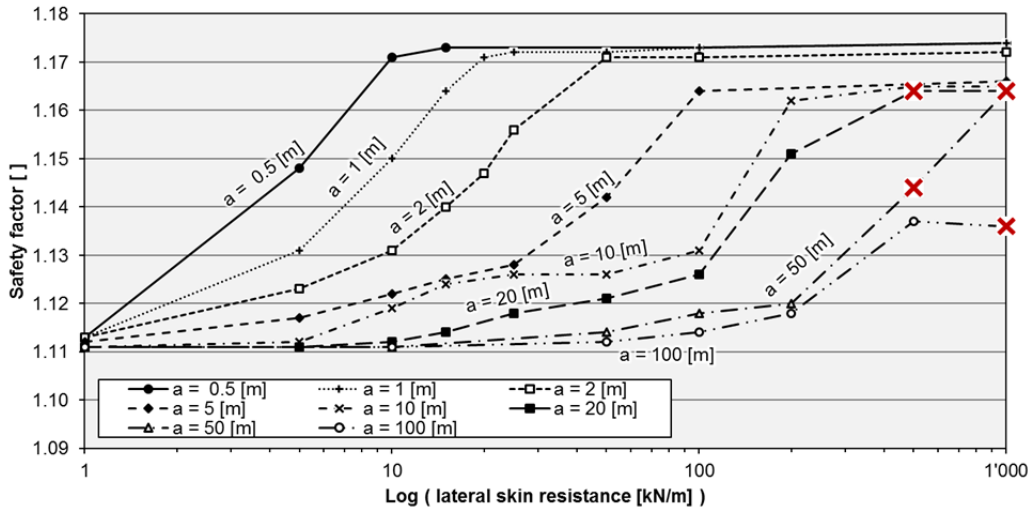

Figure 33 Overview of the variation of the spacing on logarithmic scale

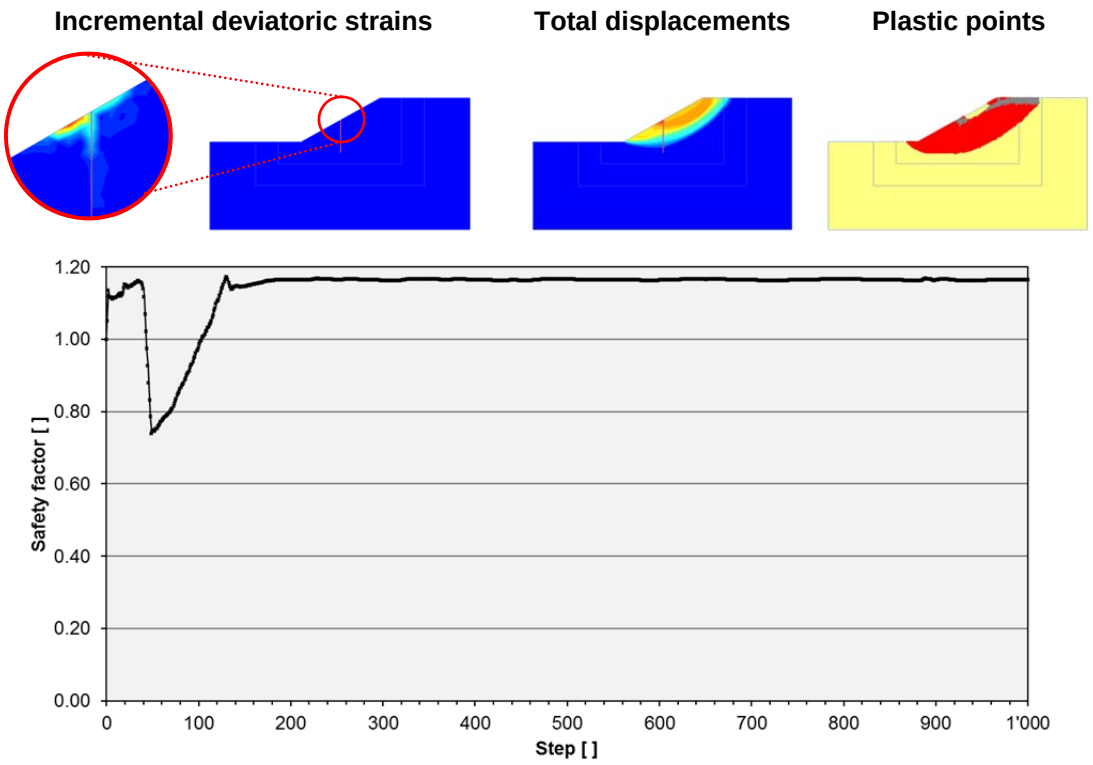

Figure 34 Local failure (spacing $L_s = 20\,\mathrm{m}$, lateral skin resistance $T_{lat} = 500\,\frac{kN}{m}$; axial skin resistance $T_{skin} = 10\,\frac{kN}{m}$)

The safety factor vs. spacing per lateral skin resistance is plotted in Figure 35.

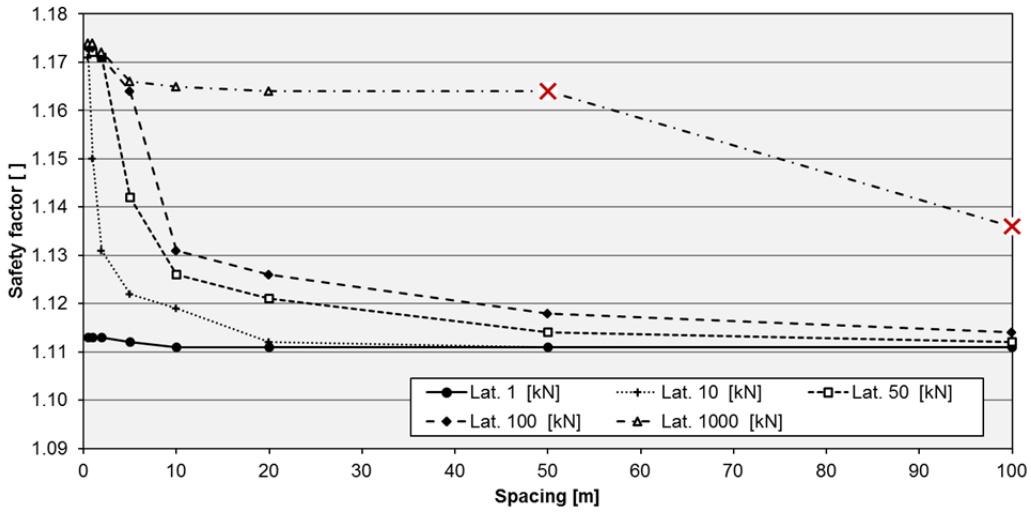

Figure 35 Safety factor vs. spacing per lateral skin resistance

Figure 36 shows the internal forces of the Embedded Beam Row at an axial skin resistance of $T_{skin} = 10 \frac{kN}{m}$ and a lateral skin resistance of $T_{lat} = 1'000 \frac{kN}{m}$ for the variation of the spacing. The shear force is always limited by the same internal forces as obtained from the plate element. The red line indicates the result obtained by a spacing of $L_s = 100\ m$ (red line) with numerical instabilities.

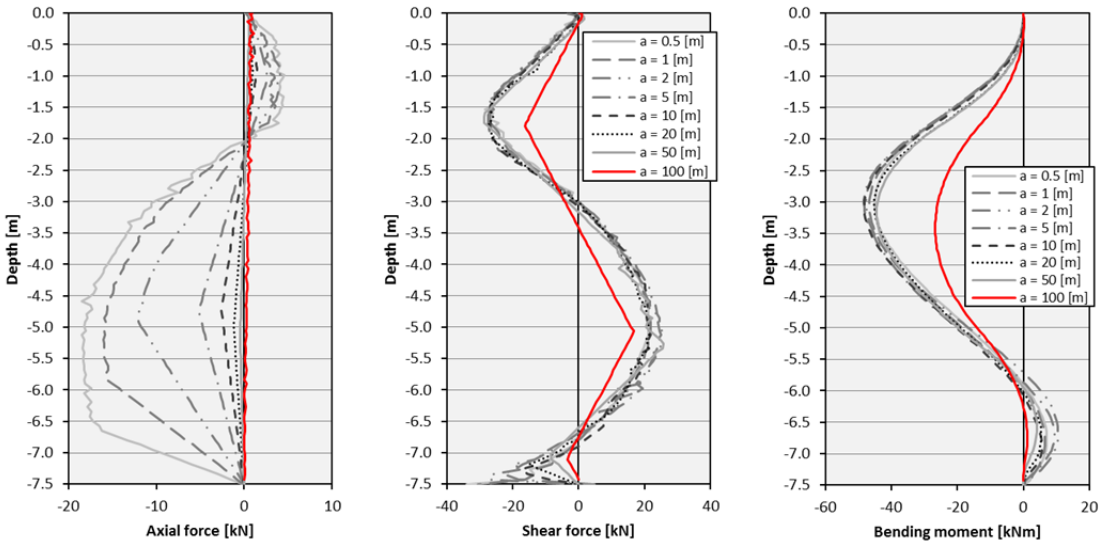

Figure 36 Internal forces of the Embedded Beam Row under variation of the spacing (Axial skin resistance $T_{skin} = 10 \frac{kN}{m}$, Lateral skin resistance $T_{lat} = 1'000 \frac{kN}{m}$)

The same variation of spacing like in Figure 36 is shown in Figure 37 for an equal lateral and axial skin resistance ($T_{lat} = T_{skin} = 10\,\frac{kN}{m}$). The internal forces decrease by a larger spacing. The inclination of the shear force at a lateral spacing of 1 meter is limited by the lateral skin resistance ($T_{lat} = 10\,\frac{kN}{m}$), as already observed in chapter §3.3.1. By varying the spacing, the inclination of the shear force is proportional to the spacing. At a spacing of 0.5 meter the maximal inclination of the shear force is $q_{max} = 20\,\frac{kN}{m}$, at a spacing of 10 m the maximal inclination is $q_{max} = 1\,\frac{kN}{m}$.

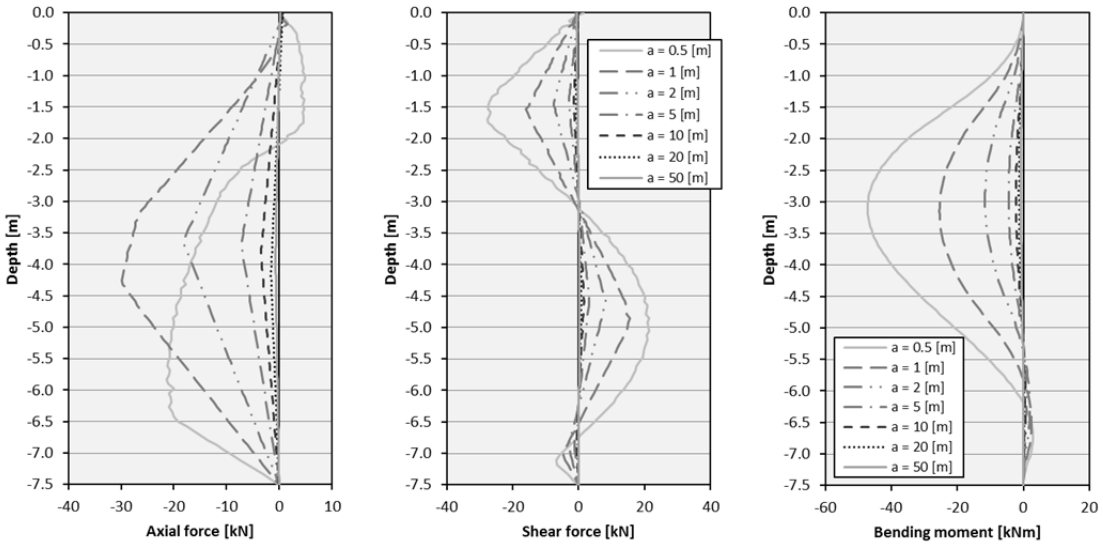

Figure 37 Internal forces of the Embedded Beam Row by variation of the spacing (axial and lateral skin resistance $T_{skin} = T_{lat} = 10\,\frac{kN}{m}$)

This relationship is also shown in Figure 38 by plotting the skin friction and traction. This means that the output of the internal forces is not meant per Embedded Beam Row but per unit of width. After revising the reference manual (Brinkgreve et al., 2016a) it is found that the skin force T_{skin} and the interaction force T_2 '*are expressed in the unit of force per unit of pile length and per unit of width in the out-of-plane direction*' (quotation Brinkgreve et al., 2016a, page 355). On the other hand the input data of the shaft resistance is defined in force per unit pile length (Brinkgreve et al., 2016a, page 207).

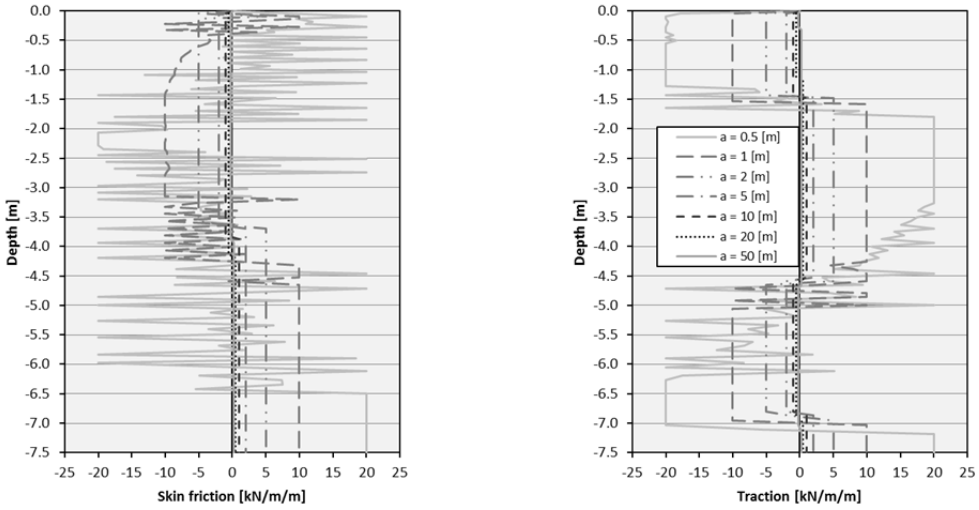

Figure 38 Skin friction and traction by variation of the spacing (Axial and lateral skin resistance $T_{skin} = T_{lat} = 10 \frac{kN}{m}$)

A short example: we pick the model with a spacing of $L_s = 0.5\,m$ from Figure 37. A spacing of $L_s = 0.5\,m$ is equivalent to two piles per meter. The skin friction and traction are $20 \frac{kN}{m}/m$. The output of traction and skin friction (Figure 38) is limited by this plastic shaft resistance. Figure 37 is updated and the internal forces are represented by internal forces per Embedded Beam Row in Figure 39. Now the internal forces are almost identical, except for a spacing of $L_s = 0.5\,m$, where the plastic shaft resistance is not reached.

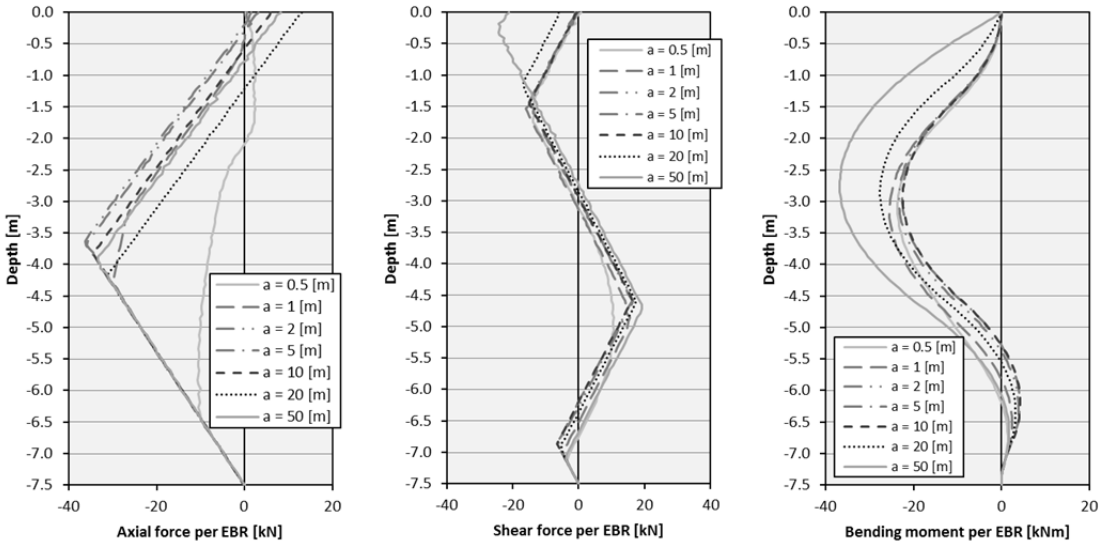

Figure 39 Internal forces per Embedded Beam Row by variation of the spacing (Axial and lateral skin resistance $T_{skin} = T_{lat} = 10 \frac{kN}{m}$)

Instead of plotting the safety factor against the lateral skin resistance per Embedded Beam Row (Figure 33), the safety factor is plotted against the lateral skin resistance per meter in Figure 40. The figure shows that the path of all lines is similar.

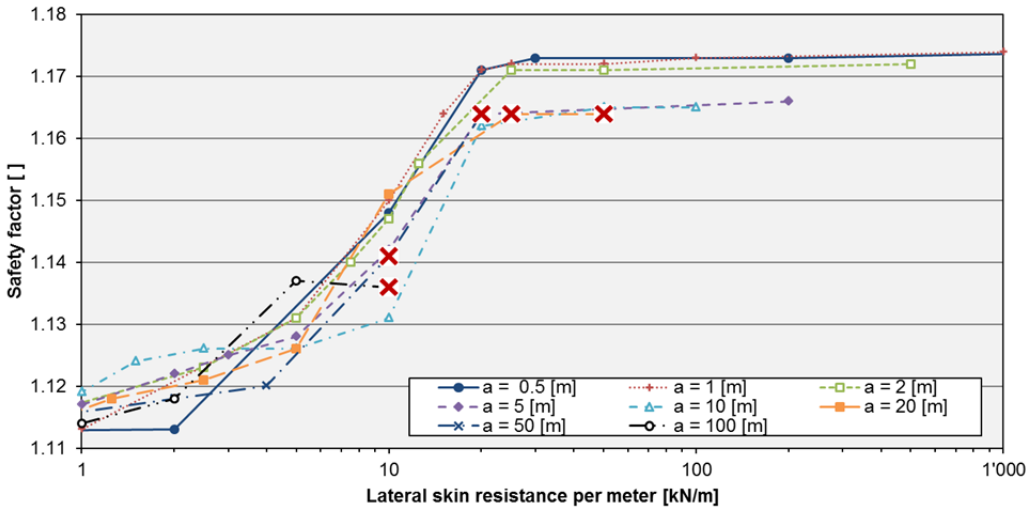

Figure 40 Safety factor vs. lateral skin resistance per meter

Figure 33 shows the safety factor by the variation of the spacing. The increase of the safety factor is not too large; therefore the variation of the spacing is repeated with a pile length of $20\ \mathrm{m}$ and with a spacing of $L_s = 1,\ 10$ and $100\ \mathrm{m}$ in Figure 41.

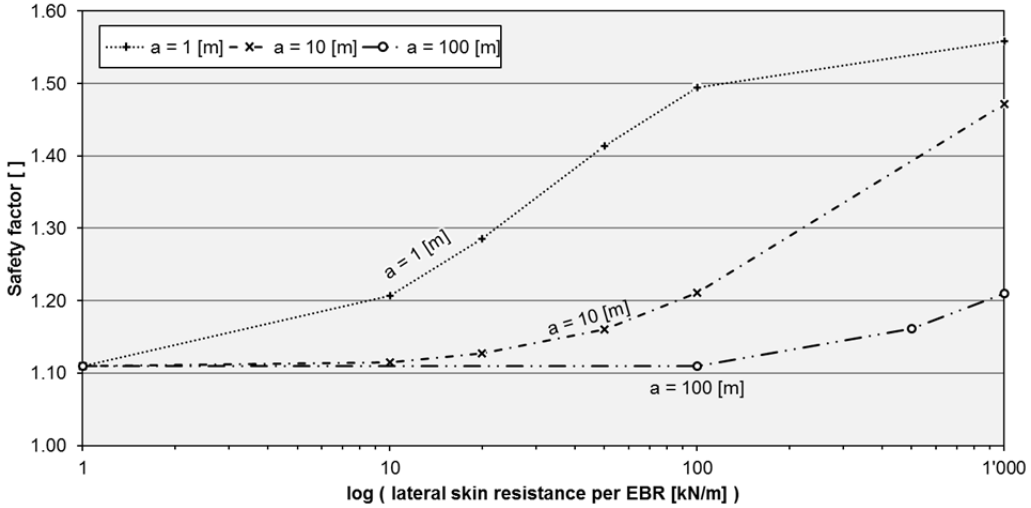

Figure 41 Overview of the variation of the spacing on a logarithmic scale (pile length of $20\ \mathrm{m}$)

Again the result from Figure 41 is rearranged and plotted as safety factor versus lateral skin resistance per meter. A similar result as before is obtained in Figure 42.

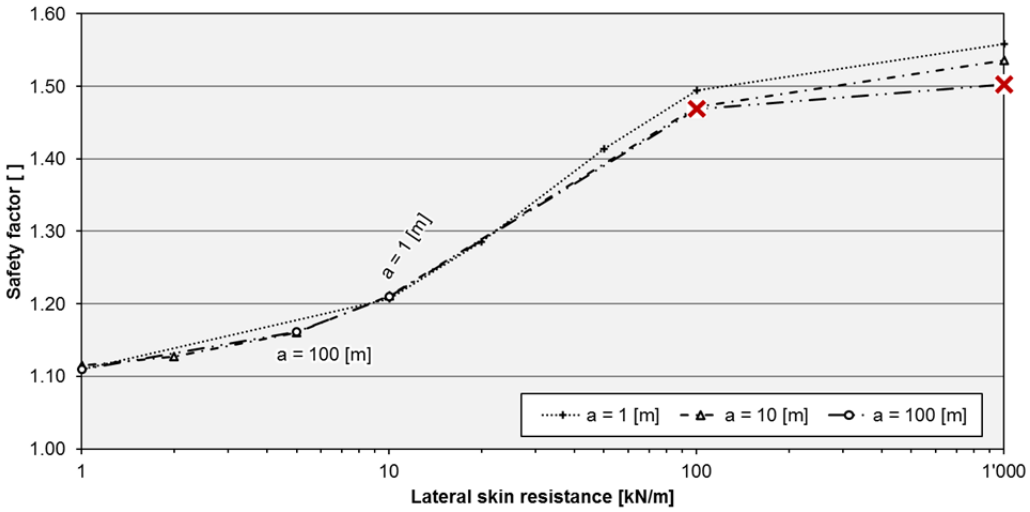

Figure 42 Safety factor vs. lateral skin resistance per meter (pile length of $20\ \mathrm{m}$)

The safety factors and the forces obtained from the analysis with an Embedded Beam Row follow a certain path. When the ratio of the spacing and the lateral skin resistance is equivalent, the same safety factor is obtained. A Large spacing with a large lateral skin resistance results in numerical instabilities.

3.3.5 Elastoplastic Embedded Beam Row

A variation of the elastoplastic parameters based on a lateral skin resistance of $\mathrm{T_{lat}} = 50\,\frac{\mathrm{kN}}{\mathrm{m}}$, an axial skin resistance of $\mathrm{T_{skin}} = 10\ \frac{\mathrm{kN}}{\mathrm{m}}$ and a spacing of $\mathrm{L_s} = 1\ \mathrm{m}$ is performed. The maximal axial force of the calculation with the elastic Embedded Beam Row is $\mathrm{N_{max}} = 17\ \mathrm{kN}$; the maximal bending moment is $\mathrm{M_{max}} = -48\ \mathrm{kNm}$. The safety factor obtained from the calculation with the elastic Embedded Beam Row is $\Sigma \mathrm{M_{sf}} = 1.172$. For the analysis with an elastoplastic Embedded Beam Row the 'Strength Reduction' in the 'Selection explorer' is activated (Figure 43).

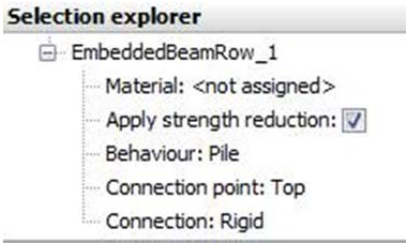

Figure 43 Application of 'Strength Reduction' to structure

The results are shown in Figure 44. Two cases with different plastic axial forces are performed. For both cases the bending moment is varied between $M_{pl} = 10$ and $70\ kNm$. The plastic axial force in the first case (Figure 44a) is below the internal maximal axial force, which means that the Embedded Beam Row is forced to form a plastic axial joint ($N_{pl} = 5\ kN < N_{max} = 17\ kN$). All the results obtained from a plastic axial force $N_{pl} = 5\ kN$ show numerical instabilities and therefore the results cannot be interpreted. The second case (Figure 44b) has an axial skin resistance above the internal force and has an axial elastic behaviour since the plastic force is not reached ($N_{pl} = 100\ kN > N_{max} = 17\ kN$). The same result as from the calculations with an elastic Embedded Beam Row is obtained when the plastic bending moment equals $M_{pl} = M_{max} \cdot \Sigma M_{sf} = 48 \cdot 1.17 = 56\ kNm$. Numerical instabilities are also observed at an axial force of $N_{pl} = 100\ kN$ when the plastic bending moment is smaller as $M_{pl} < 30\ kNm$.

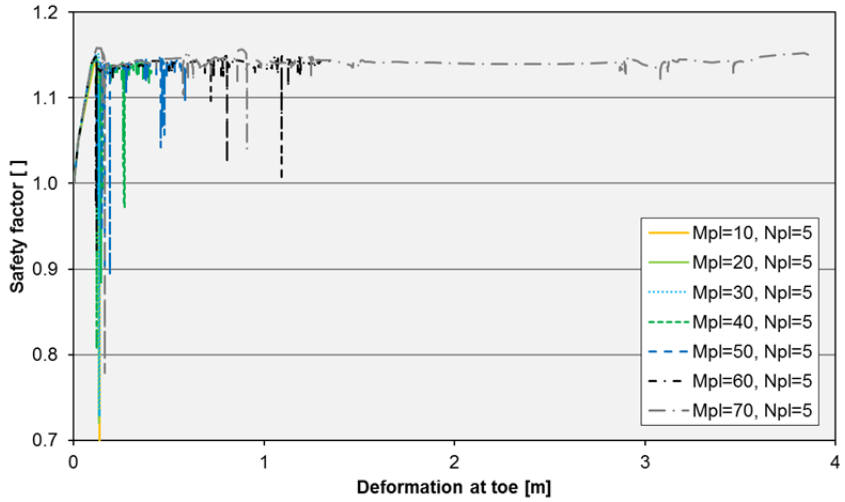

a)

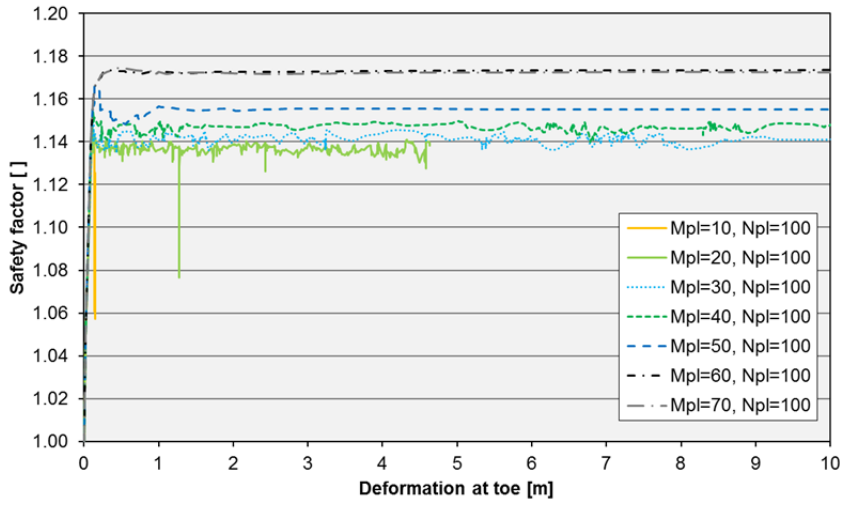

b)

Figure 44 Safety factor vs. deformation for the elastoplastic evaluation

The result of the plastic axial force of $N_{pl} = 100\,kN$ is summarised in Figure 45. The Embedded Beam Row behaves at large plastic bending moments like the elastic Embedded Beam Row from previous results as expected. These results are marked yellow with the notation 'elastic behaviour'.

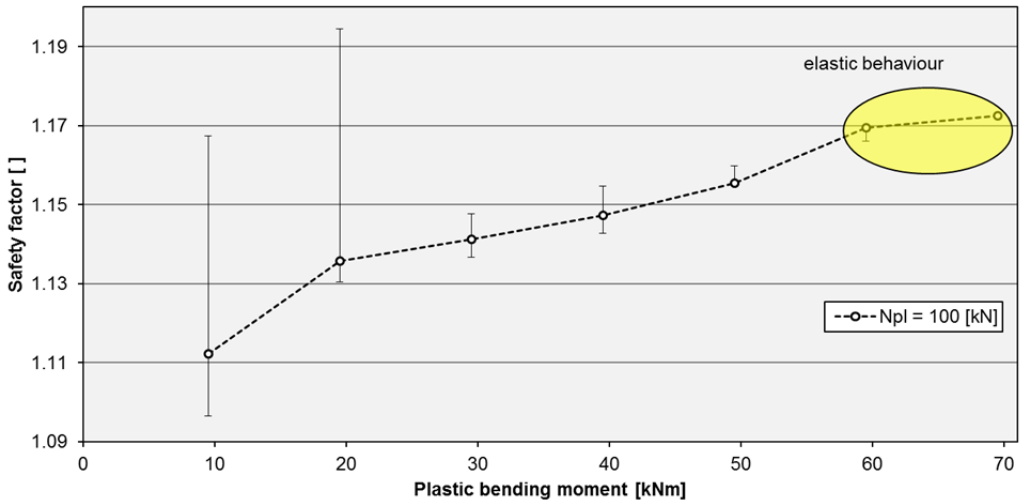

Figure 45 Safety factor vs. plastic bending moment ($N_{pl} = 100\,kN$)

In chapter §3.3.4 it is stated that internal forces are meant per meter not per Embedded Beam Row. The example with a spacing of $L_s = 1\,m$, a lateral skin resistance of $T_{lat} = 50\frac{kN}{m}$, and an axial skin resistance of $T_{skin} = 10\frac{kN}{m}$ is compared with an additional model with $L_s = 10\,m$. The lateral and axial skin resistance, as well as the plastic axial and bending yield are set relatively to each other to obtain similar internal forces. Therefore: $L_{s,A}: L_{s,B} = 1:10 = T_{skin,A}: T_{skin,B} := aso$. The described material parameters are summarised in Table 6.

Table 6 Comparison of elastoplastic behaviour at different spacing

Data set	**Spacing**	**Lateral skin resistance**	**Axial skin resistance**	**Plastic axial force**	**Plastic bending moment**
	$L_s[m]$	$T_{lat}\left[\frac{kN}{m}\right]$	$T_{skin}\left[\frac{kN}{m}\right]$	$N_{pl}[kN]$	$M_{pl}[kNm]$
A	1.0	50	10	100	30
B	10.0	500	100	1'000	300

The results in Figure 46 are hardly distinguishable. The internal forces, the safety factors and the failure mechanisms are almost identical. This means that when plastic limits correspond to the spacing, the same result is obtained. Also an analysis with Limit Equilibrium obtains the same results when the shear force and the spacing are chosen in relation to the spacing.

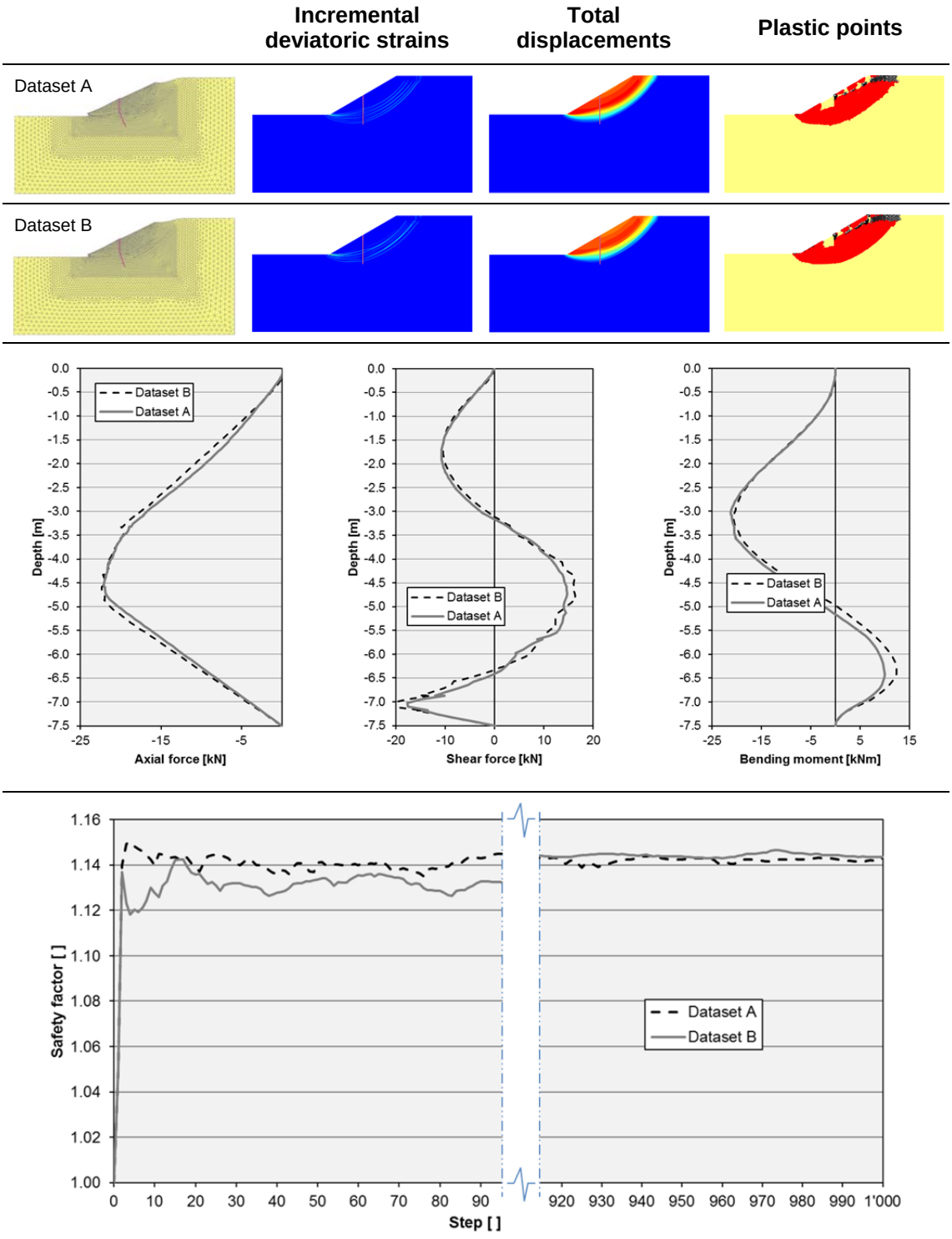

Figure 46 Failure mechanisms of dataset A and B

3.3.6 Connection point

The connection point option is described in chapter §2.3. Till now all the calculations have been performed with a rigid fixation by the assumption of a stiff bar connecting the single dowel heads. The influence of the connection adjustment is shown in Figure 47, based on the results from chapter §3.3.4 with a spacing of $L_s = 0.5$ and $20\,\mathrm{m}$. The safety factor is not affected by the choice of the connection point. In reality a stiff connection at a large spacing is hardly feasible. The rather realistic connection is free or hinged.

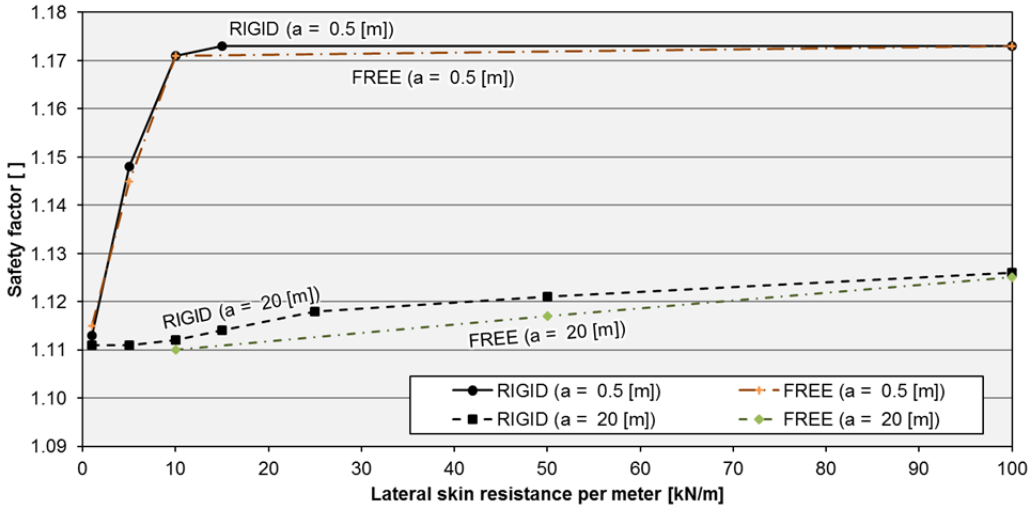

Figure 47 Safety factor depending on the connection point

3.3.7 Tension stress

In previous chapters it is mentioned that the dowel with a vertical orientation is mostly shear stressed, while the base and axial skin resistance have almost no influence. A $18.34\,\mathrm{m}$ long horizontally orientated pile comes to a safety factor of $\Sigma M_{sf} = 1.276$ (axial and lateral skin resistance $T_{skin} = T_{lat} = 10\,\frac{kN}{m}$, base resistance $F_{max} = 0.01\,kN$). Increasing the lateral skin resistance to a value of $T_{lat} = 100\,\frac{kN}{m}$ causes a minor change ($\Sigma M_{sf} = 1.292$), whereas the increment of the axial skin resistance ($T_{skin} = 100\,\frac{kN}{m}$) results in $\Sigma M_{sf} = 1.338$. The failure mechanism is pushed behind the dowel. The increment of the base resistance ($F_{max} = 1'000\,kN$) has the least impact ($\Sigma M_{sf} = 1.282$). The horizontally orientated pile behaves as expected; the calculation is mostly influenced by the axial skin resistance. The result is shown in Figure 48.

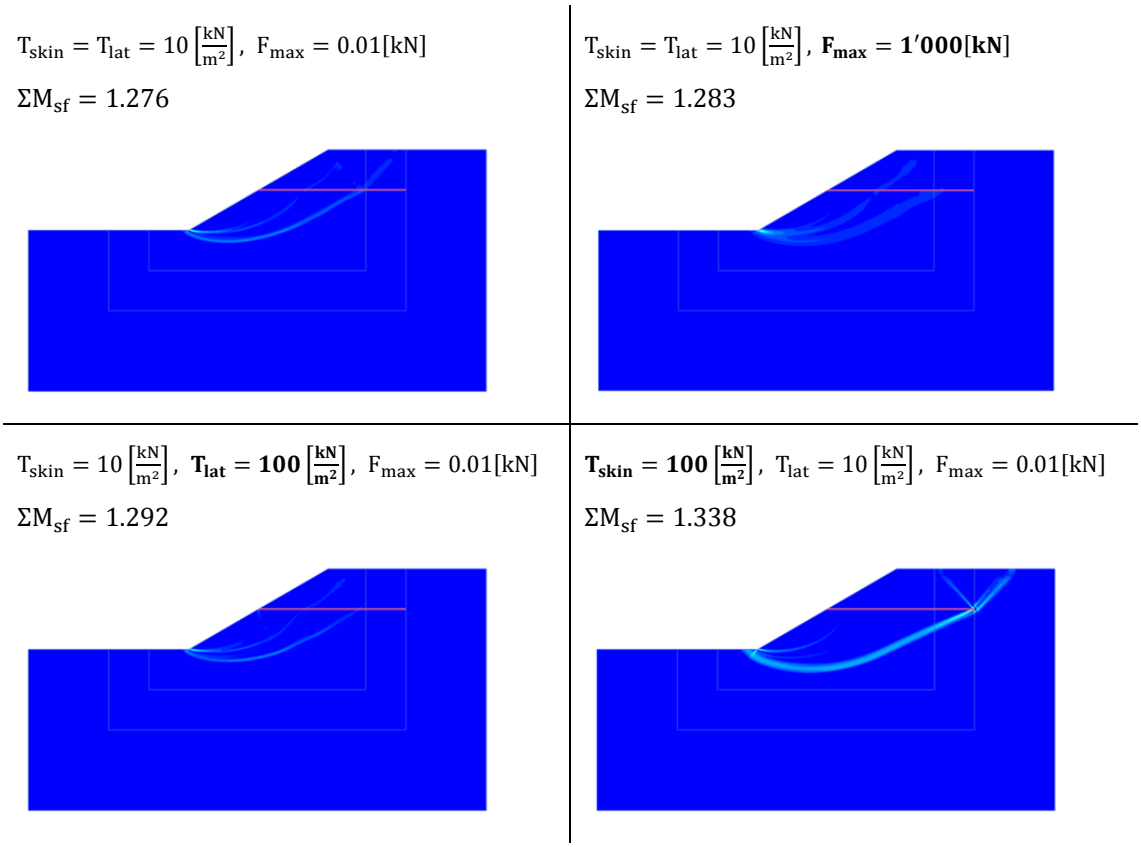

Figure 48 Incremental deviatoric strains of the horizontal dowel

Note: when orientating an Embedded Beam Row horizontally, the location of the connection point should be checked or the behaviour should be changed to rock bolt. An Embedded Beam Row with pile behaviour automatically sets the point with larger vertical coordinate as connection point. The connection point also affects the location, where the base resistance is applied.

3.4 Slope stability analysis in PLAXIS 3D

The soil parameters for the 3-dimensional model conform to Table 1. The model size is shown in Figure 9. The width of the model equals principally twice the spacing of the piles and two piles are located in the model. Figure 49 shows the plan view of the model with a spacing of $L_s = 0.5\,\mathrm{m}$. The coarseness factors are modified though (Coarseness factor inner area: 0.6, intermediate area: 0.8, outer area: 1.0).

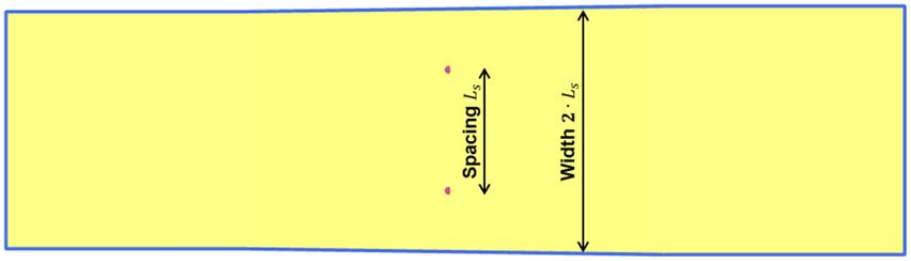

Figure 49 Model size of the three-dimensional models (plan view)

3.4.1 Mesh quality of the unsupported model (3D)

For the two dimensional calculations 15-noded elements are selected. The three dimensional calculations in PLAXIS 3D only allow 10-noded elements, which conform to 6-noded elements in two dimensions. Therefore the elements in 3D need to be chosen relatively smaller as the elements in 2D to obtain comparable results. The mesh quality is investigated for the three dimensional calculations as well. Four different meshes are generated; the result is shown in Table 7 and in Figure 50.

Table 7 Result of the mesh variation (3D)

Mesh	**Mesh factor**	**No. of soil elements**	**Minimal elem. volume**	**Average elem. size**	**Safety factor**
	[ ]	[ ]	$[\mathrm{m}^3]$	$[\mathrm{m}]$	$\sum M_{SF}$ [ ]
	0.01	72751	2.95E-03	0.1533	1.118
v. fine	0.02	8885	0.016	0.4387	1.118
fine	0.03	4366	0.06818	0.6258	1.137
	0.04	3681	0.1003	0.6816	1.149

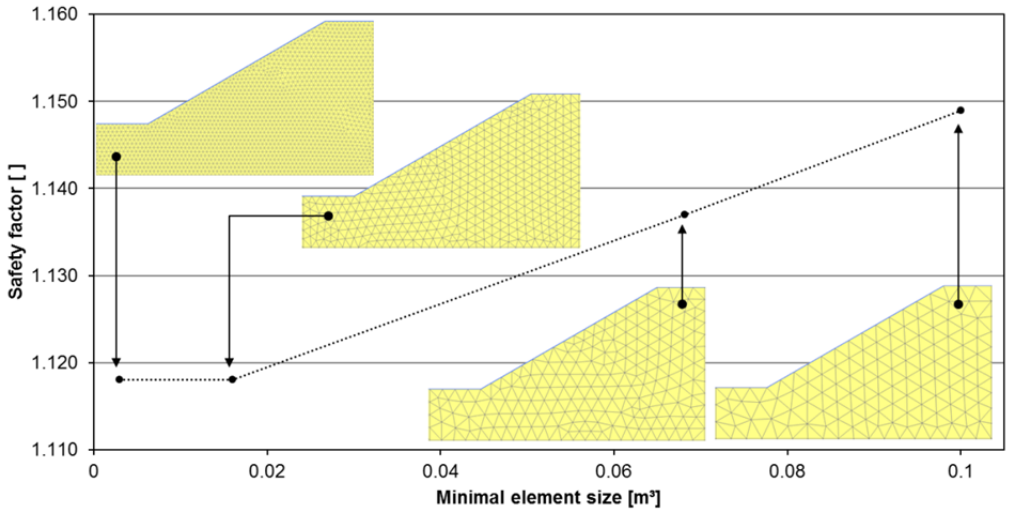

Figure 50 Safety factor vs. minimal element size (3D)

A mesh factor of 0.02 (minimal element size: $0.016\ \mathrm{m}^3$) results in the same safety factor as the finest mesh. The safety factor of the unsupported slope in 3D is $\Sigma M_{sf} = 1.118$. Figure 51 compares the result from 2D (§3.1.2, Figure 12) with the result from 3D. The incremental deviatoric strains and the failure mechanism correlate well. Due to the spacing every model has a different size, thus the mesh factor is only a reference value. The safety factor is the benchmark which should be achieved; hence in every 3D model the safety factor of the unsupported slope is calculated as well.

PLAXIS 2D and SLIDE (GLE) PLAXIS 3D (mesh factor 0.02)

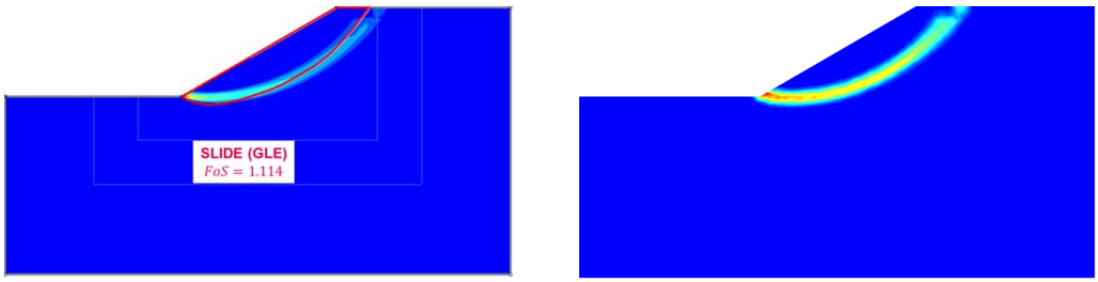

Figure 51 Comparison failure mechanisms of the unsupported slope (2D vs. 3D)

3.4.2 Embedded Beam

The Embedded Beam in PLAXIS 3D has fewer input parameters as the Embedded Beam Row in PLAXIS 2D. The parameters are shown in Table 8. The Embedded Beam does not allow elastoplastic calculations in the current version. The moment of inertia is the same in both directions. The lateral skin resistance is no input parameter in 3D. The model consists of two Embedded Beams and the width of the model equals two times the spacing of the associated model in 2D.

Table 8 Embedded Beam parameters

Parameter	**Name**	**Embedded Beam**	**Unit**
Behaviour option	-	Pile	-
Connection point	-	Top	-
Connection	-	Rigid	-
Young's Modulus	E	2.0E8	$\left[\frac{\mathrm{kN}}{\mathrm{m}^2}\right]$
Specific weight	γ	60	$\left[\frac{\mathrm{kN}}{\mathrm{m}^3}\right]$
Pile type	-	User-defined	-
Profile area	A	0.01	$[\mathrm{m}^2]$
Moment of inertia	I_3	2.0E-4	$[\mathrm{m}^4]$
Moment of inertia	I_2	2.0E-4	$[\mathrm{m}^4]$
Axial skin resistance	$\mathrm{T}_{\mathrm{skin}}$	10	$\left[\frac{\mathrm{kN}}{\mathrm{m}}\right]$
Base resistance	$\mathrm{F}_{\mathrm{max}}$	$0.01 \approx 0$	$[\mathrm{kN}]$
*specific weight is the difference between weight of the Embedded Beam and the soil			

The influence of the axial skin resistance is investigated in Appendix D. Several three dimensional calculations with Embedded Beams are performed. The spacing is varied and compared with the results obtained from the evaluation of the spacing in chapter §3.3.4. For every model an unsupported calculation is performed to check if the mesh is fine enough. Afterwards the safety factors of the unsupported slope are compared. Appendix D shows that the axial skin resistance has no influence on the safety factor obtained from safety analysis; hence the axial skin resistance is set to $\mathrm{T}_{\mathrm{skin}} = 1'000\,\frac{\mathrm{kN}}{\mathrm{m}}$. Figure 52 shows the steps versus the safety factor. Some calculations are not numerically stable.

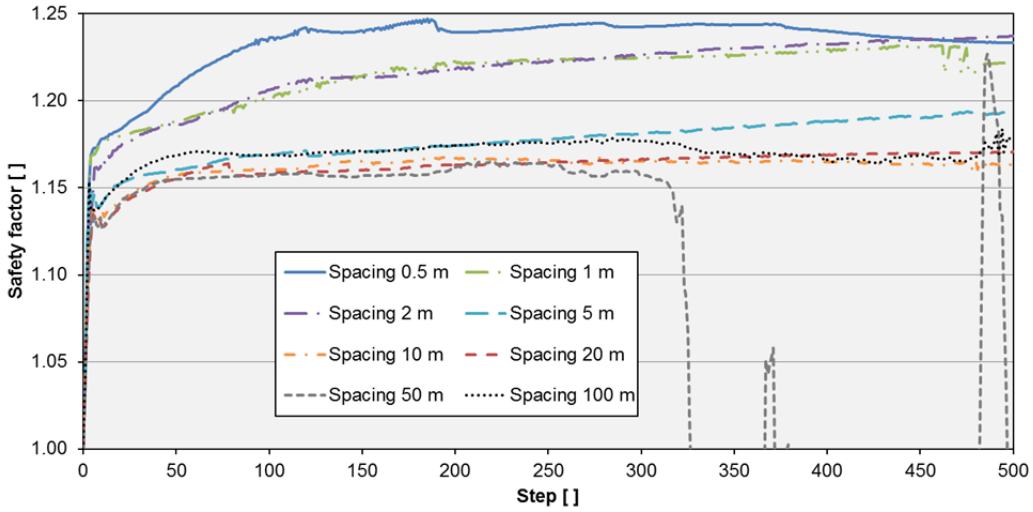

Figure 52 Safety factor vs. step (Embedded Beam)

Figure 53 shows the result from the evaluation. The black line indicates the safety factor obtained from the supported slope at the 200th step. The red line indicates the safety factor of the unsupported slope (with disabled Embedded Beams). Different meshes are generated in the models, the safety factors of the unsupported slope allow to compare the results at different element sizes.

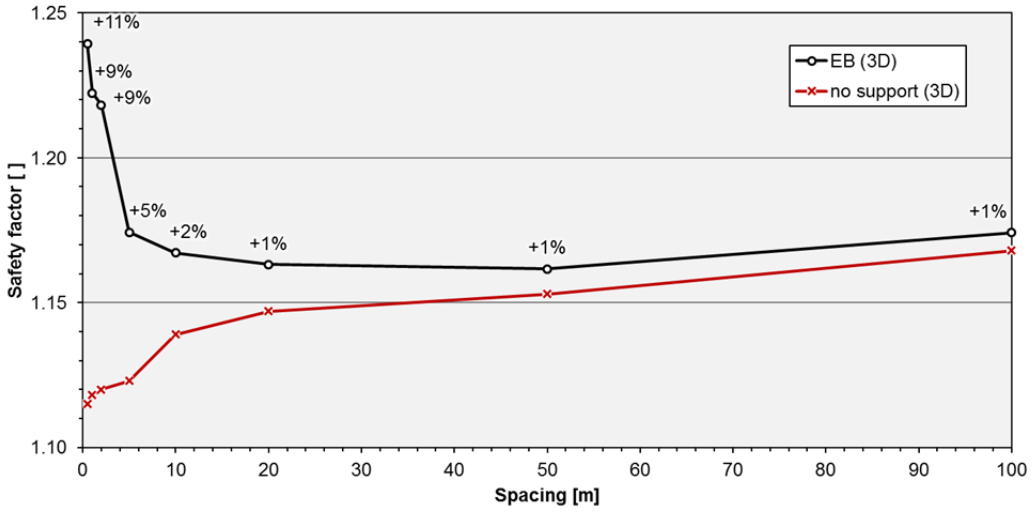

Figure 53 Safety factor vs. spacing (Embedded Beam)

The result from Figure 53 is illustrated in Figure 54 as a bar graph. It shows once more the improvement of the slope stability depending on the spacing of the Embedded Beam. The evaluation of the failure mechanisms will be compared in chapter §3.5 to the results from 2D.

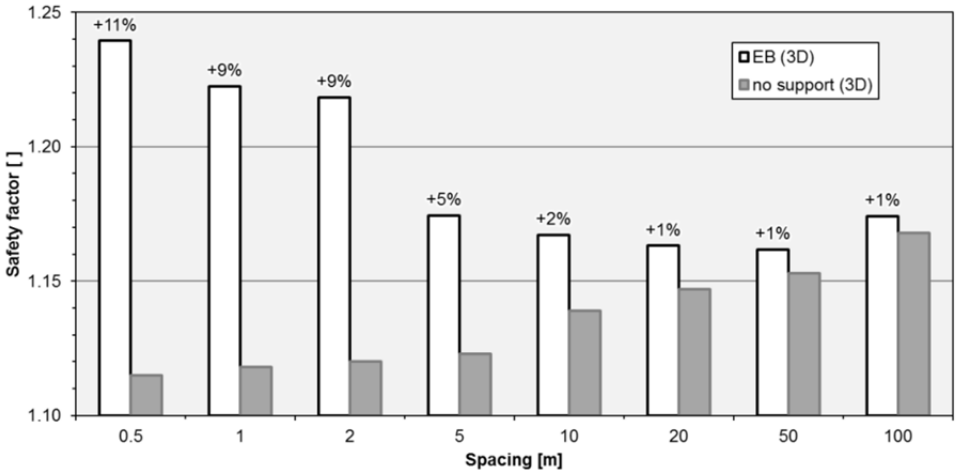

Figure 54 Safety factor vs. spacing as bar graph (Embedded Beam)

The results are normalised to allow a better comparison with the results obtained from the 2D calculations. Hereby the improvement of the safety factor in percent is added to the minimal safety factor of the unsupported slope ($\Sigma M_{sf} = 1.115$). The result is shown in Figure 55.

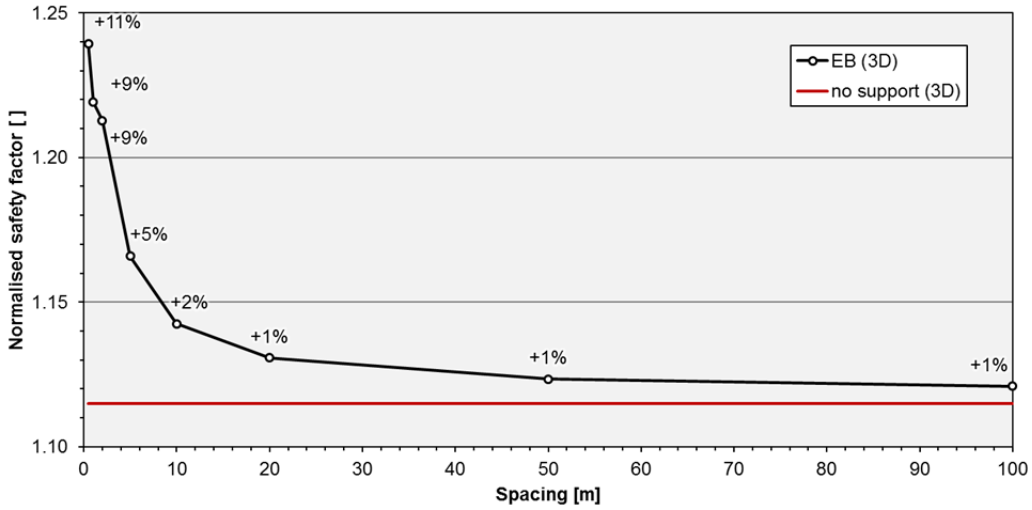

Figure 55 Normalised safety factor (Embedded Beam)

3.4.3 Volume element

The slope stability is investigated also by modelling volume elements with interfaces. Grabe (2016) has shown that the impact of elasto-plasticity for his numerical model is small. The parameters used in this model are based on Grabe (2016) and are described in Table 9. A square cross section ($0.51\text{x}0.51\ \text{m}^2$) is assumed for simplicity reasons. The volume element is surrounded by interface elements to model the soil-pile interaction.

Table 9 Parameters for pile modelled by volume elements

Parameter	Name	Pile	Unit
Material Model	-	Linear elastic	-
Unsaturated specific weight	γ_{unsat}	21.47	$\left[\frac{kN}{m^3}\right]$
Saturated specific weight	γ_{sat}	21.47	$\left[\frac{kN}{m^3}\right]$
Young's modulus	E'	12'000'000	$\left[\frac{kN}{m^2}\right]$
Poisson's ratio	ν'	0	[ ]

The result of the evaluation is shown in Figure 56. Other than the Embedded Beam the usage of volume elements does not lead to numerical instabilities and a clear safety factor is obtained within 100 steps.

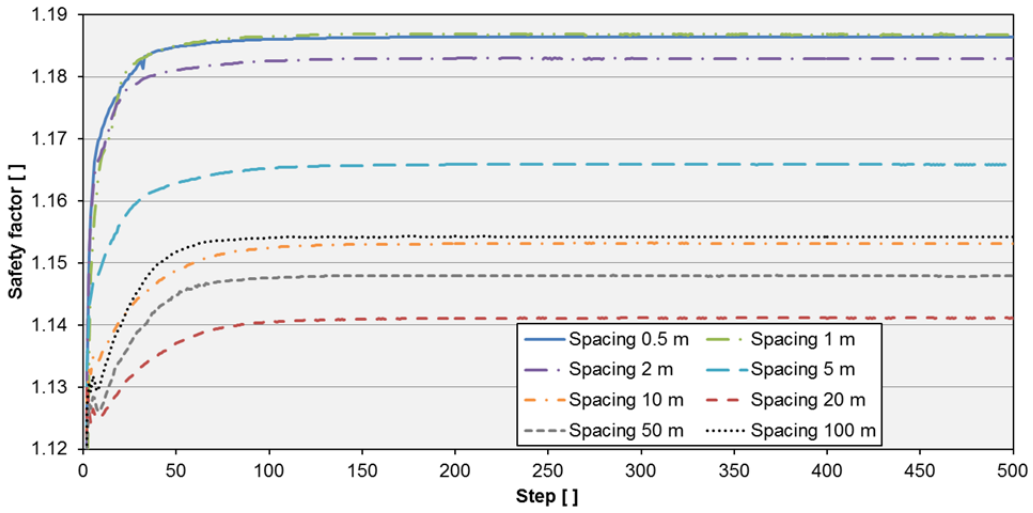

Figure 56 Safety factor vs. step (volume elements)

Figure 57 summarizes the result of the evaluation. Again the black line indicates the safety factor obtained from the supported slope and the red line indicates the unsupported safety factor. Already at a spacing of $L_s \geq 20\ m$ the slope stability does not improve. Figure 58 shows the same result in bars. The evaluation of the failure mechanisms will be compared in chapter §3.5 with the results from 2D. Again the results are normalised in Figure 59 to compare with the results from 2D. The improvement of the safety factor in percent is added to the minimal safety factor of the unsupported slope ($\Sigma M_{sf} = 1.115$).

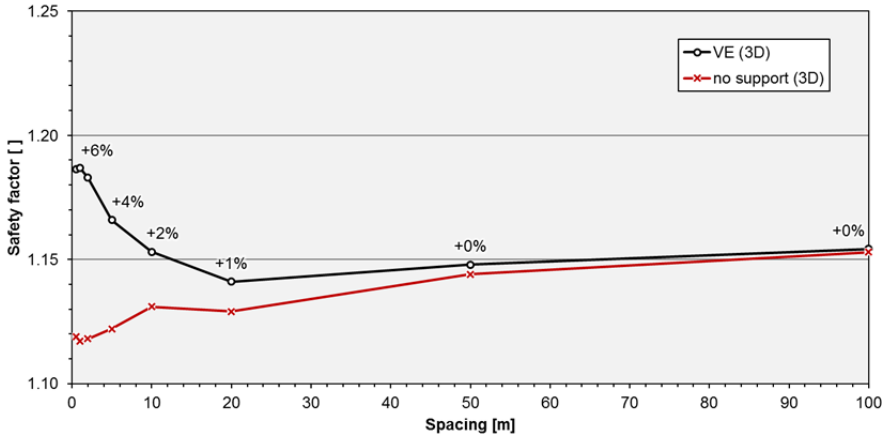

Figure 57 Safety factor vs. spacing (volume elements)

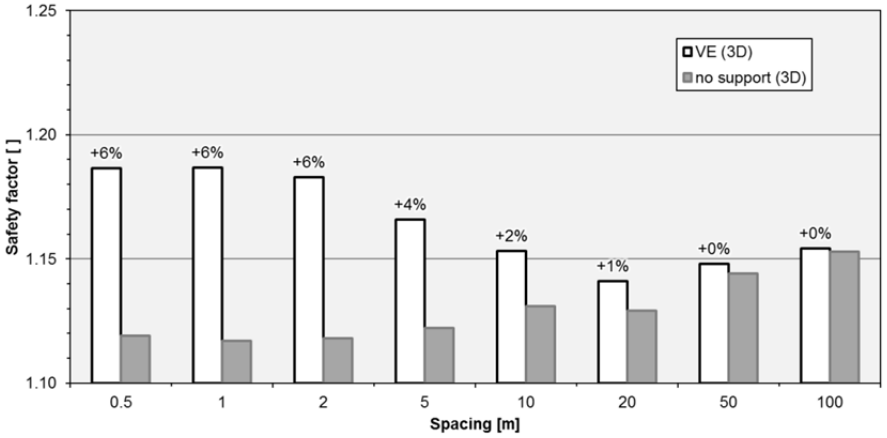

Figure 58 Safety factor vs. spacing as bar graph (volume elements)

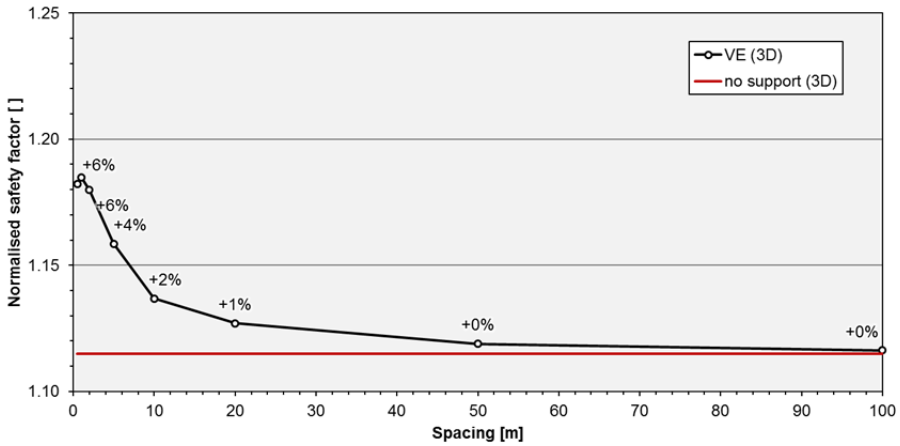

Figure 59 Normalised safety factor (volume elements)

3.5 Comparison of the results

In this chapter all the results for different methods are compared. Figure 60 summarizes the safety factor depending on the spacing and the method for the supported slope. The black line indicates the result obtained from the Embedded Beam Row at a lateral skin resistance of $T_{skin} = 100\ kN$. This lateral skin resistance is chosen since it fits best with the 3D results. The safety factor obtained by the 3-dimensional analysis cannot be matched without an arbitrary assumption for the lateral skin resistance. The green lines indicate the results obtained from the evaluation with linear elastic piles in PLAXIS 3D. The form of the lines for the Embedded Beam and volume elements with interfaces is similar. Both have a plateau at a spacing of $L_s \leq 2\ m$, where the result is the same, since the piles are so close to each other and act like a wall. At small spacing's the safety factor of the volume elements is smaller than the one with Embedded Beams. The safety factors obtained from the Embedded Beam Row (2D) are generally smaller. The maximal safety factor obtained for the Embedded Beam Row is $\Sigma M_{sf} = 1.175$ which is smaller than the result from PLAXIS 3D.

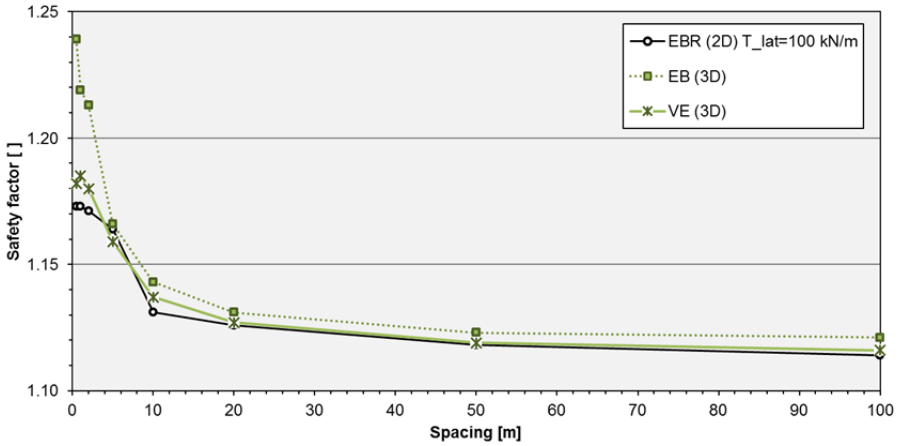

Figure 60 Comparison of safety factors by different methods

Figure 61 and Figure 62 show the failure mechanisms obtained from 2D and 3D. Figure 61 is a cross section through the pile, where Figure 62 is a cross section in the middle of the piles. The results displayed for 2D are the same in both figures. First the focus is set on the 3D results. The figures show that the failure in the section of the pile in 3D is similar (Figure 61). At the spacing of $L_s \leq 2\ m$ the failure between (Figure 61) the piles and through (Figure 62) the piles are the same, since they act like a wall. In certain cases the failure mechanisms of the Embedded Beam and volume elements correspond well.

Now the results from 2D and 3D are compared. Both, 2D and 3D results have similar failure mechanisms in certain cases. The failure of the Embedded Beam Row rather represents the failure between the piles (Figure 62).

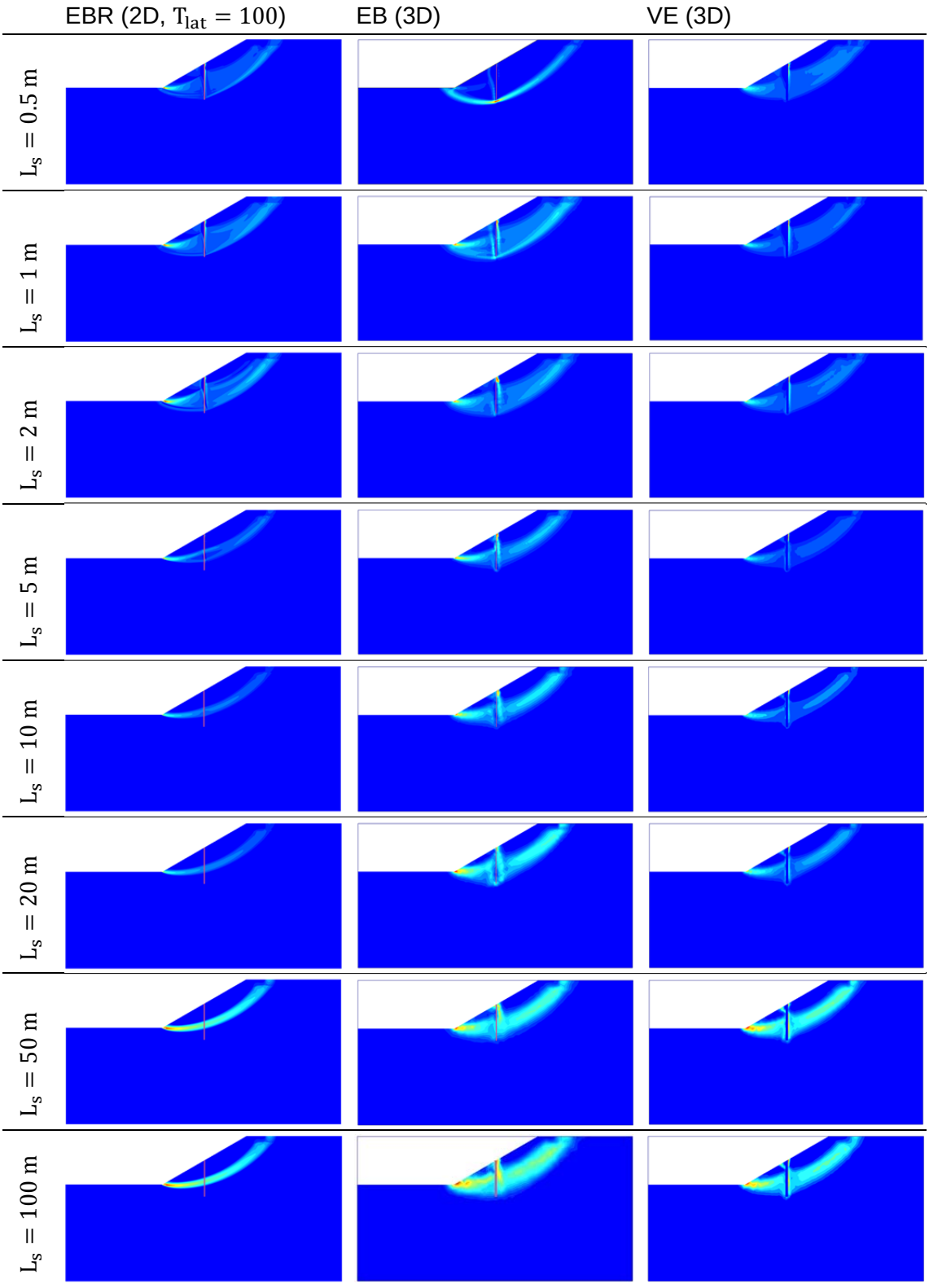

Figure 61 Comparison of the failure at the dowel (Incremental deviatoric strains)

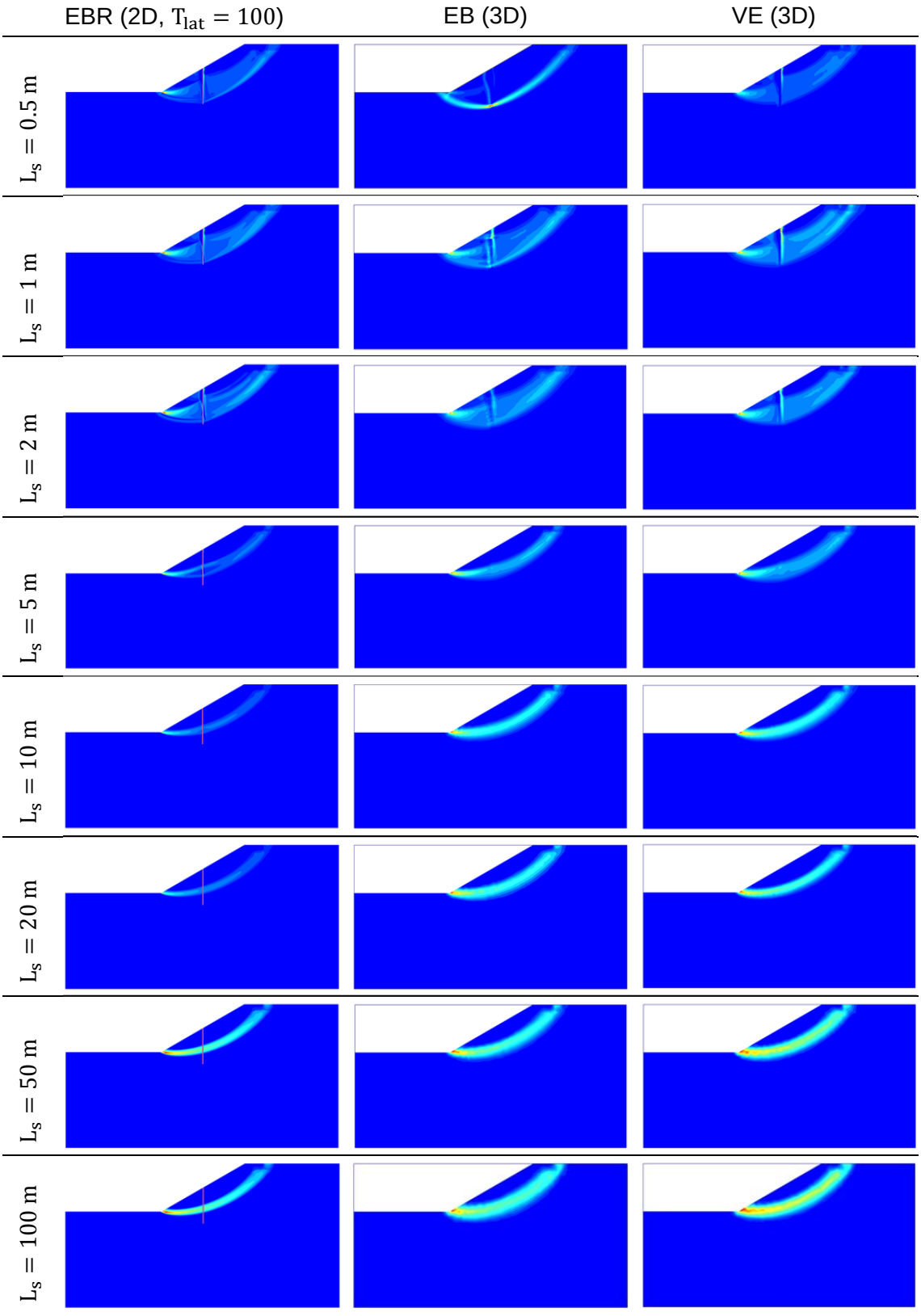

Figure 62 Comparison of the failure between the dowels (Incremental deviatoric strains)

3.6 Conclusion

The upper limit of the Embedded Beam Row corresponds to a plate element. The lower limit equals the unsupported slope. It is also possible to generate results in between by varying the lateral skin resistance. The axial skin and the base resistance have almost no influence since the dowel is sheared and laterally loaded. The influence of the connection point is negligible.

The '2.5D' behaviour of the Embedded Beam Row is not satisfying. The result obtained follows a pattern lead by the interface stiffness factor, the spacing and the skin resistance. In other words, when the spacing and the skin resistance are related to the pile spacing, the same result is obtained. The variation of the spacing at unlimited lateral shear strength is not leading to a realistic result. A calibration is necessary. By comparing results with 3D analysis the results are fitted to an acceptable, but not satisfying result at a lateral skin resistance of $\mathrm{T}_{\mathrm{lat}} = 100\,\frac{\mathrm{kN}}{\mathrm{m}}$.

4 Slope with weak layer

Based on the model from chapter §3 a model with a weak layer is generated. The procedure is similar to the investigations of the homogeneous slope. After studying the unsupported slope in chapter §4.1, the failure of the plate supported slope is investigated (chapter §4.2). Afterwards the assumptions about Embedded Beam Rows done in previous chapters are tried to be confirmed. Some comparative three dimensional calculations are performed. Finally a conclusion closes this chapter.

4.1 Unsupported slope

The model with a weak layer is basically the same as in the previous chapters. The model size is expanded on the right side. No water loads are applied again. A weak layer with a thickness of one meter is added. The layer is based on the failure line from SLIDE in Appendix C, which is offset by $0.5\ \mathrm{m}$ in both directions (coordinates in Table 18). The model is shown in Figure 63. Note that the soil parameters are adapted (Table 10), apart from for the unit weight all the parameters are changed. The amount of steps is reduced to 500 steps because this has been shown to be sufficient to obtain a clear failure mechanism. For calculations, where the safety factor still changes after 500 steps, the amount of steps is increased.

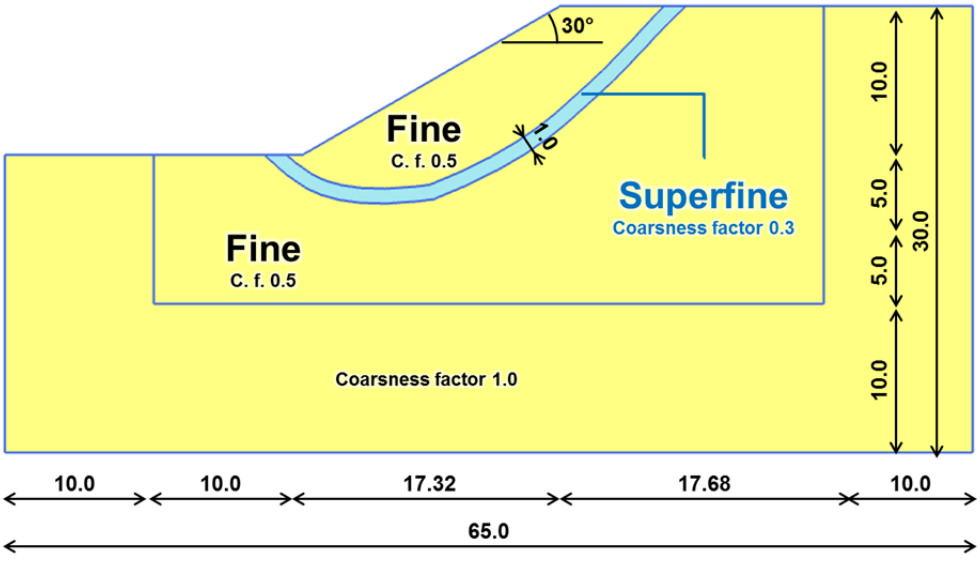

Figure 63 Soil profile with weak layer

Table 10 Soil properties of the homogeneous soil model

Parameter	Name	Soil body	Weak layer	Unit
Material model	-	Mohr-Coulomb	Mohr-Coulomb	-
Unsaturated specific weight	γ_{unsat}	16	16	$\left[\frac{kN}{m^3}\right]$
Saturated specific weight	γ_{sat}	16	16	$\left[\frac{kN}{m^3}\right]$
Young's modulus	E'	15'000	5'000	$\left[\frac{kN}{m^2}\right]$
Poisson's ratio	ν'	0.3	0.3.	[ ]
Cohesion	c'_{ref}	10.0	0.01	$\left[\frac{kN}{m^2}\right]$
Friction angle	φ'	25	20	[°]
Dilatancy angle	ψ	0	0	[°]

4.1.1 Influence of the mesh

As already mentioned several times the mesh size influences the result. The mesh factor is varied between 0.01 and 0.05. The result is shown in Table 11 and Figure 64. The selected mesh factor is 0.03. Figure 65 shows the failure through the weak zone (mesh factor 0.03).

Table 11 Result of the mesh variation for slope with weak layer

Mesh	Mesh factor	No. of soil elements	Minimal elem. area	Average elem. size	Safety factor
	[ ]	[ ]	$[m^2]$	$[m]$	$\sum M_{SF}$[ ]
	0.01	26169	< 0.01	0.273	1.037
	0.02	6506	0.02	0.5475	1.045
v. fine	0.03	2832	0.05	0.8298	1.045
fine	0.04	1636	0.08	1.092	1.063
	0.05	1111	0.07	1.325	1.061

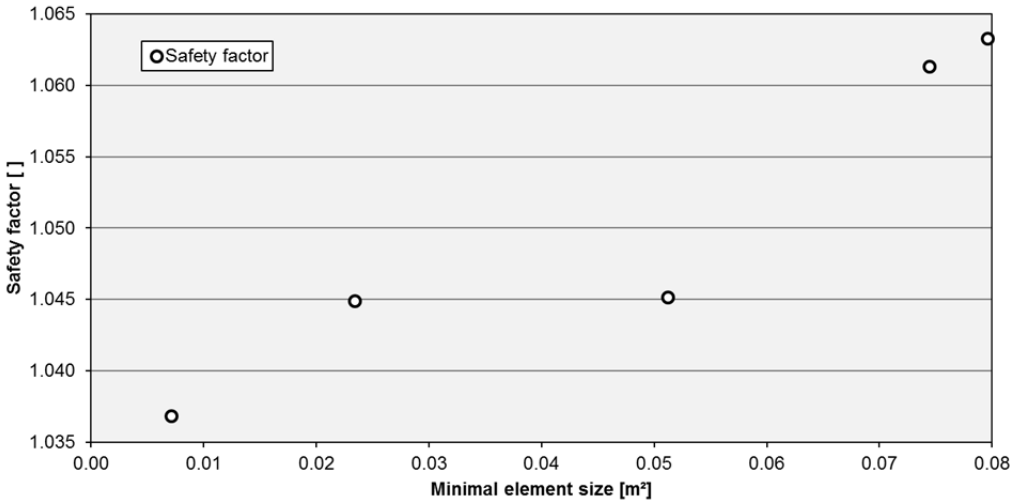

Figure 64 Safety factor vs. minimal element size for slope with weak layer

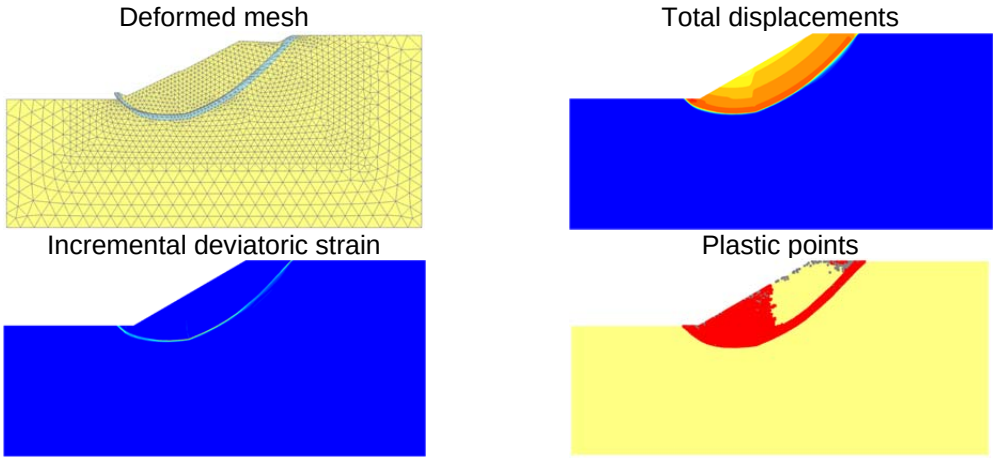

Figure 65 Visualisation of the failure mechanism for the slope with a weak layer (chosen mesh factor: 0.03)

4.1.2 Comparative calculations with limit equilibrium analysis

The results from calculations with Limit Equilibrium (SLIDE) are shown in Table 12. With the chosen strength parameters the failure mechanism is forced to go through the weak layer.

Table 12 Safety factors for different calculation methods for the non-homogeneous slope

Calculation method	**Non-circular failure line ΣM_{sf}**
PLAXIS: Phi/c reduction, non-associated ($\psi = 0$)	1.045
SLIDE: GLE/Morgenstern-Price	1.039
SLIDE: Spencer	1.043

4.2 Slope supported by plate

Also for the non-homogeneous soil body a brief investigation with a plate element is performed. The investigation is done by a plate element with interfaces and a plate without interfaces as well. The safety factor obtained for both is $\Sigma M_{sf} = 1.725$. The internal forces and the failure are shown in Figure 66. The length of the pile is $15\ \mathrm{m}$. Because the plate is modelled as elastic material a different failure mechanism as compared to the unsupported case is developed (failure in the weak layer is prevented by the plate).

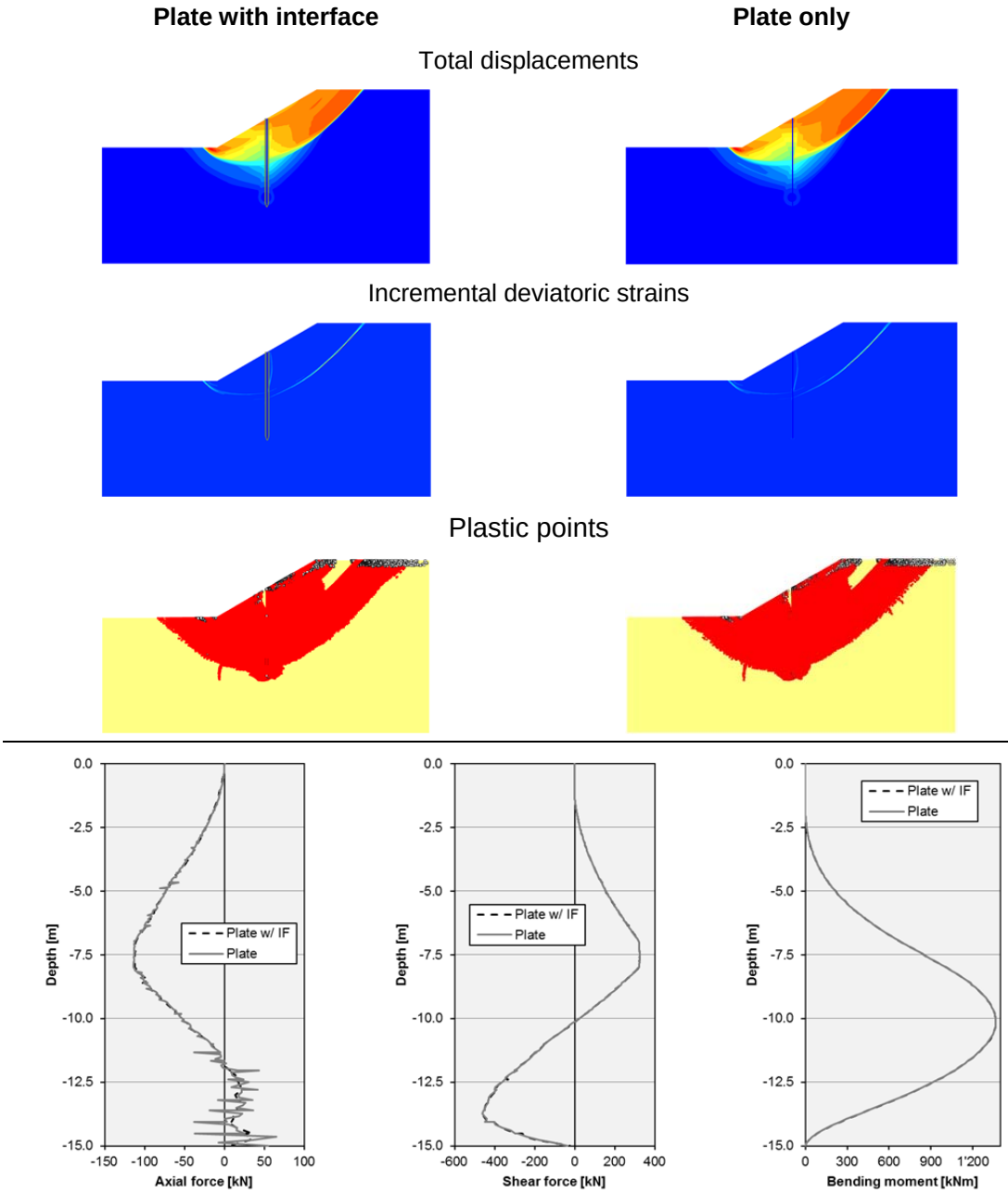

Figure 66 Internal forces and failure of the non-homogeneous slope supported by plates

4.3 Slope supported by Embedded Beam Row

The parameters for the Embedded Beam Row can be obtained by the previous example from Table 5. Other than the previous calculations the connection point on the top is set to ‘Free’, since chapter §3.3.6 has shown that the results are almost identical.

4.3.1 Length

The influence of the length of the Embedded Beam Row on the slope with a weak layer is investigated. The base, the lateral and axial skin resistance are set infinitely high ($T_{lat} = T_{skin} = F_{max} = 10^6$). The spacing is $L_s = 1\,\mathrm{m}$. The safety factors obtained are shown in Figure 67. Since the failure mechanism of the unsupported slope is at a depth of $7.5\,\mathrm{m}$, a pile length smaller than $10\,\mathrm{m}$ is ineffective and would not improve the slope stability. The maximum safety factor of the slope is limited by the failure in front of the Embedded Beam Row at a length of ca. $20\,\mathrm{m}$, which is shown in Figure 68. For further calculations the length is $15\,\mathrm{m}$ ($\Sigma M_{sf} = 1.756$). The safety factor Embedded Beam Row with a length of $15\,\mathrm{m}$ corresponds well with the result obtained by the plate in chapter §4.2. However it has to be mentioned that the failure mechanisms in the slope (outside the weakness zone) are different for this safety factors.

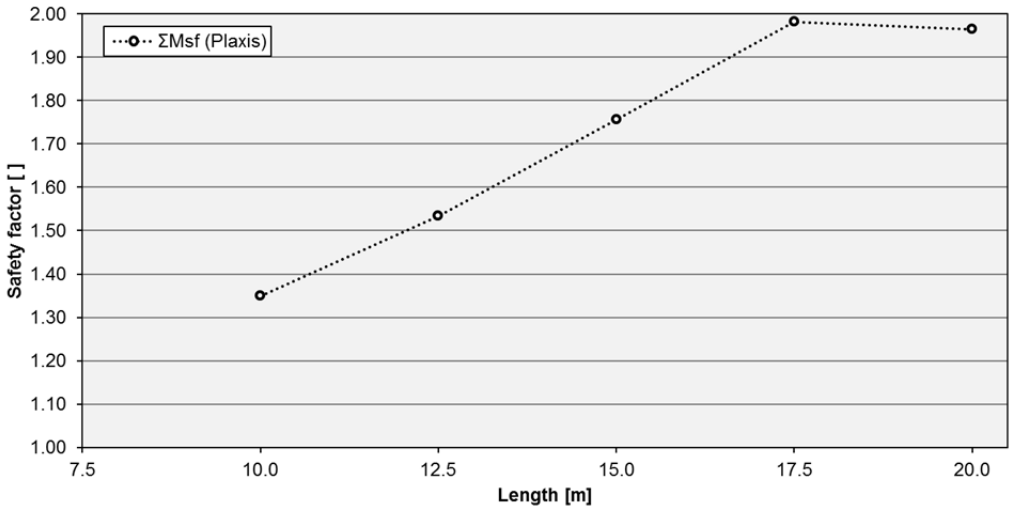

Figure 67 Variation of the dowel length for the non-homogeneous slope

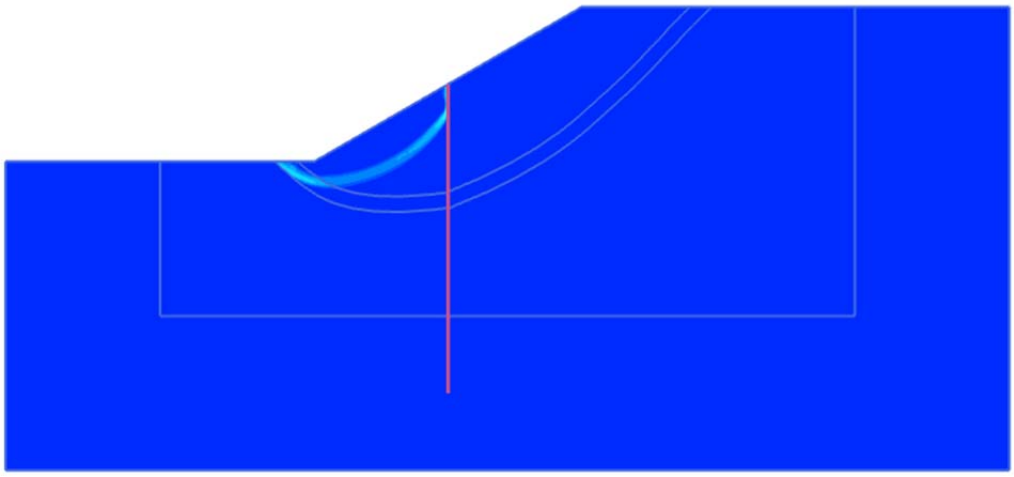

Figure 68 Failure in front of the Embedded Beam Row for pile with a length of $20\ \mathrm{m}$

4.3.2 Axial and lateral skin resistance

The result of the skin resistance variation is shown in Figure 69 on a logarithmic scale. The graphs show that also in this example the axial skin resistance has almost no impact. The lower boundary of the safety factor is the same as obtained by the unsupported slope; the upper boundary correlates with the result from the plate.

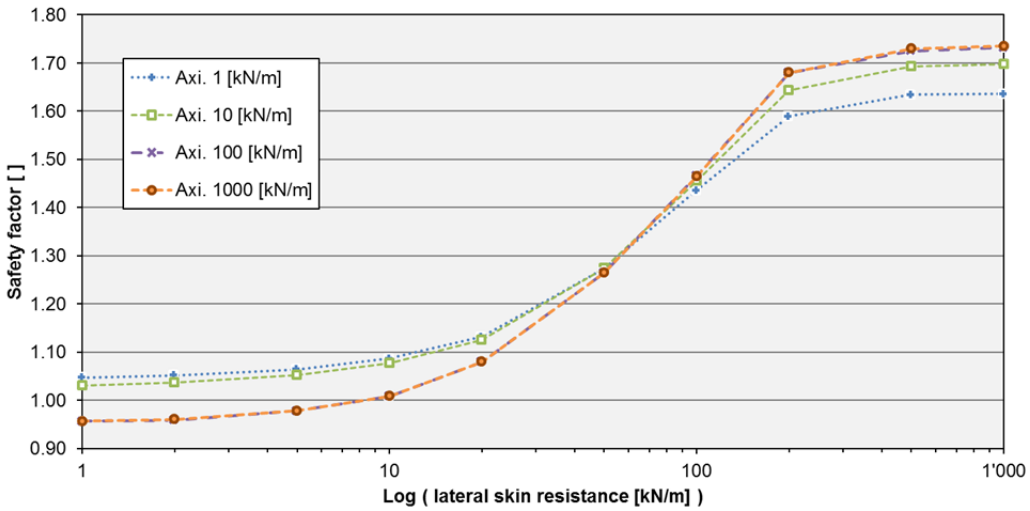

Figure 69 Overview of the variation of the lateral skin resistance on a logarithmic scale

The failure at an axial skin resistance of $T_{skin} = 1 \frac{kN}{m}$ and a lateral skin resistance of $T_{lat} > 50 \frac{kN}{m}$ has not fully developed after 500 steps; the number of steps is increased to 1'000. Considering the output of the result, the Embedded Beam Rows all bend in these examples. In previous results concerning the homogeneous slope the elastic Embedded Beam Row only rotated but no clear bending was observed.

A plastic hinge forms when elastoplastic material for the Embedded Beam Row is considered. Analysing the total displacement of all examples with an axial skin resistance of $T_{skin} = 1 \frac{kN}{m}$, it shows that after 500 steps the deformation is still relatively small. This is the reason why bending of the Embedded Beam Row was not observed yet. An example of the bending of the Embedded Beam Row is shown in Figure 70.

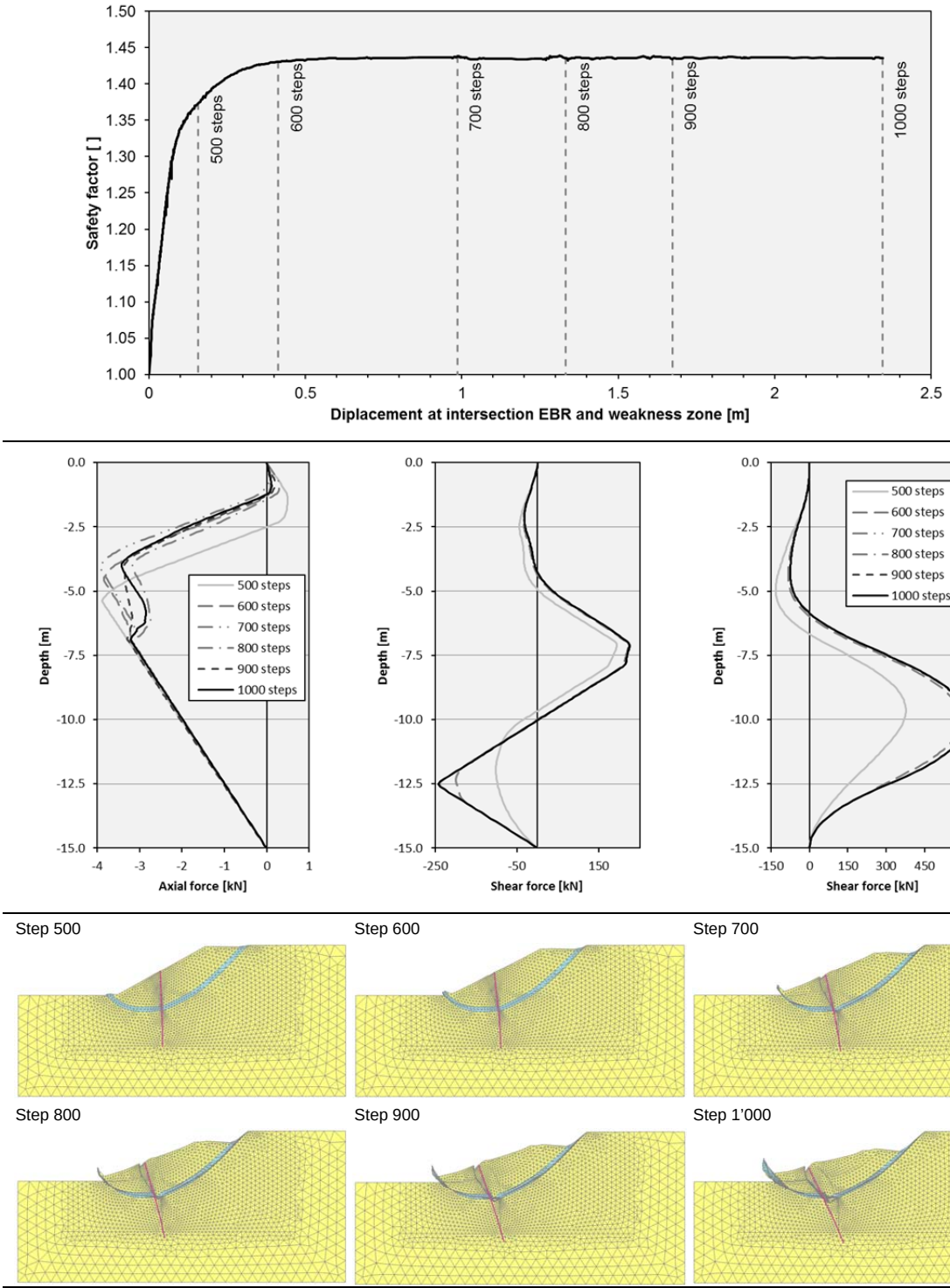

Figure 70 Bending of Embedded Beam Row via true scale deformed mesh ($T_{skin} = 1$ kN, $T_{lat} = 100$ kN)

The internal forces of the Embedded Beam Row with a varying lateral skin resistance and a constant axial skin resistance ($T_{skin} = 10\ \frac{kN}{m} = const.$) are shown in Figure 71. Again the axial force is limited by the axial skin resistance. The shear force is limited by the lateral skin resistance. The depth of the maximal shear and axial force are at the depth of the failure. The shear force and the bending moment obtained in Figure 70 are the same as the one with a lateral skin resistance of $T_{lat} = 100\ kN$.

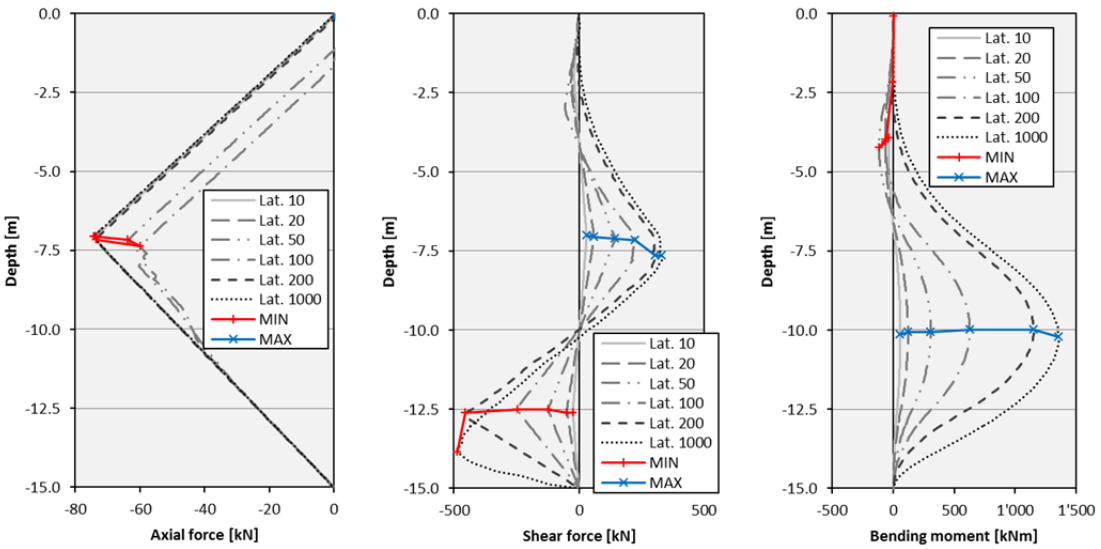

Figure 71 Internal forces of the Embedded Beam Row under variation of the lateral skin resistance ($T_{skin} = 10\frac{kN}{m} = const.$)

The behaviour of the Embedded Beam Row again corresponds with the plate in chapter §4.2 and the unsupported slope. The internal forces correspond as well. As observed before the axial skin resistance has almost no influence.

4.3.3 Base resistance

The influence of the base resistance is investigated at an axial skin resistance of $T_{skin} = 10\frac{kN}{m}$ and a lateral skin resistance of $T_{lat} = 50\frac{kN}{m}$. The safety factor obtained ($\Sigma M_{sf} = 1.275$) is constant by varying the base resistance ($F_{max} = 1; 10; 100; 1'000\ kN$). Only the axial forces differ as already noted in the investigation on the base resistance of the homogeneous slope (see chapter §3.3.2).

4.3.4 Spacing

The analysis of the spacing for the non-homogeneous slope is slightly different as the one for the homogeneous slope in chapter §3.3.4. Figure 40 has shown that the behaviour follows a certain path, when the skin resistance is adapted with respect to the spacing. Table 13 shows the lateral skin resistance of the 30 datasets. The axial skin resistance is kept constant per meter, the base resistance is $F_{max} = 0\ kN$.

Table 13 Variation of the spacing

	Spacing $L_s[m]$					**Skin resistance per meter** $t\left[\frac{kN}{m}\right]$
	0.5	1	5	10	50	
Lateral skin resistance $T_{lat}[kN]$	2.5	5	25	50	250	**5**
	5	10	50	100	500	**10**
	25	50	250	500	2‘500	**50**
	50	100	500	1’000	5‘000	**100**
	250	500	2’500	5’000	25‘000	**500**
	500	1’000	5’000	25’000	50‘000	**1‘000**
Axial skin resistance $T_{skin}\ [kN]$	5	10	50	100	500	**10**

The result is plotted in Figure 72. Again the result follows a certain path. Only the results at a large spacing and a large lateral skin resistance show numerical instabilities and are considered not reliable (marked with red crosses in Figure 72). According to this figure a safety factor of around $\Sigma M_{sf} = 1.70$ can be obtained, when the lateral skin resistance is $T_{lat} = 5’000\ kN$ at a spacing of $L_s = 10\ m$. In fact the spacing is not taken realistically into account.

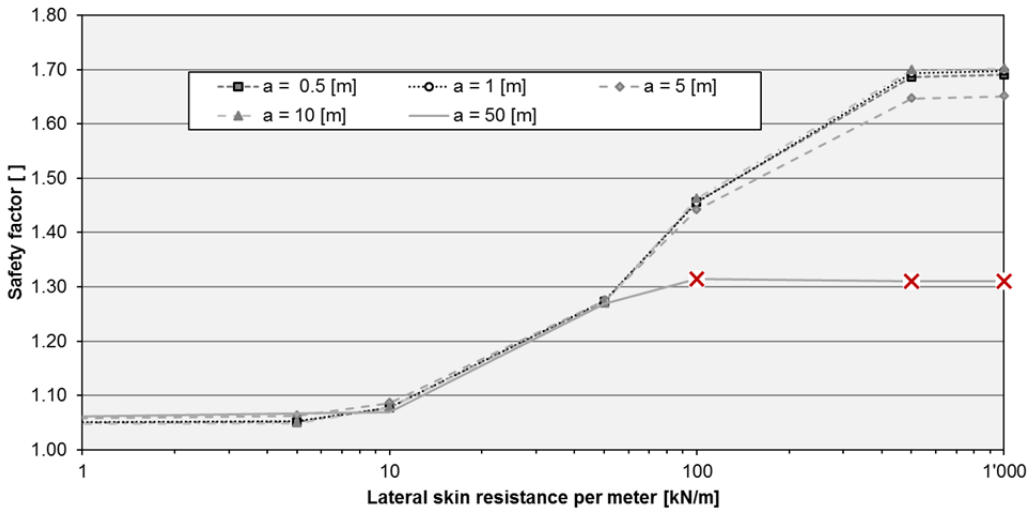

Figure 72 Safety factor vs. the lateral skin resistance per meter

The internal forces for a spacing of $L_s = 10\ m$ are plotted in Figure 73. They look like the result in Figure 71, but it should be noted that the internal forces are meant per meter. This means that the internal forces per Embedded Beam Row are 10 times bigger as displayed.

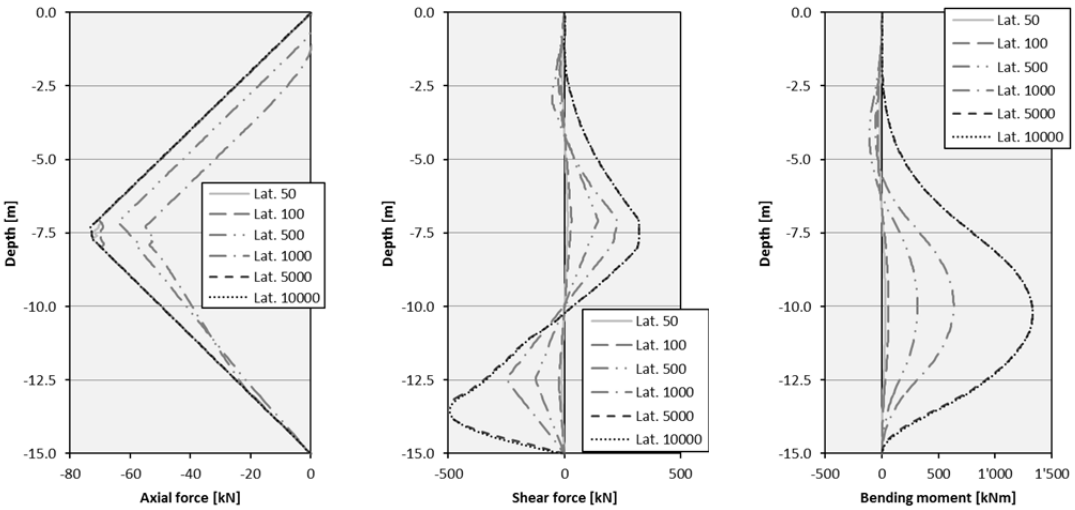

Figure 73 Internal forces for a spacing of $L_s = 10\ m$

4.3.5 Elastoplastic Embedded Beam Row

For the following calculations the strength reduction is applied to the structural elements as well. The evaluation is performed with a lateral skin resistance of $T_{lat} = 1'000 \frac{kN}{m}$, an axial skin resistance of $T_{skin} = 10 \frac{kN}{m}$ and a spacing of $L_s = 1\,m$. Since in most cases the axial forces have a minor influence, the axial plastic force is set larger than the maximal axial force ($N_{pl} = 200\,kN \gg N_{max} \cong 75\,kN$) to avoid plasticity in axial direction. The result of the variation is shown in Figure 74. Some additional calculations are performed. The lateral skin resistance is decreased to $T_{skin} = 100 \frac{kN}{m}$ (green line). At a plastic bending moment $M_{pl} < 1'000\,kNm$ the path is the same as obtained for $T_{skin} = 1'000 \frac{kN}{m}$. This means that the safety factor is limited by the plastic bending moment. Also calculations with a spacing of $L_s = 10\,m$ (blue line) are performed. The input values (including the plastic values) are adapted corresponding to the spacing as in the previous chapter. This means that the same result is obtained when the spacing, the skin resistance and the plastic moment have a constant ratio. Note that the plastic bending moment on the abscissa is the plastic bending moment per meter, which means that the input parameters for the blue line are 10 times larger as noted on the x-coordinate.

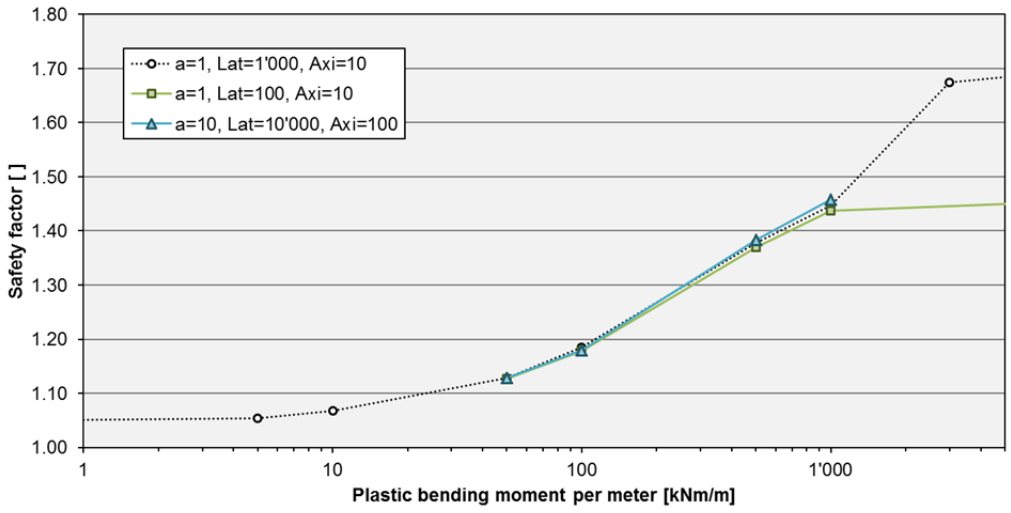

Figure 74 Variation of the plastic bending moment

4.4 Slope stability analysis in PLAXIS 3D

The slope stability in PLAXIS 3D for the non-homogeneous slope is only performed with Embedded Beams. The parameters are the same as described in Table 8. The model size is again twice the spacing. The axial skin resistance is $T_{skin} = 10 \frac{kN}{m}$. The spacing is varied and the displacement versus the safety factor is shown in Figure 75. The results are normalised against the safety factor of the unsupported slope ($\Sigma M_{sf} = 1.07$) and plotted in Figure 76.

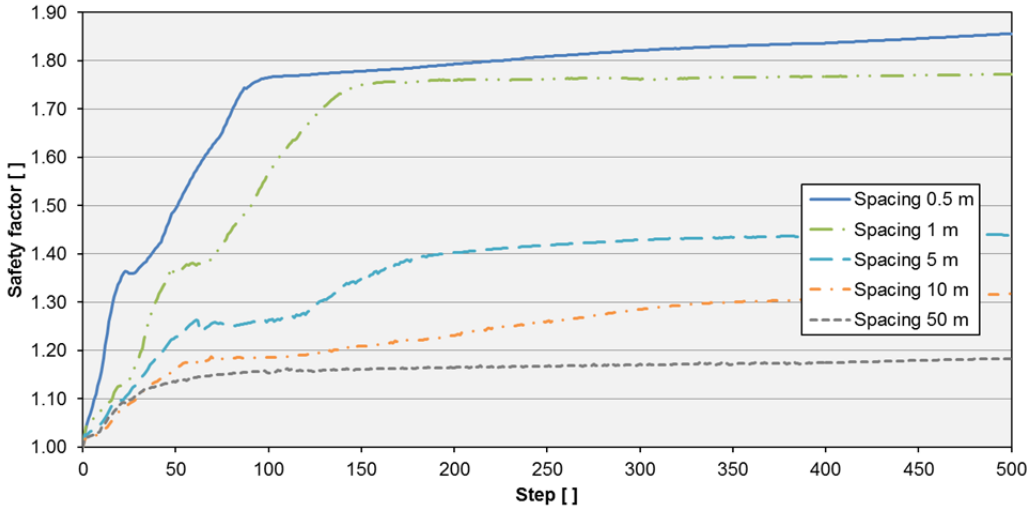

Figure 75 Safety factor vs. step (Embedded Beam) for non-homogeneous slope

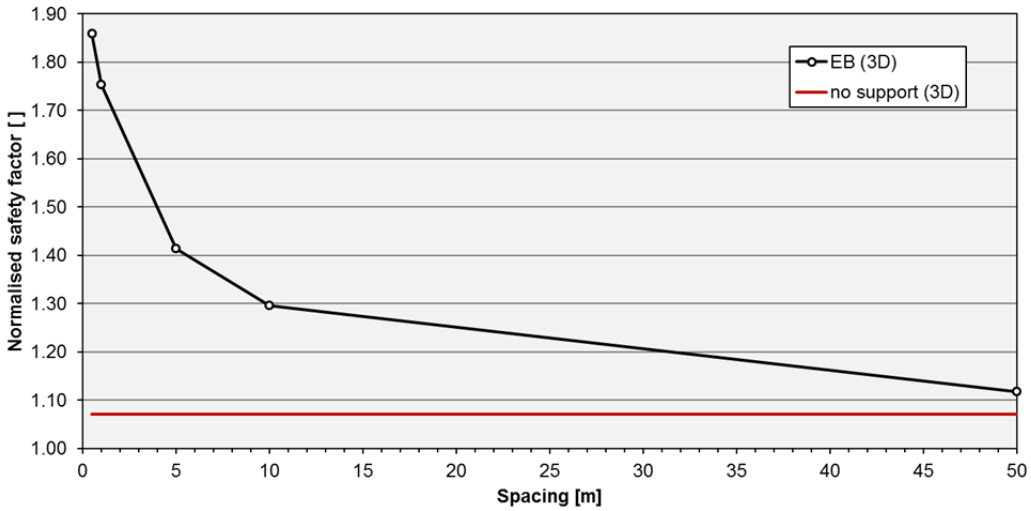

Figure 76 Normalised safety factor of Embedded Beam in non-homogeneous slope

4.5 Comparison of the results

The result for the Embedded Beam Row (2D) and the Embedded Beam (3D) are compared in Figure 77. The best fit is obtained by a lateral skin resistance of $T_{lat} = 500 \frac{kN}{m}$. Again the safety factor obtained by the 3-dimensional analysis cannot be matched without an arbitrary assumption for the lateral skin resistance.

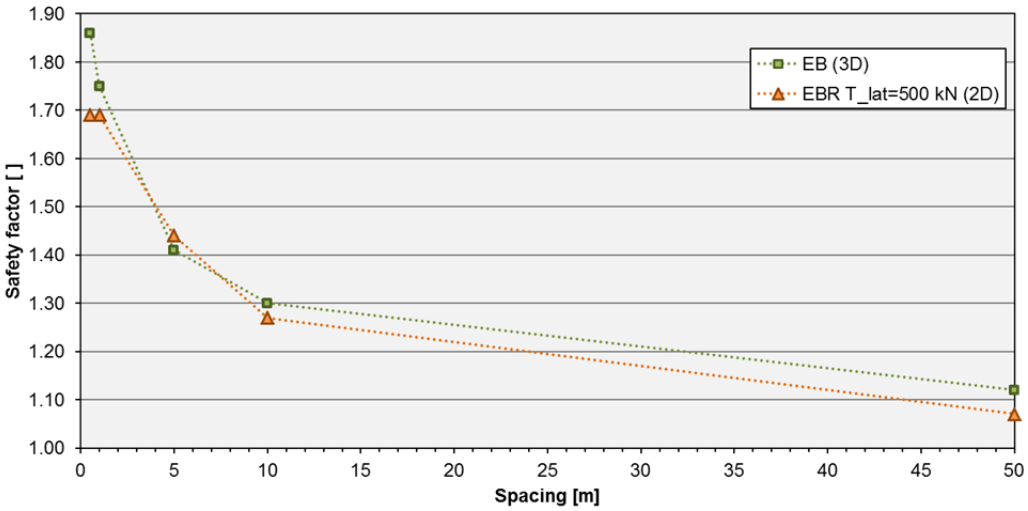

Figure 77 Comparison of safety factors by different methods

Figure 78 compares the failures obtained from 2D and 3D. At a small spacing the piles act like a wall and obtain the same failure at the piles as between the piles. At a spacing of $L_s = 5\ m$ the results from 2D and 3D do not correspond. At a large spacing the failure corresponds again.

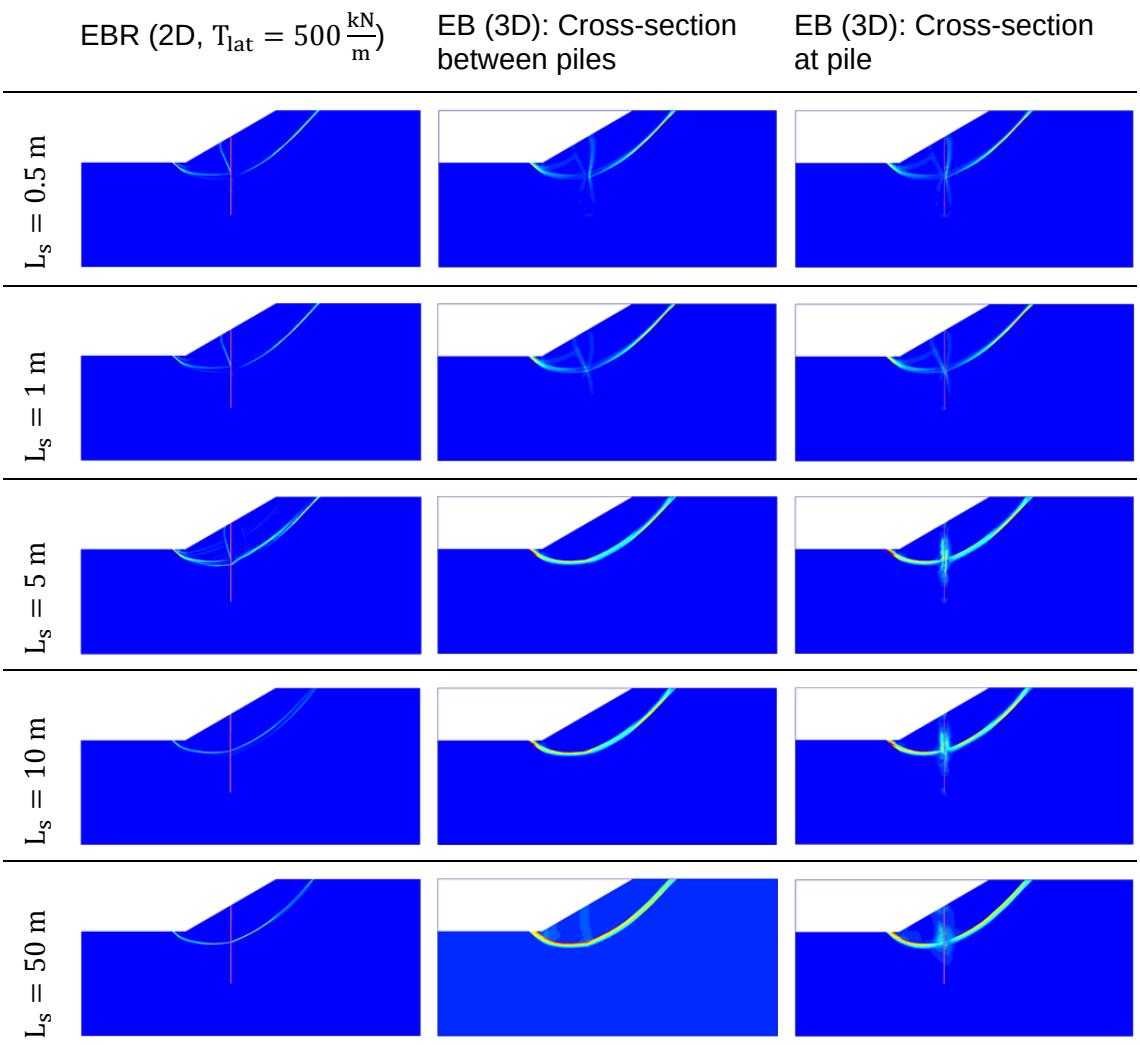

Figure 78 Comparison of the failure of EBR and EB (Incremental deviatoric strains)

4.6 Conclusion

The conclusions made in the investigation on the homogeneous slope are approved. The base and axial skin resistance have almost no influence on the result. The variation of the spacing, the lateral skin resistance and the elastoplastic parameters follow a certain pattern. When no elastoplastic behaviour is considered for the Embedded Beam Row, the lateral skin resistance and the spacing are decisive; when elastoplastic behaviour is determined the safety factor is limited by the plastic moment. As long as those parameters are in a certain ratio, the same result is obtained. The calculations in PLAXIS 2D can be fitted to the results from 3-dimensions. The result is still not identical but follows a similar path.

5 Case study

Grabe (2016) has investigated the slope stability of a slope supported by dowels in a three dimensional analysis. This case study is used in the following, but with some modifications. The soil parameters used in the study are given in Table 14. The dowel parameters are summarised in Table 15. The model size, the dowel positions and the mesh refinement are displayed in Figure 79. The initial stresses are calculated by 'Gravity loading' and the water load is applied as shown in Figure 79. In the next step the dowel is installed in a 'Plastic phase' and subsequently the 'Safety analysis' is performed. The water table ground is assumed to be at a horizontal distance of $52.5\ \mathrm{m}$ from the slope toe. All analyses are performed as drained analyses.

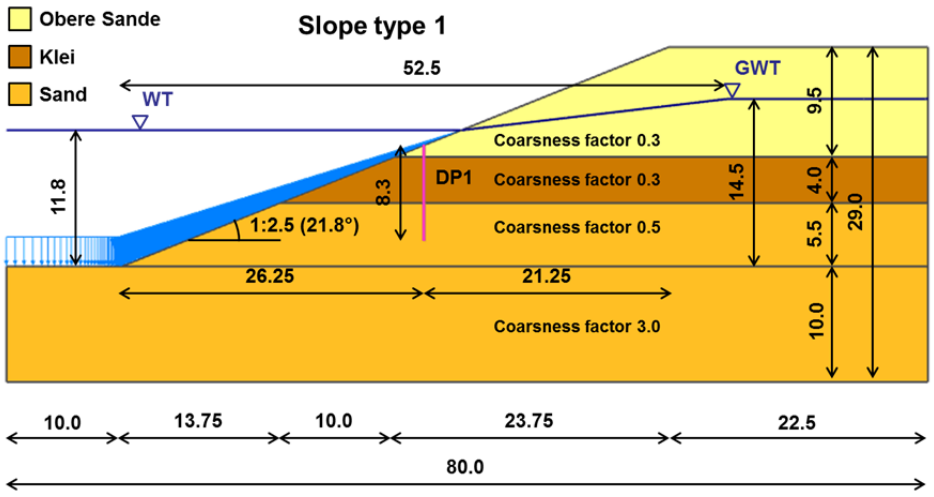

Figure 79 Soil profile for the case study

Table 14 Soil properties of the case study

Parameter	Name	Obere Sande	Klei	Sand	Unit
Material model	-	Mohr-Coulomb			-
Unsaturated specific weight	γ_{unsat}	18	16	21	$\left[\frac{kN}{m^3}\right]$
Saturated specific weight	γ_{sat}	20	16	21	$\left[\frac{kN}{m^3}\right]$
Young's modulus	E'	20'000	7'000	40'000	$\left[\frac{kN}{m^2}\right]$
Poisson's ratio	ν'	0.33	0.4	0.32	[ ]
Cohesion	c'_{ref}	0	9	0	$\left[\frac{kN}{m^2}\right]$
Friction angle	φ'	34.7	20.7	37.4	[°]
Dilatancy angle	ψ	0	0	2.5	[°]

Table 15 Embedded Beam Row parameters of the case study

Parameter	**Name**	**Dowel DP1**	**Unit**
Behaviour option	-	Pile	-
Connection point	-	Top	-
Connection	-	Free	-
Material type	-	Elastic	-
Young's Modulus	E	2.1E8	$\left[\frac{\mathrm{kN}}{\mathrm{m}^2}\right]$
Specific weight	γ	60.0	$\left[\frac{\mathrm{kN}}{\mathrm{m}^3}\right]$
Pile type	-	User-defined	-
Profile area	A	0.0107	$[\mathrm{m}^2]$
Moment of inertia	I	2.32E-4	$[\mathrm{m}^4]$
Spacing	$\mathrm{L}_{\mathrm{spacing}}$	2.0	$[\mathrm{m}]$
*specific weight is the difference between weight of the Embedded Beam Row and the soil			

5.1 Unsupported slope

5.1.1 Mesh size

The result of the mesh variation is shown in Figure 80. For further analyses the mesh size of 0.02 with a minimal element size of $0.01\ \mathrm{m}^2$ is used. The safety factor for the unsupported slope is $\Sigma \mathrm{M}_{\mathrm{sf}} = 1.18$.

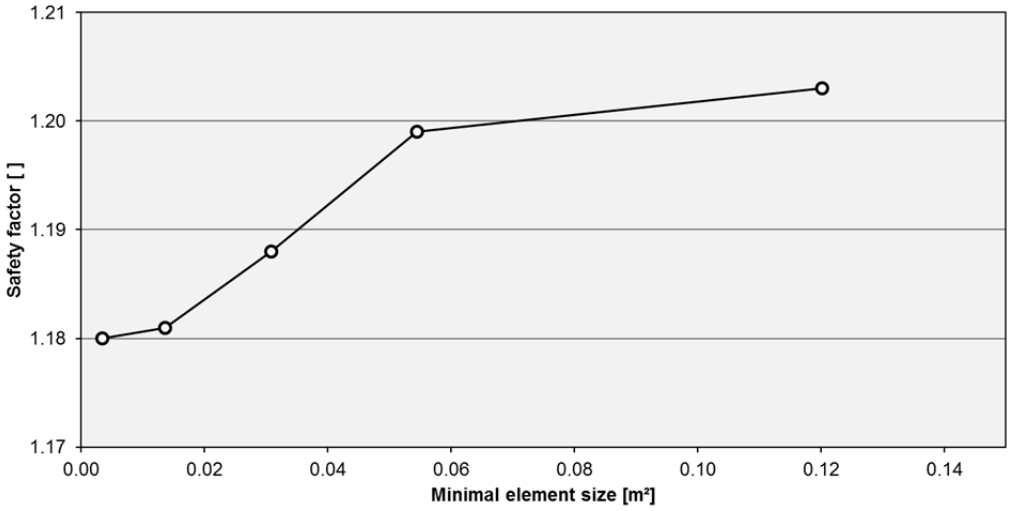

Figure 80 Mesh size variation for the case study

The failure mechanism obtained in Figure 81 is almost identical to the result obtained by Grabe (2016).

Result mesh size 0.02 | Result with PLAXIS 2D by Grabe (2016)

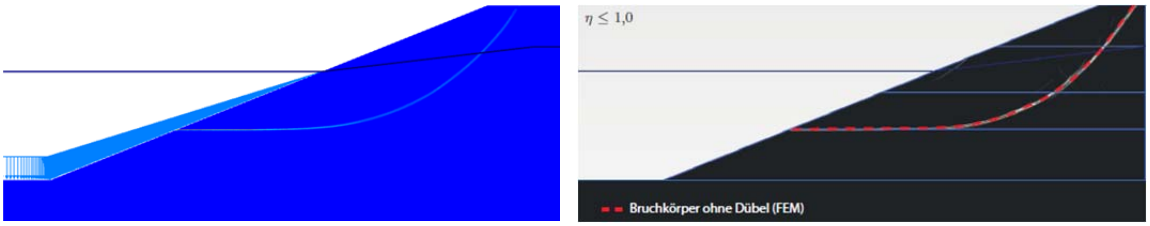

Figure 81 Comparison of the failure for the unsupported slope obtained by Grabe (2016)

5.2 Supported slope

The evaluation of the slope stability supported by an Embedded Beam Row is performed by:

- Embedded Beam Row with constant lateral skin resistance, Figure 82a
- Embedded Beam Row with lateral skin resistance increasing with depth, Figure 82b

a) 'Constant' lateral skin resistance | b) 'Increasing' lateral skin resistance

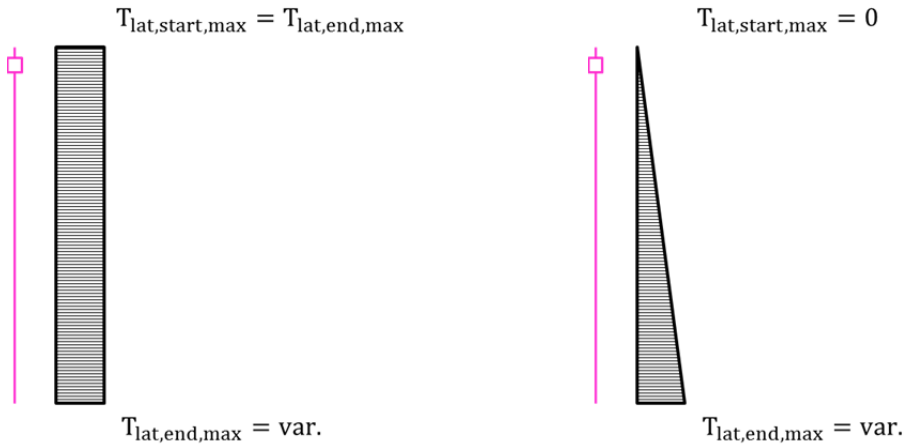

Figure 82 'Constant' and 'increasing' lateral skin resistance

Since the base and the axial skin resistance have been shown to have no influence, the axial skin resistance is $T_{skin} = 10 \frac{kN}{m}$ and the base resistance is $F_{max} = 0\,kN$. The safety factor obtained by the variation of the constant and the increasing lateral skin resistance is shown in Figure 83. The safety factor obtained from the increasing lateral skin resistance is smaller than the one from the constant lateral skin resistance. The safety factor for an Embedded Beam Row with unlimited lateral skin resistance is $\Sigma M_{sf} = 1.33$.

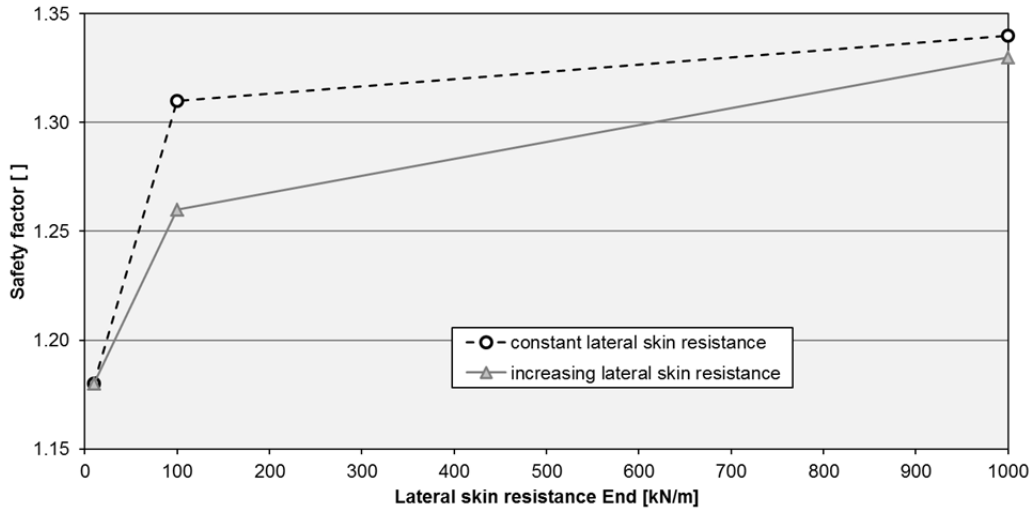

Figure 83 Variation of the lateral skin resistance for the case study (constant and increasing lateral skin resistance)

The safety factor obtained by Grabe (2016) is $\Sigma M_{sf} = 1.32$. The result from Grabe (2016) in 3D is compared to the result obtained by a lateral skin resistance of $T_{lat,end} = 1'000 \frac{kN}{m}$ in Figure 84. The failure of the constant skin resistance substantially fits, although the failure obtained with the analysis in PLAXIS 2D is rather interpreted as a failure close to the head of the pile.

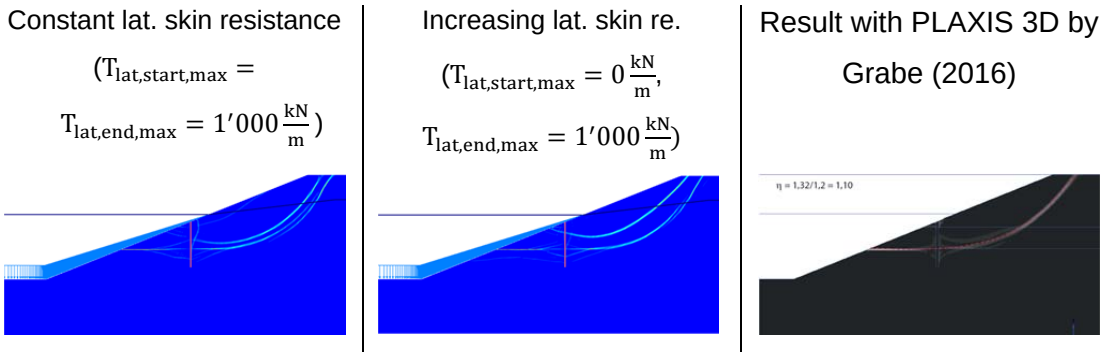

Figure 84 Comparison of the failure for the supported slope obtained by Grabe (2016)

The internal forces obtained in the last step of the safety analysis are shown in Figure 85 and are almost identical.

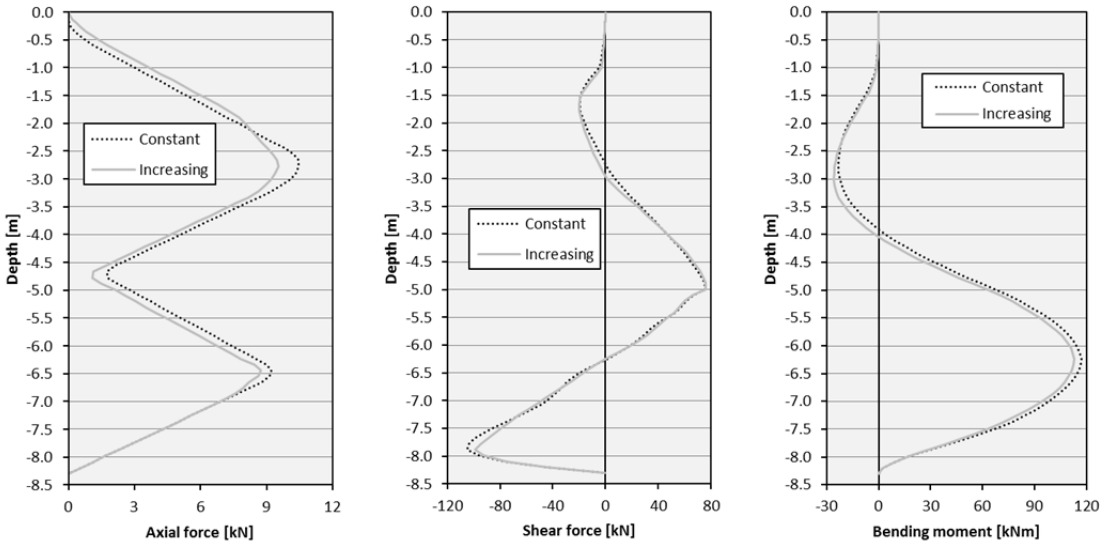

Figure 85 Internal forces obtained in the last step

6 Conclusion

In several examples it is shown that the Strength Reduction Method conforms to results obtained from Limit Equilibrium for the unsupported slope. Also the failure mechanisms are relatively conforming. The calculation time in SRFEA is still larger and a fine mesh is mandatory. On the other hand the SRFEA obtains the failure automatically with no further assumptions. For the application of SRFEA a certain experience is needed.

In the description of the Embedded Beam Row in chapter §2.3 it is already pointed out that the Embedded Beam Row is not fully capable to model lateral loading. The derivation of the default interface stiffness factors is not based on physical principals but on a numerical study by Sluis (2012). The numerical studies have shown numerous limitations of the usage of an Embedded Beam Row.

In general the result obtained from a stiff Embedded Beam Row conforms to the result obtained with a plate. Also a slope supported by a weak Embedded Beam Row conforms to the unsupported slope.

The safety factor obtained by an Embedded Beam Row follows a certain pattern shown in several examples. This means when the skin resistances, the plastic moment and the spacing are correlated, the same result is obtained. Piles at a small spacing almost act like a plate. However, the behaviour for a large spacing is not modelled realistically. Sluis (2012) and Kwaak (2015) mention the limitation by the application area of the Embedded Beam Row. In fact the Embedded Beam Row could not be used for dowelling since the spacing-diameter ratio described by Witt (2013) is larger than the application area.

The internal forces are mostly influenced by the skin resistance since they limit the maximal axial and lateral force per meter. However it has to be questioned if the internal forces obtained are realistic in these cases.

In PLAXIS 2D the lateral skin resistance is an additional input parameter for the Embedded Beam Row. This parameter is the governing parameter for lateral loaded piles. Sluis (2012) shows different approaches to derive the values. Kwaak (2015) obtains good results by using the API methods, but he states the derivation of the parameters as time-consuming. Kwaak (2015) also recommends improving the Embedded Beam Row by making the lateral interface stiffness factor on stress- or strain-dependent.

PLAXIS 3D unfortunately does not provide elastoplastic behaviour for the Embedded Beam. Elastoplastic behaviour of a dowel can be modelled when using volume elements with interfaces, and assigning the Mohr-Coloumb criterion. The three dimensional investigations with Embedded Beams and volume elements have shown that the usage of volume elements in safety analysis is numerically more stable and the safety factor is obtained by a smaller number of calculation steps. On the other hand the usage of Embedded Beams allows a simple and fast modelling of piles.

7 Literature

Algulin, J.; Pedersen, B. (2014)
Modelling of a piled raft foundation as a plane strain model in PLAXIS 2D. Master thesis. Chalmers University of Technology Göteborg, Sweden.

Brandl, H. (2009)
Stützbauwerk und konstruktive Hangsicherung. In: Grundbau-Taschenbuch, Teil 3, 7. Auflage: Gründung und geotechnische Bauwerke, Witt (Hrsg.). Berlin, Deutschland. pp 746-901

Brinkgreve, R.B.J.; Bakker, H.L. (1991)
Non-linear finite element analysis of safety factor. In: Proceedings of the 7th International Conference of Computer Methods and Advances in Geomechanics. Beer & Booker & Carter (eds.). Rotterdam, the Netherlands.

Brinkgreve, R.B.J.; Kumarswamy, S.; Swolfs, W.M. (2016a)
PLAXIS 2D Reference Manual 2016. Build 8122. Plaxis bv. Delft, The Netherlands.

Brinkgreve, R.B.J.; Kumarswamy, S.; Swolfs, W.M. (2016b)
PLAXIS 2D Material Model Manual 2016. Build 8122. Plaxis bv. Delft, The Netherlands.

Grabe, J.; (2016)
Numerische Untersuchungen zur Standsicherheit von verdübelten und unverdübelten Böschungen. Abschlussbericht. Technische Universität Hamburg-Harburg, Deutschland.

Griffiths, D.V.; Lane O.A. (1999)
Slope stability analysis by finite elements. In: Géotechnique 49, No. 3. pp 387-403

Huder, J. (1983)
Stabilisierung von Rutschungen mittels Ankern und Pfählen. In: Schweizer Ingenieur und Architekt, Band 101, Heft 16. ETH Zürich, Schweiz. pp 422-425

Kwaak van der, B. (2015)
Modelling of dynamic pile behaviour during an earthquake using PLAXIS 2D: Embedded Beam (rows). Master thesis. Delft University of Technology, The Netherlands.

Mosser, C. (2016)
Numerical Study on the Behaviour of Soil Nails. Master thesis. Technical University Graz, Austria.

Rüegger, R. (2013)
Vorlesungsteil Verankerung. In: Entwurf & Konstruktion in der Geotechnik, Bauingenieurwissenschaften, Master 1. Semester. Institut für Geotechnik. ETH Zürich, Schweiz. pp 123-163

Sloan, S.W. (2013)
Geotechnical stability analysis. In: Géotechnique 63, No. 7. pp 531-572

Sluis, J. (2012)
Validation of Embedded Pile Row. Master thesis. Delft University of Technology, The Netherlands.

Sluis, J.; Besseling, F.; Stuurwold, P. and Lengkeek, A. (2013)
Validation and Application of the Embedded Pile Row-feature in PLAXIS 2D. Plaxis Bulletin, Issue 34, Brinkgreve & Beernink & Lengkeek (eds.). Delft, The Netherlands. pp 10-13

Tschuchnigg, F.; Schweiger, H.F.; Sloan, S.W. (2015)
Slope stability analysis by means of finite element limit analysis and finite element strength reduction techniques. Part I: Numerical studies considering non-associated plasticity. In: Computers and Geotechnics 70. pp 169-177

Witt, K.J. (2013)
Hangverdübelung mit Bohrpfählen zur Erhöhung der Standsicherheit. Informationstag Ingenieurbau 2013 - Praktisches aus dem Konstruktiven Ingenieurbau Bauhaus-Universität Weimar, 9. Oktober 2013. Bauhaus Akademie Schloss Ettersburg, Deutschland.

Wolffersdorff von, P.-A.; Schweiger, H.F. (2008)
Numerische Verfahren in der Geotechnik. In: Grundbau-Taschenbuch, Teil 1, 7. Auflage: Geotechnische Grundlagen, Witt (Hrsg.). Berlin, Deutschland. pp 501-557

Appendix A: Calculation time of the unsupported homogeneous slope

Figure 86 adds the calculation time to Figure 10 with the safety factor per minimal element size (values in Table 16). The values show that the calculation time is approximately proportional to the number of steps, meaning the calculation time for 500 steps is 5 times the calculation time for 100 steps. The calculation time rises rapidly at a mesh factor of 0.02. This mesh factor gives more than a sufficient fine mesh and the calculation time is still moderate.

Table 16 Calculation time for different meshes

Mesh	**Mesh factor [ ]**	**Element no. [ ]**	**Calculation time [min] for**		
			100 steps	**200 steps**	**500 steps**
	0.01	33’581	23	47	108
	0.02	8’481	4	8	15
v. fine	0.03	3’834	2	3	13
fine	0.04	2’138	1	2	6
	0.05	1’407	1	1	4
medium	0.06	995	1	1	3
	0.07	728	1	1	2

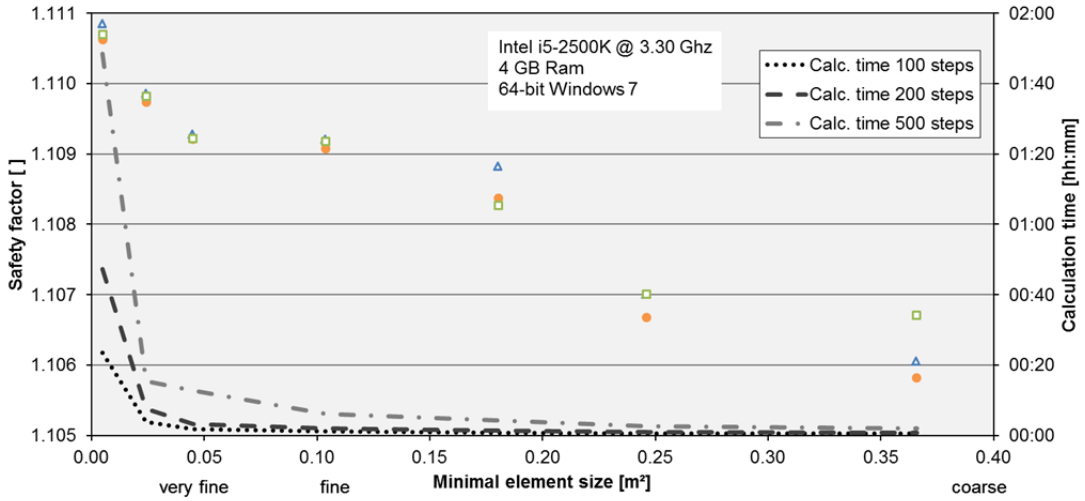

Figure 86 Safety factor vs. minimal element size and calculation time

The incremental deviatoric strains, the total displacements and the plastic points show that the location of the failure is identical (Figure 87). The amount of plastic points changes though. The plastic area is minor to the superfine meshed model (mesh factor 0.01). A rough mesh leads to more plastic points. The amount of steps has no influence on the plastic points (Figure 88).

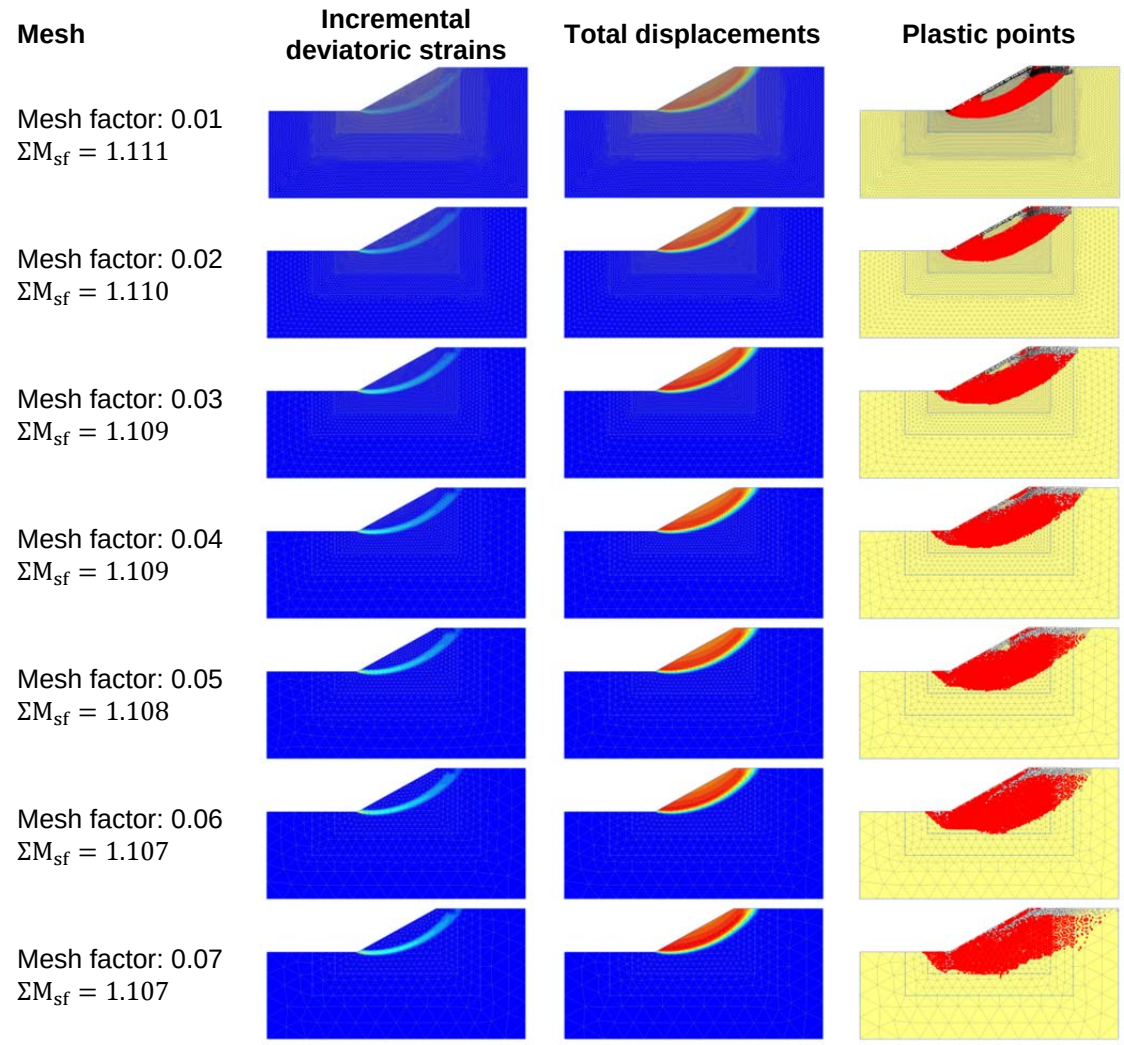

Figure 87 Failure of different meshes (500 steps)

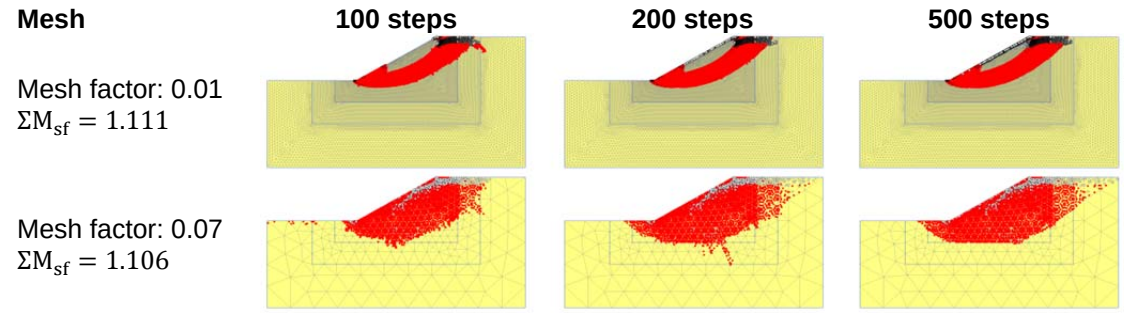

Figure 88 Incremental deviatoric strains at 100, 200 and 500 steps

Appendix B: Calculation time and mesh quality of the supported homogeneous slope

An analysis of the mesh quality and calculation time of the supported slope is performed. The lateral and axial skin resistances are $T_{skin} = T_{lat} = 10 \frac{kN}{m}$ at a spacing of $L_s = 1\ m$. As in chapter §3.1.1 the mesh size is varied between 0.01 and 0.08 to verify the mesh chosen at the beginning of the calculations. The amount of steps is 1'000. The result is shown in Table 17 and Figure 89. This chart verifies that the chosen mesh is fine enough.

Table 17 Result of the mesh variation of the supported slope

Mesh	**Mesh factor**	**No. of soil elements**	**Minimal elem. area**	**Average elem. size**	**Safety factor**
	[ ]	[ ]	$[m^2]$	$[m]$	$\sum M_{SF}$[ ]
	0.01	35674	0.00	0.2189	1.151
	0.02	8982	0.02	0.4363	1.150
v. fine	0.03	4073	0.05	0.6479	1.150
fine	0.04	2276	0.08	0.8668	1.150
	0.05	1498	0.12	1.068	1.149
medium	0.06	1087	0.19	1.254	1.148
	0.07	756	0.31	1.504	1.148
coarse	0.08	599	0.36	1.69	1.149

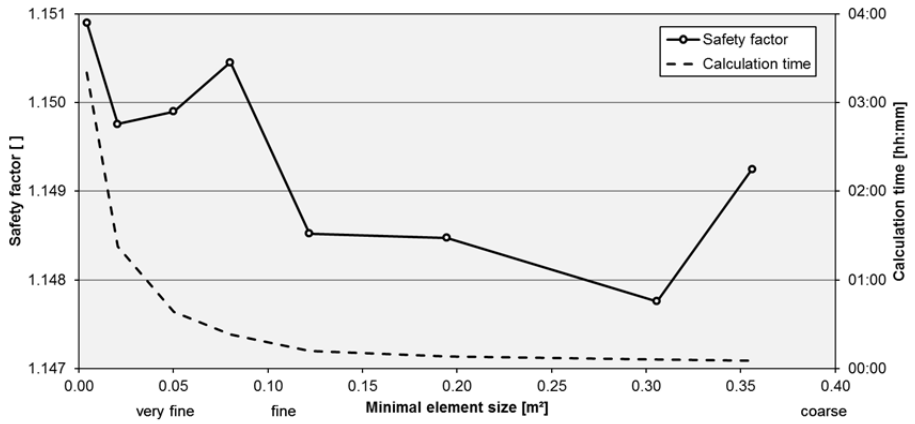

Figure 89 Safety factor vs. minimal element size and calculation time for supported slope

Appendix C: Verification of maximal safety factor

The minimal safety factor obtained from the analysis should match the unsupported slope: $\Sigma M_{sf,min} = 1.11$ (chapter §3.1.1). A failure beneath the support is possible if the support is stiff enough to stabilise the whole slope. An analysis with a $7.5\ m$ long dowel in SLIDE is performed to obtain a realistic failure line. The shear strength of the support is set to infinite (in SLIDE 'micro pile', out-of-plane spacing $0.5\ m$, and the pile shear strength $1.0E7\ kN$). The calculation method used is GLE/Morgenstern. The safety factor obtained is $FoS = 1.21$ (Spencer $FoS = 1.22$). The list of the coordinates of the failure line is summarised in Table 18. Based on this coordinates a PLAXIS model is created. The material above this failure line is assigned with an increased shear strength ($\Delta\varphi = 5°$) to push the failure beneath the failure line (Figure 90). The safety factor is $\Sigma M_{sf} = 1.233$. It also corresponds well with the factor obtained by the analysis with a plate and an elastic area on the top of the pile (chapter §3.1, Figure 15: $\Sigma M_{sf} = 1.227$).

Table 18 Coordinates of failure line (coordinates of the slope foot: $X = 0\ m$, $Y = 0\ m$)

No.	X [m]	Y [m]	No.	X [m]	Y [m]	No.	X [m]	Y [m]
1	-1.84	0.00	**12**	8.66	-2.50	**23**	18.48	3.47
2	-1.18	-0.59	**13**	9.77	-2.03	**24**	19.08	4.01
3	-0.80	-0.92	**14**	10.87	-1.57	**25**	19.67	4.54
4	0.46	-1.79	**15**	11.88	-1.07	**26**	20.51	5.33
5	1.39	-2.21	**16**	12.89	-0.57	**27**	21.11	5.94
6	2.55	-2.54	**17**	13.77	-0.05	**28**	21.70	6.54
7	3.93	-2.73	**18**	14.65	0.46	**29**	22.75	7.65
8	4.76	-2.75	**19**	15.42	0.99	**30**	23.64	8.62
9	5.60	-2.77	**20**	16.18	1.51	**31**	24.17	9.16
10	6.61	-2.70	**21**	17.30	2.40	**32**	25.03	10.00
11	7.63	-2.63	**22**	17.89	2.94			

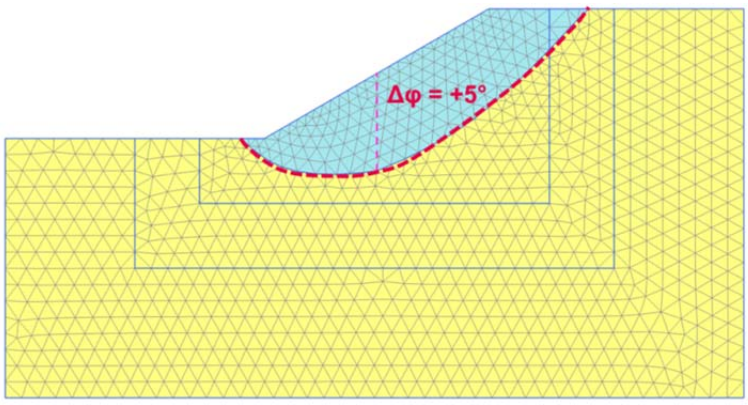

Figure 90 Soil profile with incremental friction angle above the failure line

Appendix D: Influence of the axial skin resistance for the Embedded Beam (3D)

A three-dimensional model with a depth of $1\,\mathrm{m}$ and a spacing of $0.5\,\mathrm{m}$ between the Embedded Beams is generated to investigate the influence of the axial skin resistance. Figure 91 shows that the axial skin resistance, as already observed in §3.3.1, has an insignificant influence on the result. Also the failure mechanism is almost identical.

The previous mesh is modified; the validation of the accuracy is performed by a calculation with deactivated Embedded Beams. The safety factor obtained for the unsupported slope is $\Sigma M_{sf} = 1.115$ after 200 steps. The accuracy is sufficient.

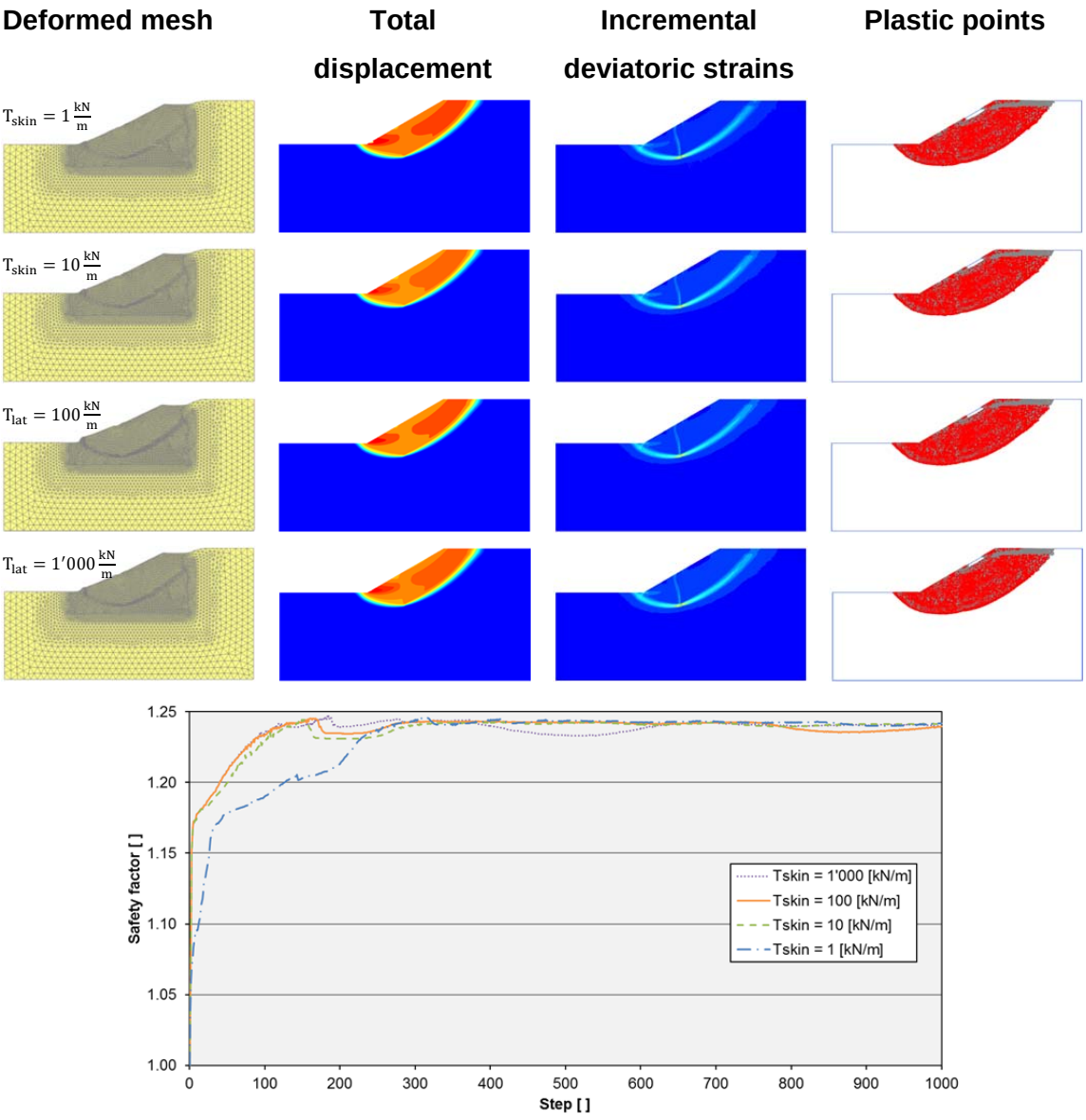

Figure 91 Failure of the Embedded Beam with varying axial skin resistance